UNIVERSITY OF BIRMINGHAM

DEVELOPMENT OF BIOMIMETIC WATER-REPELLENT SURFACES BASED ON ZINC OXIDE NANOPILLARS FOR ANTIBIOFOULING APPLICATIONS

by

JITAO ZHANG

A thesis submitted to the University of Birmingham for the degree of

DOCTOR OF PHILOSOPHY

Department of Mechanical Engineering

School of Engineering

College of Engineering and Physical Sciences

University of Birmingham

August 2024

UNIVERSITY OF
BIRMINGHAM

University of Birmingham Research Archive

e-theses repository

This unpublished thesis/dissertation is copyright of the author and/or third parties. The intellectual property rights of the author or third parties in respect of this work are as defined by The Copyright Designs and Patents Act 1988 or as modified by any successor legislation.

Any use made of information contained in this thesis/dissertation must be in accordance with that legislation and must be properly acknowledged. Further distribution or reproduction in any format is prohibited without the permission of the copyright holder.

ABSTRACT

Biofouling, particularly bacterial adhesion and subsequent biofilm formation, significantly impacts medical device efficacy and patient health, presenting serious healthcare challenges and increased medical costs. Conventional approaches, such as antibiotics and chemical coatings, often face limitations due to resistance development, toxicity, and durability concerns. This thesis investigates a novel approach combining biomimetic zinc oxide (ZnO) nanopillar structures with advanced water-repellent surface modifications to simultaneously achieve robust antibacterial and water-repellent properties. Optimized ZnO nanopillar arrays were successfully fabricated through hydrothermal synthesis method, demonstrating exceptional bactericidal effects mediated by photocatalytic generated reactive oxygen species (ROS). Subsequent modifications included the development of biomimetic superhydrophobic (SHS) and lubricant-infused surfaces (LIS), effectively reducing bacterial adhesion by significantly decreasing droplet-surface interactions.

The superhydrophobic ZnO nanopillar surfaces display exceptional water repellency. The contact-angle hysteresis is confined to just 2–3°, and water droplets roll off at a tilt angle of only 1°. Additionally, droplets impacting the surfaces with different Weber numbers indicating that a robust Cassie–Baxter wetting state was maintained. These surfaces effectively inhibited model pathogenic bacteria gram-positive *Staphylococcus aureus* (*S. aureus*) and gram-negative *Escherichia coli* (*E. coli*) without the need for UV or antimicrobial agents.

Additionally, a biomimetic lubricant-infused surface based on nanopillar structures of zinc oxide (LIS-ZnO) is reported. Inherent antibacterial activity and an effective reduction in bacterial attachment against *E. coli* and *Pseudomonas syringae pv. syringae* (*Pss*), which exhibit different biofilm formation modes, are exhibited by this type of surface. LIVE/DEAD assays, employed with confocal microscopy, indicated that bacteria were killed after 24 hours of incubation on the surface. This outcome was attributed to the photocatalytic activity possessed by the underlying ZnO nanopillars, as demonstrated by the effective degradation of cyanine-based fluorescent dyes within a 5-hour observation period. Furthermore, the adherent bacterial signals observed on the LIS-ZnO surfaces were the lowest among all tested samples. Specifically, colony formation units of *E. coli* and *Pss* were reduced by approximately 70% and 35%, respectively, compared to a superhydrophobic surface based on the same nanopillars. These attributes render the LIS-ZnO surfaces a potential candidate for use in healthcare industries to resist bacterial adhesion and address biofouling.

Overall, this work presents a scalable strategy based on biomimetic water-repellent ZnO nanopillar surfaces, offering a robust and long-lasting antibiofouling solution for medical interfaces. The combined bactericidal and anti-adhesion effects have the potential to significantly reduce device-associated infections, contributing to improved patient outcomes and reduced healthcare costs.

Dedicated to my parents:

Mr Xinquan Zhang & Ms Jingbo Ping

Thank you for your continuous love and support.

I am truly grateful and honoured to have you as my parents.

I love you.

ACKNOWLEDGEMENTS

First and foremost, I would like to convey my heartfelt gratitude to my supervisor, Dr. Nan Gao. Your guidance, patience, care, and continuous support have been invaluable. Not only did you consistently assist me when I encountered academic obstacles, such as experimental or writing difficulties, but you also kindly listened to my personal concerns in daily life. Without your assistance, my PhD studies would not have been possible. Most significantly, I admire your high standards for research quality, attention to detail, and critical thinking. These characteristics inspire me to continue pursuing the academic path. It has been an honour to be your student.

I would also like to extend my gratitude to my co-supervisors, Dr. Jason Stafford and Dr. Carl Anthony, for their support throughout my PhD journey. Thanks to Professor Duc Pham for the support, guidance and encouragement with my annual review during my PhD. Special thanks to Dr. James Churm for his guidance and assistance in the processing room and for sharing his own PhD experiences with me. I am also grateful to Dr. Ludwig Schneider, Dr. Felicity de Cogan, Miss. Georgia Williams, Dr. Mojgan Rabiey, Dr. Diana Vinchira-Villarraga for their support and help during my PhD research. My heartfelt thanks go to my groupmates, Dr. Alexander Saal, Dr. Navdeep Sangeet Singh, Dr. Thanaphun Jitniyom, and Miss. Yue Li, for their support in my research and for the casual conversations that significantly alleviated my anxiety.

I would also like to thank to all my friends that I met for those joyful days. Thanks to all colleagues and friends in office 106 and 207. Special thanks to Miss. Xiangyu Wei, Dr. Zeyu Sun, Mr. Xu He, Mr. Fengzhe Wang, Dr. Meixi Liu, Mr. Fanggang Zhang, Mr. Fei Yu, Mr. Yiqi Zhou, Mr. Tianshu Ruan and Mr. Haoyu Shi.

Finally, I reserve this important paragraph as ending to express my sincerest gratitude to my family for their complete trust, support, encouragement, and love. This milestone would not have been possible without their invaluable support.

TABLE OF CONTENT

LIST OF ACRONYMS

ZnO: Zinc Oxide

ROS: Reactive Oxygen Species

SHS: Superhydrophobic Surface

LIS: Lubricant-Infused Surface

SHS-ZnO: Superhydrophobic Zinc Oxide Nanopillar Surfaces

LIS-ZnO: Lubricant-Infused Zinc Oxide Nanopillar Surfaces

SEM: Scanning Electron Microscopy

CLSM: Confocal Laser Scanning Microscopy

RMS: Root Mean Square of surface roughness

CA: Contact Angle

RA: Rolling Angle

AFM: Atomic Force Microscopy

SR: Silicone Rubber

PDMS: Polydimethylsiloxane

FESEM: Field Emission Scanning Electron Microscopy

XRD: X-ray Diffraction

FTIR: Fourier Transform Infrared Spectroscopy

TEM: Transmission Electron Microscopy

ITO: Indium Tin Oxide

CFU: Colony Forming Units

EPS: Extracellular Polymeric Substances

NO: Nitric Oxide

CVD: Chemical Vapor Deposition

NPs: Nanoparticles

FAS: Fluoroalkylsilane

UV: Ultraviolet

ANOVA: Analysis of Variance

DMEM: Dulbecco's Modified Eagle Medium

NaOH: Sodium Hydroxide

$Zn(NO_3)_2 \cdot 6H_2O$: Zinc Nitrate Hexahydrate

DI water: Deionized water

PBS: Phosphate-buffered Saline

DRS: Diffuse Reflectance Spectroscopy

LIST OF SYMBOLS

$\boldsymbol{\theta_c}$**:** Contact angle (°)

$\boldsymbol{\gamma}$**:** Surface tension (N/m)

$\boldsymbol{\gamma_{sv}}$**:** Solid-vapor surface tension (N/m)

$\boldsymbol{\gamma_{sl}}$**:** Solid-liquid interfacial tension (N/m)

$\boldsymbol{\gamma_{vl}}$**:** Liquid-vapor surface tension (N/m)

$\boldsymbol{\theta_a}$**:** Advancing contact angle

$\boldsymbol{\theta_r}$**:** Receding contact angle

$\boldsymbol{\theta_w}$**:** Wenzel contact angle (°)

$\boldsymbol{r}$**:** Surface roughness factor (dimensionless)

$\boldsymbol{\theta_{CB}}$**:** Cassie–Baxter contact angle (°)

$\boldsymbol{\varphi_S}$**:** Dimensionless fraction of the solid surface area in contact with liquid

$\boldsymbol{F_{LA}}$**:** Lateral adhesion force (N)

$\boldsymbol{W_a}$**:** Adhesion work

$\boldsymbol{W_c}$**:** Cohesion work

$\boldsymbol{W_s}$**:** Spreading work

We: Weber number

$\mathbf{E_g}$**:** Optical Bandgap Energy

LIST OF TABLES

LIST OF FIGURES

CHAPTER 1 INTRODUCTION

1.1 Background and motivation

The term of biofouling in healthcare industry generally refers to biofilms formed by bacteria [1], which pose a significant threat to human health. The formation of biofilms on the surfaces of medical devices and implants, such as scalpels and catheters, is a leading cause of nosocomial (hospital-acquired infections), or iatrogenic infections (medically induced infections, including those caused by procedures or treatments) [2-6]. Meanwhile, the need for repeated treatments and equipment replacement due to biofouling significantly increases healthcare costs [7]. As a result, effective methods for the prevention and control of biofilms are in high demand. Traditional antibiotic therapies, while initially effective, become less so over time as bacteria within biofilms develop resistance, leading to a significant reduction in treatment efficacy [8]. Therefore, there is an urgent need to find alternative methods to address this challenge. In recent years, researchers have begun to focus on the potential of antimicrobial agents and various metal oxides in preventing bacterial infections [9]. Metal oxide has garnered significant attention due to their broad-spectrum antimicrobial activity and sustained long-term antimicrobial effects [10]. For example, metal oxide photocatalysts such as Titanium Dioxide (TiO_2) and Zinc Oxide (ZnO) have demonstrated antibacterial performance due to the generation of reactive radicals under light irradiation [11-15]. Specifically, this photocatalytic activity can cause cell membrane disruption and induce oxidative stress in bacterial cells. ZnO is particularly interesting because it can exhibit

photocatalytic activity under ambient conditions without dedicated ultraviolet (UV) illumination, offering a potential solution for biofouling prevention [12-14]. However, while ZnO possesses effective bactericidal properties, ZnO is typically hydrophilic (water-attracting, with a tendency to interact or bond with water molecules), which does not prevent the initial attachment and colonization of bacterial cells.

Typically, the spread and adhesion of bacteria, which make up biofilms, are often more severe in the presence of liquids, such as in the form of bulk flow and intermittent droplets [16-19]. Against this background, water-repellent surfaces with self-cleaning properties have gained significant attention [20]. The two main types of water repellent surfaces that have been explored over the past decade are superhydrophobic surfaces inspired by lotus leaves, and lubricant-infused surfaces inspired by pitcher plants. The first type of water repellent surfaces consists of superhydrophobic surfaces (SHS) with the "lotus effect", which protects surfaces from contamination [21-23]. The term “superhydrophobic” represents a contrasting property to the previously mentioned “hydrophilic”, characterized by being extremely difficult to wet and exhibiting a strong ability to repel water. This approach typically involves modifying surface morphology and chemical properties to impart superhydrophobic characteristics, thereby replicating the self-cleaning properties of lotus leaves. Droplets exhibit the Cassie-Baxter wetting state on SHS, characterized by contact angles greater than 150°, where the liquid sits partially on the solid surface while being supported by trapped air pockets, resulting in minimized solid-liquid contact area [24]. Specifically, in the Cassie-Baxter

state, droplets are partially supported by surface nano/micro-structures and partially suspended on air pockets beneath the droplets [25-28]. The presence of these air pockets minimizes the effective contact area between the liquid (e.g., bacteria-laden droplets) and the surface, thereby reducing interfacial adhesion forces. In contrast, previous studies have indicated that the absence of air pockets can significantly promote bacterial adhesion [29-32]. Furthermore, naturally SHS promoting the Cassie-Baxter wetting state (e.g., cicada wings) have demonstrated bactericidal properties attributed to the direct puncturing of bacterial membranes by their rigid surface nanopillars [33, 34]. Consequently, this wetting characteristic is commonly integrated into strategies aimed at reducing bacterial adhesion via SHS [35-37]. Nonetheless, the destruction of surface roughness structures and the loss of low surface energy coatings can compromise superhydrophobicity, and air pockets may become unstable under high-performance pressures [38-40]. These factors can impact the longevity and effectiveness of conventional SHS in maintaining anti-biofouling properties, which is particularly acute since SHS inherently lack antimicrobial properties [41]. In contrast, the other type of water repellent surfaces is liquid-infused surfaces (LIS), which involve infusing a lubricating liquid into a microstructured substrate to create a low-adhesion liquid surface [42, 43]. This feature facilitates lubrication, effectively preventing bacterial adhesion and subsequent biofilm formation [44-46]. Compared to common superhydrophobic surfaces, LIS exhibits significant advantages, including minimal contact line pinning (a phenomenon where the contact line, the intersection of the liquid,

solid, and gas phases, becomes immobilized due to surface heterogeneities), reduced interfacial friction, and independence from air pockets [47, 48]. All these characteristics contribute to its potential performance in anti-biofouling applications. However, similar to superhydrophobic surfaces, the commonly made LIS generally lack intrinsic bactericidal capabilities [45, 49], which limits their antibiofouling efficiency unless combined with cytotoxic chemicals or antimicrobial agents such as quaternary ammonium salt ionic liquids and silver nanoparticles. Typically, LIS without antimicrobial agents reduce bacterial adhesion by 70–80%, while those incorporating antimicrobial agents can achieve close to 100% bactericidal efficiency.

To overcome the two mentioned challenges of bacteria adhesion and the need for additional chemicals or agents to achieve bactericidal effects, this thesis proposes the combination of zinc oxide nanopillar structures with biomimetic water-repellent surface treatments. This approach allows one to achieve inherent bactericidal properties while preventing the initial bacterial adhesion and biofilm formation.

1.2 Research aims and objectives

This thesis aims to obtain functional ZnO surfaces with water-repellency characteristics for anti-biofouling applications. The anti-biofouling results should be supported by comprehensive material and interface characterization, as well as bacterial viability and attachment experiments. Additionally, this study will involve developing a protocol for the experimental measurement of droplet adhesion, which will provide further understanding of the fundamental behaviours of droplet wetting,

adhesion, and impact dynamics by manipulating the interaction between droplets and surfaces. The following objectives are specified to support the overall aim:

1. Fabricate ZnO nanopillar structures and explore surface modification methods to optimize their water repellency for better durability and longevity.
2. Evaluate the water repellency of the synthesised samples. This will include static and dynamic contact angle measurements, droplet adhesion force instrument tests, and high-speed camera droplet impact dynamics tests.
3. Examine the antibiofouling properties of the synthesised surfaces against various bacteria. This includes live-dead assays using confocal microscopy, Scanning Electron Microscopy (SEM) observation of bacterial morphology, Colony-forming Units (CFU) counting, and bacterial adhesion rate calculations.

1.3 Thesis outline

This thesis is organised into six chapters:

Chapter 1 presents the overall research background and motivation for the application of water-repellent surfaces in biofouling environments and also discusses the potential application prospects of ZnO as material for sample fabrication. This is followed by a statement of the research aims and objectives, and an identification of the thesis structure.

Chapter 2 reviews the theories and principles of different wetting conditions. It also examines the mechanisms of biofouling, natural water-repellent bactericidal surfaces and the latest advances in research on ZnO surfaces with antibiofouling properties.

Chapter 3 details the fabrication and optimization of biomimetic cicada wing-inspired ZnO nanopillars. The hydrothermal synthesis parameters and reaction environment were optimized to achieve the preparation of ordered and uniform nanopillar arrays. The fabricated ZnO nanopillars were characterized using SEM, atomic force microscopy (AFM), and X-ray diffraction (XRD) to evaluate their structural integrity, crystallinity, and surface morphology. These optimized ZnO nanostructures lay the foundation for subsequent studies on wettability, droplet impact dynamics, and anti-biofouling properties in subsequent chapters.

Chapter 4 proposes a biomimetic superhydrophobic surfaces based on ZnO nanopillars fabricated in Chapter 3. The fabricated samples were subjected to material characterization, wettability tests, and droplet impact dynamics tests. Additionally, antibiofouling tests were conducted using two common infectious bacteria *Staphylococcus aureus* (*S. aureus*) and *Escherichia coli* (*E. coli*) to examine and compare the durability of the surface treatments under different bacterial infections.

Chapter 5 reports on a biomimetic lubricant-infused surface based on nanopillar structures of ZnO. Building upon the findings of photocatalysis in Chapter 4, diffuse reflectance spectroscopy is supplemented to elucidate the origin of the bactericidal properties of the samples. The antibiofouling performances are evaluated using two bacteria with different biofilm formation mechanisms, *E. coli* and *Pseudomonas syringae pv. syringae* (*Pss*). An enhanced bacterial attachment assay, by quantifying the number of bacteria adhering at different washing methods, is used to optimize the

calculation of bacterial adhesion rate.

Chapter 6 summarizes the main findings and discusses the conclusions of the research works presented in this thesis. Some potential opportunities and directions of future research are also outlined.

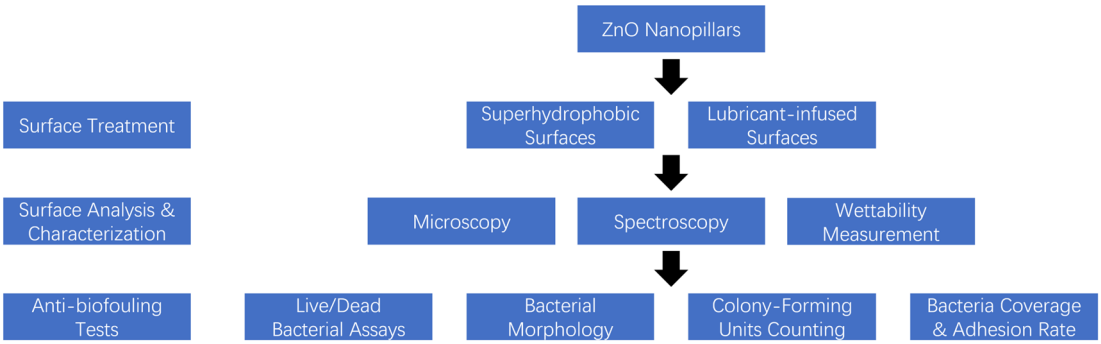

Figure 1.1. Research structure of the thesis.

1.4 Publications

- Navdeep Sangeet Singh, **Jitao Zhang**, Jason Stafford, Carl Anthony and Nan Gao*, "Implementing Superhydrophobic Surfaces within Various Condensation Environments: A Review", *Adv. Mater. Interfaces* **2021**, 8 (2), 2001442
- **Jitao Zhang**, Georgia Williams, Thanaphun Jitniyom, Navdeep Sangeet Singh, Alexander Saal, Lily Riordan, Madeline Berrow, James Churm, Manuel Banzhaf*, Felicity De Cogan* and Nan Gao*, "Wettability and Bactericidal Properties of Bioinspired ZnO Nanopillar Surfaces", *Langmuir* **2024**, 40, 14, 7353–7363
- **Jitao Zhang**, Diana Vinchira-Villarraga, Thanaphun Jitniyom, James Churm, Mojgan Rabiey* and Nan Gao*, "Lubricant-infused surfaces with inherent antibacterial properties". The manuscript is currently under 1st revision peer review by an Elsevier journal.

- Thanaphun Jitniyom, Georgia Williams, **Jitao Zhang**, Miguel Navarro-Cía, James Churm, Manuel Banzhaf and Nan Gao*, “Functional of double re-entrant and ZnO-NPs prevent wetting and antimicrobial properties”. This manuscript is in preparation for submission to a journal.

CHAPTER 2 LITERATURE REVIEW

2.1 Wetting behaviour

Wetting is a fundamental concept in fluid dynamics and surface science, which plays a crucial role in natural phenomena and various human activities. The wetting behaviour between solid and liquid is partially determined by the surface energies. Surface energy is the energy required to break the intermolecular forces when a surface is created [50]. In solid-state physics, surface atoms possess higher energy than interior atoms due to their reduced coordination, which leads to unsatisfied bonds. Although individual atoms in a crystalline solid are generally fixed in the lattice, the overall system tends to minimize its free energy through processes such as surface reconstruction and the adsorption of liquid molecules. When a solid contacts a liquid, the liquid molecules adsorb onto the solid surface, effectively reducing the high surface energy and allowing the liquid to spread. This phenomenon is known as wetting, and the ability of a liquid to spread on a solid surface is referred to as wettability.

2.1.1 Young's contact angle and dynamic contact angles

The common way to evaluate the wettability of a solid material is to measure the equilibrium contact angle of water droplet which spread on its surface [27].When liquid drops adhere to a solid surface, it is generally considered that the contact point is a three-phase contact, and the surface tension of different phases, solid-liquid (*sl*), liquid-vapor (*lv*) and solid-vapor (*sv*) at the interface of contact need to be considered, as shown in Figure 2.1. The contact line and area can move during the spreading, either

growing or shrinking and it indicates that the free energy (expressed by interfacial tension) of the three-phase interface has reached equilibrium once the change stops [51]. The equilibrium contact angle is the angle between the surface tangent on the liquid–vapor interface and the tangent on the solid–liquid interface at their intersection under this equilibrium state.

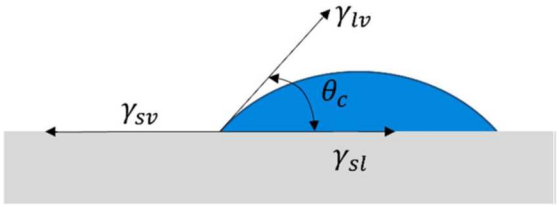

Figure 2.1. Diagram showing the governing surface tension vectors acting at the droplet's three-phase contact line. The contact angle (θ_c) denotes the surface wettability, γ is the surface tension and *sv*, *sl* and *lv* mean different interface phases.

Ideally, the relationship between contact angle and three interfacial tensions is given by Young's equation, where θ_c is the equilibrium contact angle (°) and γ is the surface tension (N/m). Subscripts *sv*, *sl* and *lv* mean different interface phases mentioned above:

$$cos\theta_c = \frac{\gamma_{sv}-\gamma_{sl}}{\gamma_{lv}} \tag{2.1}$$

This equation shows that the equilibrium contact angle is a function of the free energy (surface tension) of the three-phase interface, which is related not only to the properties of the solid, but also to the properties of the liquid-vapor interface. A rough evaluation of the wettability of a solid can be made by measuring the contact angle, as the minimum contact angle is 0° and the maximum is 180°. The smaller the contact

angle, the better the wettability of the solid. In recent studies, surfaces with a contact angle greater than 90° are referred to as hydrophobic, while those exceeding 150° are described as superhydrophobic. Conversely, surfaces with a contact angle less than 90° are termed hydrophilic, and those with an angle below 10° are classified as superhydrophilic, as shown in Figure 2.2 [52].

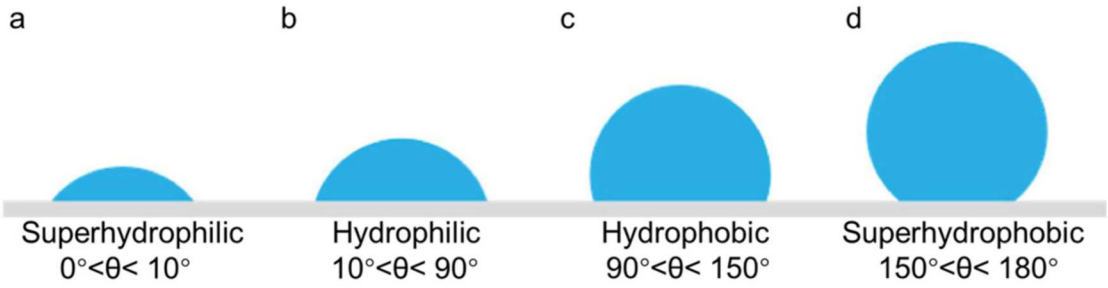

Figure 2.2. Classification of surface wettability based on θ_c: (a) superhydrophilic ($\theta_c < 10^{\circ}$), (b) hydrophilic ($10^{\circ} < \theta_c < 90^{\circ}$), (c) hydrophobic ($90^{\circ} < \theta_c < 150^{\circ}$) and (d) superhydrophobic ($\theta_c > 150^{\circ}$) [52].

This equilibrium contact angle obtained usually called Young's contact angle or static contact angle. In addition to the static contact angle, the wettability of the liquid drops on the solid can be further verified by measuring the dynamic contact angle, which include advancing angle, receding angle, and sliding angle. Sliding angle, as the name implies, is the angle at which the droplet starts to slide after the solid is tilted, as shown in Figure 2.3 [53]. The lower the sliding angle on solid, the easier the droplet is to move.

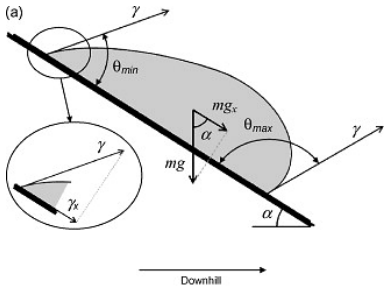

Figure 2.3. Schematic diagram of droplet sliding angle on solid surface [53].

Unlike the idealized premise of Young's contact angle, surfaces in the real world do not exhibit perfect surface characteristics, therefore the contact angles of the front and rear of the droplet may change during the sliding motion, and these front and rear angles are called the advancing angle and the receding angle respectively. The maximum dynamic contact angle is called the advancing contact angle (θ_a) and the minimum dynamic contact angle is called the receding contact angle (θ_r). The difference between these two angles is known as contact angle hysteresis, which is important for understanding surface roughness and inhomogeneity [26]. The overall effect can be viewed as being very similar to static friction, which the smaller the contact angle hysteresis, the less work per unit distance required to move the contact line, the more hydrophobic the solid surface is. Typically, advancing and receding contact angle (contact angle hysteresis) are measured by needle-in method, as shown in Figure 2.4 [54].

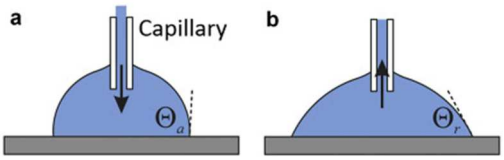

Figure 2.4. Schematic diagram of (a) advancing and (b) receding contact angle measurements using needle-in method [54].

In this measurement method, a droplet is placed on the surface using a syringe, which is kept within the droplet [55]. Liquid is injected at a constant rate to increase the droplet volume. Initially, the contact angle increases with the droplet volume while the solid-liquid contact line remains stable. As more liquid is injected, the solid-liquid contact line begins to advance on the surface, and the contact angle stops increasing and reaches a constant θ_a . The θ_r is measured in the opposite manner by removing liquid from the static droplet at a constant rate. The droplet volume and contact angle decrease initially, but the contact line remains stable. The θ_r is reached when the contact angle stabilizes, when the contact line decreases, and the droplet begins to recede.

2.1.2 Wenzel and Cassie-Baxter wetting models

The generation of Young's model allows one to discuss the wetting state of sessile droplets on an ideally smooth flat surface, but the wetting phenomenon on surfaces in the real world are vary due to the differences of surface roughness. In fact, it can be divided into homogeneous and heterogeneous by defining roughness, and the corresponding wetting models are Wenzel model and Cassie-Baxter model (Figure 2.5).

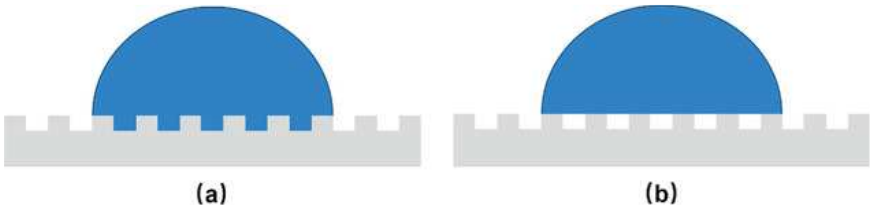

Figure 2.5. Schematic diagram of a droplet on solid substrate in the (a) Wenzel and (b) Cassie–Baxter state.

To address the limitations of Young's model, Wenzel introduced a refined approach in 1936 to account for the influence of surface roughness on the droplet contact angle [56]. In this case, the droplets penetrate the grooves of the surface and fill the rough structures [57]. Therefore, when the rough surface below the droplet is completely wetted by the liquid, the equation for the apparent contact angle can be written as the equation, where θ_w is the Wenzel contact angle (°), γ is the surface tension (N/m) and r is the roughness factor, which is the ratio of actual area to apparent area of the solid surface:

$$cos\theta_w = \frac{r(\gamma_{sv}-\gamma_{sl})}{\gamma_{lv}} = rcos\theta_c \quad (2.2)$$

It can be seen from the variant in Equation 2.2 that the apparent contact angle in Wenzel's model and the ideal contact angle in Young's model can be linked through the surface roughness factor.

The Wenzel model is only valid for the homogeneous wetting state since it assumes that the liquid wets the surface roughness structure completely. Therefore, another model is needed to discuss the mechanism of liquid under heterogeneous wetting, that is, air can be trapped in the surface roughness structure under the droplet to form air pockets. Cassie and Baxter [58, 59] developed an alternative model to explain this mechanism by relating the apparent contact angle to the composite interface as shown below:

$$cos\theta_{CB} = \varphi_S cos\theta_c - (1 - \varphi_S) \quad (2.3)$$

where θ_{CB} is the apparent contact angle and φ_S is the dimensionless fraction of the

solid surface area in contact with the liquid, then $1-\varphi_S$ is the air gaps. When $\varphi_S = 1$, it can be considered that the liquid completely contacts with the solid surface, and the surface is completely wetted, thus becoming the Wenzel equation. One situation to induce this transition from the Cassie-Baxter to the Wenzel state is by applying sufficient pressure to the droplet, causing it to penetrate the air gaps on the superhydrophobic surface. Alternatively, heating the surface can also facilitate this transition. As the pressure within the water-air gaps increases, the droplet evaporates and subsequently condenses into these gaps.

2.1.3 Droplet adhesion

The wetting behaviour of droplets directly impacts their adhesion force on surfaces, as the interaction between the droplet and the surface is fundamentally governed by the force balance at the liquid-solid interface. The capillary forces oppose the droplet during its sliding process, resulting in a frictional motion. These capillary forces are related to the difference in contact angles at the rear and front of the droplet. The lateral adhesion force F_{LA} is determined by the liquid-vapor surface tension (γ_{lv}) and the apparent rear (θ_{Rear}) and front (θ_{Front}) contact angles of the droplet:

$$F_{LA} = k * L * \gamma_{lv} * cos\theta_{Rear} - cos\theta_{Front} \quad (2.4)$$

Gao et al.'s research demonstrates that the lateral adhesion of droplets on solid surfaces can be divided into static and dynamic states, analogous to static and kinetic friction in solids, as shown in Figure 2.6 [60]. As the lateral adhesion force increases, the droplet remains stationary until a critical threshold is reached. Upon surpassing this

threshold, the droplet transitions to a dynamic state and begins to move with a constant force required to sustain its movement.

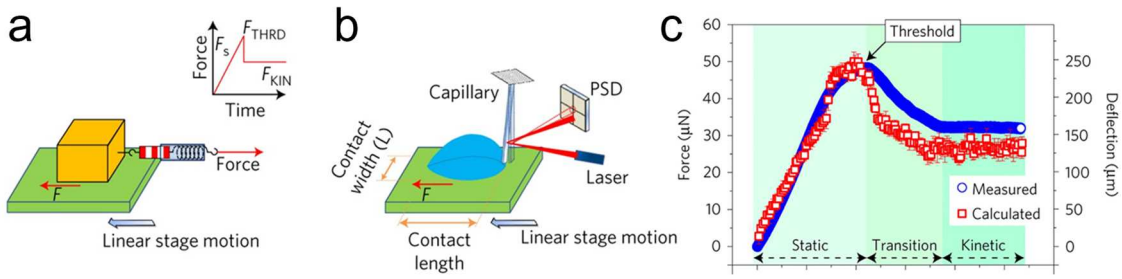

Figure 2.6. (a) Textbook configuration for demonstrating solid–solid friction. (b) Homemade set-up for measuring liquid–solid friction. (c) The measured lateral adhesion force is plotted with blue circles and the calculated force is plotted with red squares [60].

Schnell et al. investigated the lateral adhesion force of droplets on laser-structured surfaces based on the foundation of Gao's work [61]. The results demonstrated that the mobility of droplets on laser-structured surfaces at different motion stages is consistent with previous study, as shown in Figure 2.7 and Figure 2.8. Figure 2.7(a–e) illustrates how the surface topography evolves from reference (REF) to self-organized nanostructure (LIPSS), self-organized microstructure (MICRO), laser-inscribed (TRENCH) and hierarchical (TRENCH + LIPSS) design. The REF sample displays a relatively smooth morphology with minimal height variation. In contrast, the LIPSS sample reveals periodic nanoripples oriented in parallel lines, resulting in moderate undulations in the height profile. The MICRO sample exhibits larger, microscale asperities, indicating a more pronounced roughness. The TRENCH design features

well-defined laser-etched grooves, while TRENCH+LIPSS combines both micro- and nano-scale structures. Correspondingly, Figure 2.8(a–j) shows friction force measurements in the transverse direction (CD) and longitudinal direction (ID). The REF surface exhibits isotropic behaviour with similar force curves in both directions. In contrast, the LIPSS and MICRO surfaces exhibit moderate stick-slip behaviour, especially in CD direction. The adhesion forces measured on TRENCH differ more significantly in the CD and ID directions, suggesting that the grooves can impact droplet motions. Finally, the droplets on the TRENCH + LIPSS design show the most significant direction dependence, characterized by larger forces and more pronounced stick-slip in the transverse line direction. The chemical composition and topographical design of the surfaces significantly influence the droplet's adhesion and mobility. Topographical design and surface chemistry affect surface roughness and energy respectively, both of which are key parameters determining surface wettability. Wang et al. fabricated surfaces with varying roughness in range of 5 - 20 μm by polishing Teflon plates and investigated the contact angle hysteresis and droplet spreading behaviour [62]. The results demonstrated that within the examined range of surface roughness, an increase in roughness initially led to a continuous decrease in contact angle hysteresis, reaching a minimum value, after which it began to increase. The trend in spreading work as a function of surface roughness was found to be analogous to the observed variations in contact angle hysteresis, as shown in Figure 2.9. As the roughness increases from about 5 to about 14 microns, the contact angle hysteresis

decreases significantly from about 50˚ to 5˚, indicating that intermediate roughness reduces droplet pinning sites, thereby easing the movement of the liquid on the surface. This trend is also reflected in the change in work, which reaches a minimum at approximately the same intermediate roughness, indicating that there is an optimal balance between liquid-solid and liquid-liquid interactions, which reduces droplet adhesion and makes it easier to roll off. Beyond this roughness threshold, further increases in roughness restore higher hysteresis, indicating that the re-emergence of pinning or trapped air pockets increases the resistance to droplet movement. Furthermore, the application of specific coatings can significantly alter surface energy [63]. For instance, low-surface-energy coatings such as fluoropolymers (e.g., PTFE), silane-based compounds (e.g., FAS-17), and PDMS can drastically reduce wettability, leading to water-repellent surfaces with water CA over 150˚. Conversely, high-surface-energy coatings like metal oxides (e.g., TiO_2, ZnO), plasma-treated polymers, and hydrophilic polymer coatings (e.g., PEG-based materials) can enhance wettability, decreasing the water CA on surfaces. These coatings can create surfaces that either strongly repel or attract water, thereby controlling droplet adhesion. Superhydrophobic coatings, such as those made from fluorinated compounds, typically result in low adhesion forces, allowing droplets to roll off easily, whereas hydrophilic coatings, like those based on zwitterionic polymers, can cause droplets to spread and adhere more firmly.

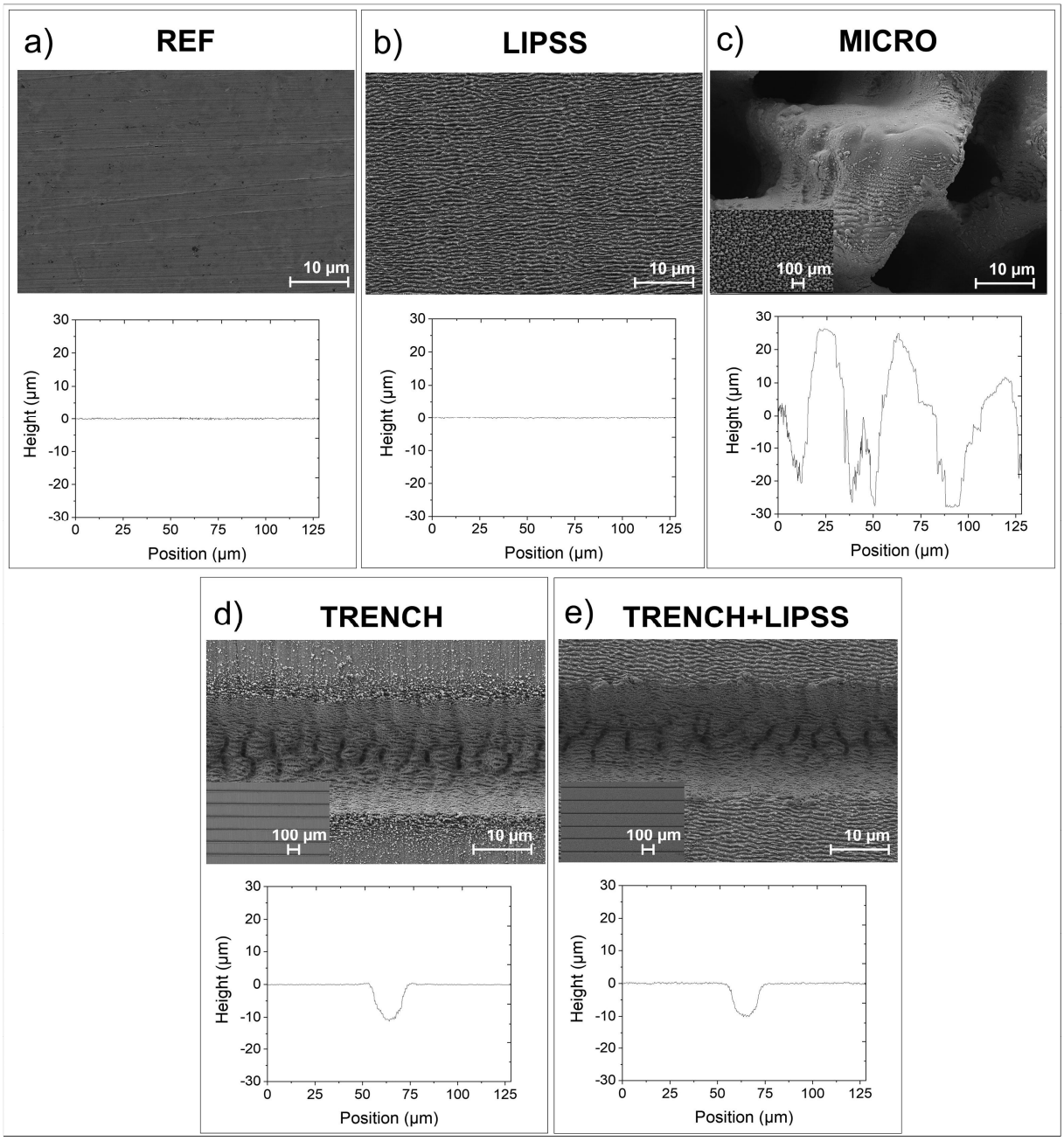

Figure 2.7. SEM images and CLSM data of the fluorinated surface: reference (REF), self-organized nanostructure (LIPSS), self-organized microstructure (MICRO), laser-inscribed (TRENCH) and hierarchical (TRENCH + LIPSS) design [61].

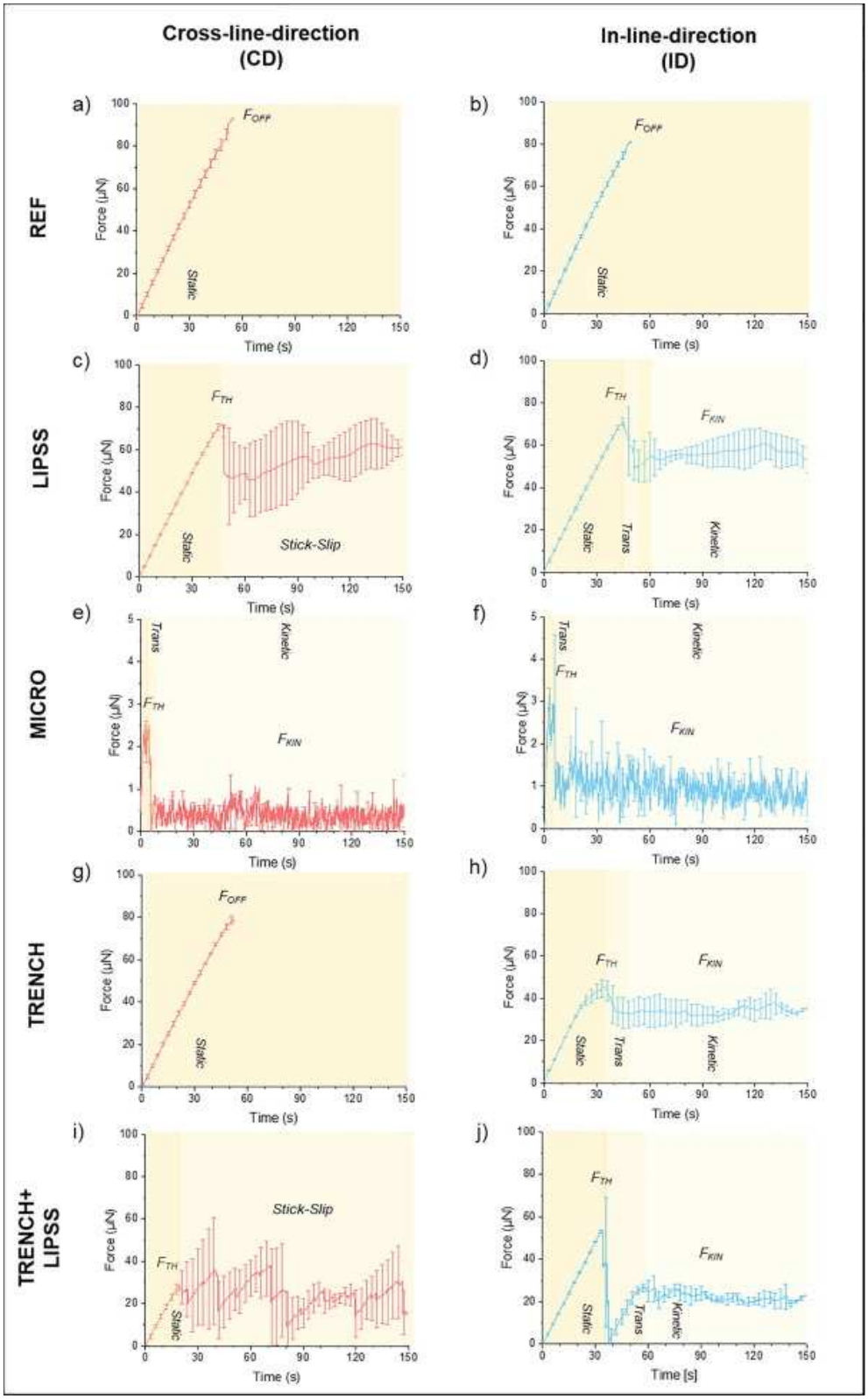

Figure 2.8. Results of droplet adhesion force investigations in two directions of droplet motion on different laser-structured surface designs [60].

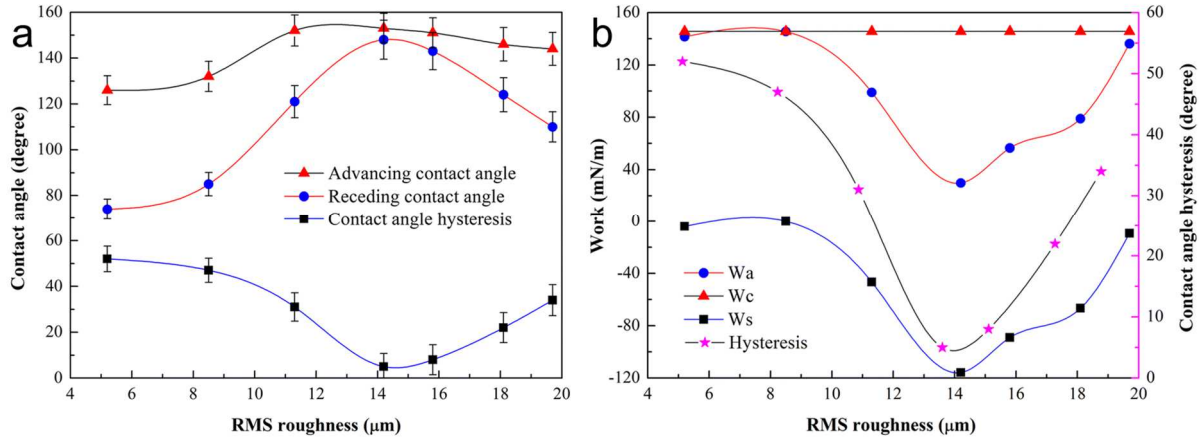

Figure 2.9. (a) Variation of advancing contact angle, receding contact angle, and contact angle hysteresis with RMS roughness. (b) Variation of adhesion work (*Wa*), cohesion work (*Wc*), spreading work (*Ws*), and contact angle hysteresis with RMS roughness [61].

2.1.4 Droplet impact

Wetting behaviour also determines the impact dynamics of droplets, as wettability affects the spreading and retraction behaviour of droplets on surfaces. Typically, the impact of a droplet on a surface causes the shape of the phase contact line to change, leading to deposition, rebound, or splashing [64]. The relative importance of inertial forces to surface tension during impact is commonly captured by the Weber number (*We*), as shown in Equation 2.5, where ρ is the fluid density (kg/m³), U is the impact velocity (m/s), D is the droplet diameter (m) and γ is the surface tension (N/m) [65].

$$W_e = \frac{\rho {U_0}^2 D}{\gamma} \tag{2.5}$$

Deposition occurs on superhydrophilic and hydrophilic surfaces, where the droplet spreads and wets the surface upon impact. Rebound or partial rebound occurs on hydrophobic or superhydrophobic surfaces, as shown in Figure 2.10 [66]. Each row

represents a silicon surface with laser-ablated microstructures but different wettability (achieved by fluoropolymer coatings of varying thickness) from superhydrophilic (<5°) in the top row to superhydrophobic (160°) in the bottom row, while each column shows the droplet shape at successive time steps (in ms) after impact (*We* = 3, D_0 = 2.3 mm, V = 0.3 m/s). On the superhydrophilic surface (first row), the droplet spreads quickly and remains flat with no rebound, as the low contact angle (<5°) promotes strong wetting and liquid-solid adhesion. As the contact angle increases through the hydrophilic state (e.g., 20°, 50°, 90°) to the final hydrophobic state (145°, 160°), the droplet spreads less and begins to retract more strongly. On the 145° CA hydrophobic surface, partial rebound can be observed, that the droplet retracts slightly and rises but may not completely detach from the surface. Finally, on superhydrophobic surfaces (bottom row, 160°), droplets exhibit significant rebound.

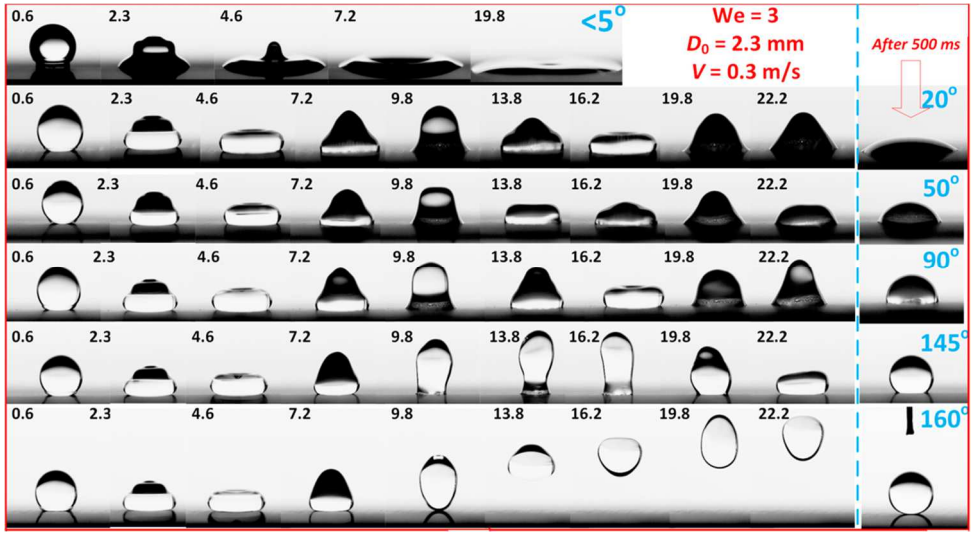

Figure 2.10. Droplet impacts on surface with fixed microstructure and different wettability from superhydrophilicity (first row, <5˚) to superhydrophobicity (last row, 160˚) in time and the unit of time in the figure is ms [66].

During this rebound process, the droplet's kinetic energy is converted into surface energy as it spreads upon impact, as shown in Figure 2.11 [67]. The droplet flattens due to inertia, with its height decreasing and spreading diameter increasing until it reaches its maximum spread. At this point, the contact area between the droplet and the surface is at its peak, and the droplet shape transitions from spherical to cap-shaped, eventually becoming pancake-shaped [68]. Subsequently, due to surface tension, the droplet begins to retract, releasing surface energy in the form of kinetic energy. The droplet's edges converge toward the centre under surface tension, causing the height to increase and the spreading diameter to decrease to zero. The droplet then extends vertically, potentially forming a jet and ejecting satellite droplets from the top. If the kinetic energy is sufficient to overcome the surface's adhesive forces, the droplet will rebound. Due to the gravity, the rebounded droplet may fall back and impact the surface again [69].

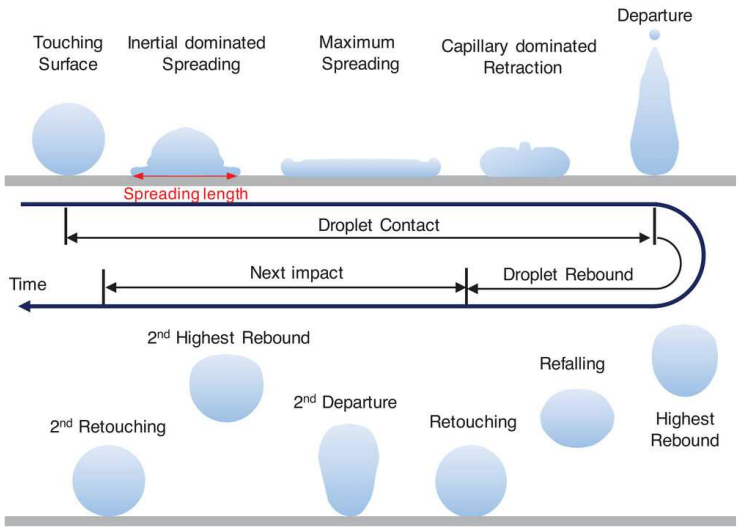

Figure 2.11. Schematic of the basic process of droplet impact on conventional superhydrophobic surfaces [67].

If the impact pressure of the droplet causes the liquid to penetrate (impale) the surface structure, partial rebound can occur even on micro-textured superhydrophobic surfaces [70]. At sufficiently high impact velocities, a transition from the Cassie-Baxter state to the Wenzel state may occur [71]. As the impact velocity increases on hydrophobic and superhydrophobic surfaces, the droplet may eject additional secondary droplets [72]. Further, the dynamics of droplet impact are critically influenced by several dimensionless numbers. For example, a high Weber number indicates that inertial forces dominate over surface tension forces, which can lead to phenomena such as droplet breakup, splashing, or spreading [71, 73, 74]. Zhou et al. investigated the dynamic wetting behaviour of sodium dodecyl sulfate droplets with varying diameters, speeds, and concentrations impacting superhydrophobic solid surfaces, which provided insights into the influence of surface properties, droplet impact velocity, and droplet size on the impact dynamics [75].

2.2 Natural water-repellent surfaces

In nature, water-repellent surfaces are widely found in both plants and animals [24]. Some of these surfaces exhibit remarkable self-cleaning and anti-fouling properties, providing abundant inspiration for the design of artificial structures.

Lotus leaf is a well-known example of a superhydrophobic surface [22, 76]. It exhibits extraordinary water repellency and self-cleaning properties through its hierarchical structure and epidermal wax, commonly referred to as the "lotus effect." This phenomenon has inspired the design and development of artificial water-repellent

surfaces [22, 77]. Scanning electron microscopy reveals that the lotus leaf surface has a microscale rough structure covered with nano-scale protrusions [78]. These micro-nano structures create a complex hierarchy that allows water droplets to contact only the tips of these protrusions, forming a Cassie-Baxter wetting state, which facilitates droplet rolling.

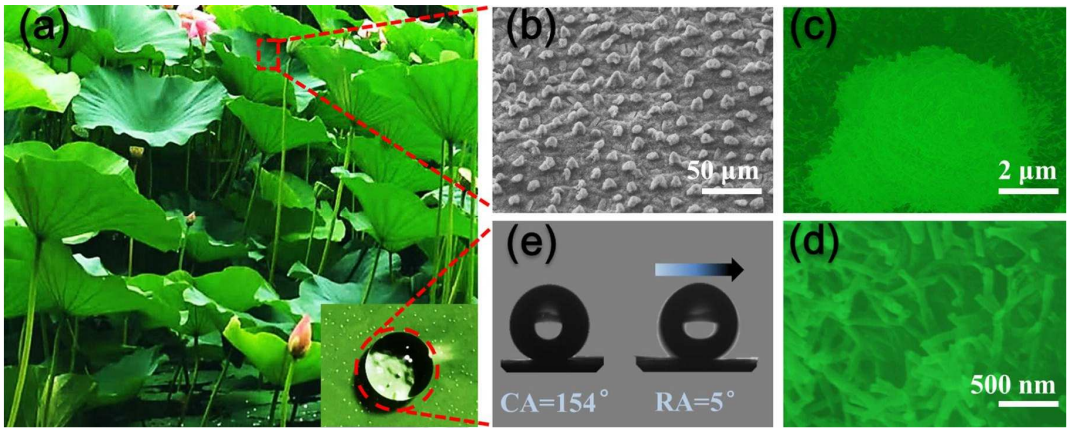

Figure 2.12. Images of the lotus leaf and water droplet on the surface. (a) Typical digital photographs of superhydrophobic lotus leaves and the water droplet on the lotus leaf. (b) SEM image of the lotus leaf tilted at an angle of 45°. (c, d) Magnified SEM images of a single papilla (c) and nanotubes (d). (e) The CA and RA of the lotus leaf. The pictures (c, d) are processed with false-colour [78].

Furthermore, subsequent studies have shown that the lotus leaf surface is coated with a layer of wax, which could be considered as a low surface energy material with a surface energy value around 20–30 mJ/m² [79]. The wax layer further reduces the contact area between water droplets and the leaf surface, enhancing the water repellency. Evidence for this can be seen in the significant decrease dropping by as much as 140˚ in contact angle and the consequent loss of superhydrophobicity when

the wax on leaves was damaged or removed [80]. Both rice and lotus leave exhibit superhydrophobicity through multi-layered micro/nanostructures, but their specific surface morphologies are significantly different. Lotus leaves typically have densely packed micronized papillae (bump-like structures) topped with nanoscale wax crystals creating a multiple scale. In contrast, rice leaves exhibit more pronounced parallel ridges or grooves at the micrometre scale, interspersed with nanoscale wax particles that form patchy layers along these ridges, as shown in Figure 2.13 [81]. This combination of micro and nano structure also reduces the contact area of water droplets, allowing them to form a high contact angle on the surface. However, rice leaves predominantly facilitate line contact through these ridge structures, although point contact may occasionally occur depending on the droplet's size, shape, or orientation relative to the ridges. Evidence of this can be seen in the significantly different sliding angles for droplet movement in two directions on rice leaves, which are 3˚ on longitudinal direction and 9˚ on lateral direction with irregularly arranged morphography [81].

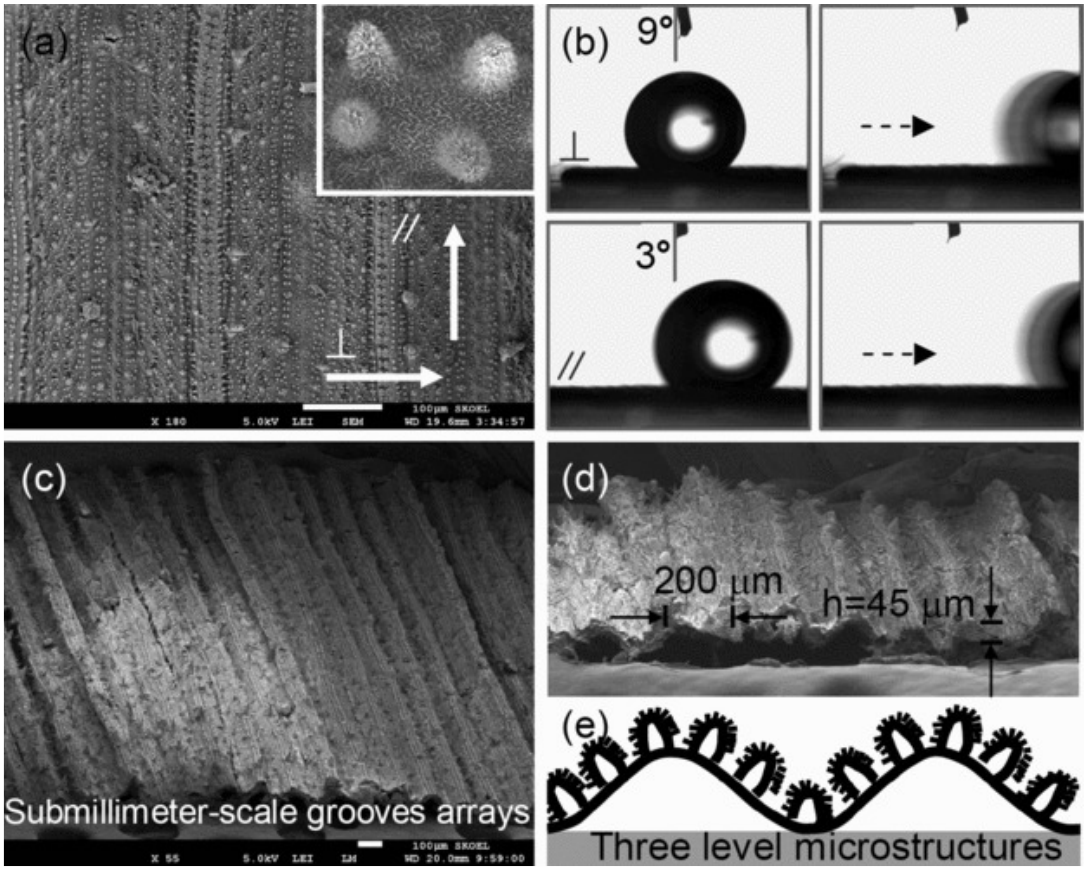

Figure 2.13. The anisotropic wetting of a rice leaf and the sub-millimetre-scale groove arrays. a) Top-view SEM image of the rice leaf. The inset is the magnified image of dual-size structures; micrometre-scale papilla and nanostructures. b) The anisotropic sliding property of the rice leaf. c) 60°-tilted-view SEM image of the rice leaf. d) Cross-sectional SEM image of the macrogrooves; width=200 μm and height=45 μm. e) Proposed three-level model of the rice leaf [81].

Additionally, some other plant leaves such as maize leaves and fern leaves, exhibit superhydrophobicity similar to those of rice leaves but with subtle variations in structure and performance [82, 83]. The surface of maize leaves features longitudinally arranged micron-scale ridge structures, also covered with fine wax particles, as shown in Figure 2.14a. Similar to rice leaves, these ridge structures on maize leaves create line contact

for water droplets, although the ridge structures are generally more regular and uniform. Fern leaves, on the other hand, are typically covered with micron-scale papillae structures and fine wax particles, as shown in Figure 2.14b. These papillae structures resemble small "bumps", forming numerous tiny air pockets that prevent water droplets from spreading out on the surface.

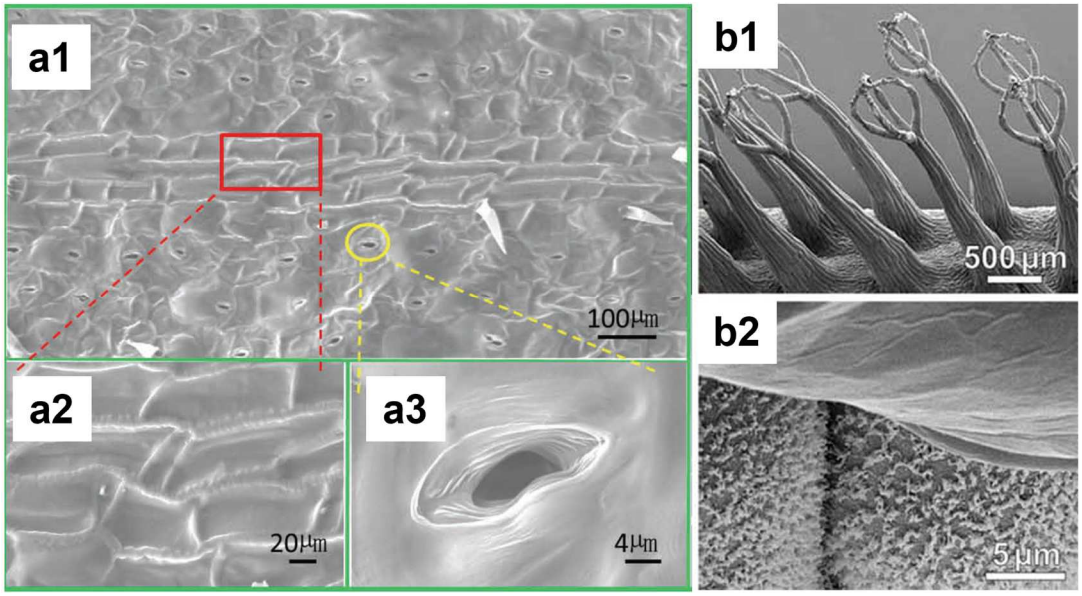

Figure 2.14. SEM images of (a) maize leaves and (b) fern leaves.

It is worth noting that water droplets on rose petals also exhibit a high contact angle, but unlike the aforementioned plant leaves, they show higher adhesion to the droplets, displaying high contact angle hysteresis, as shown in Figure 2.15 [84].

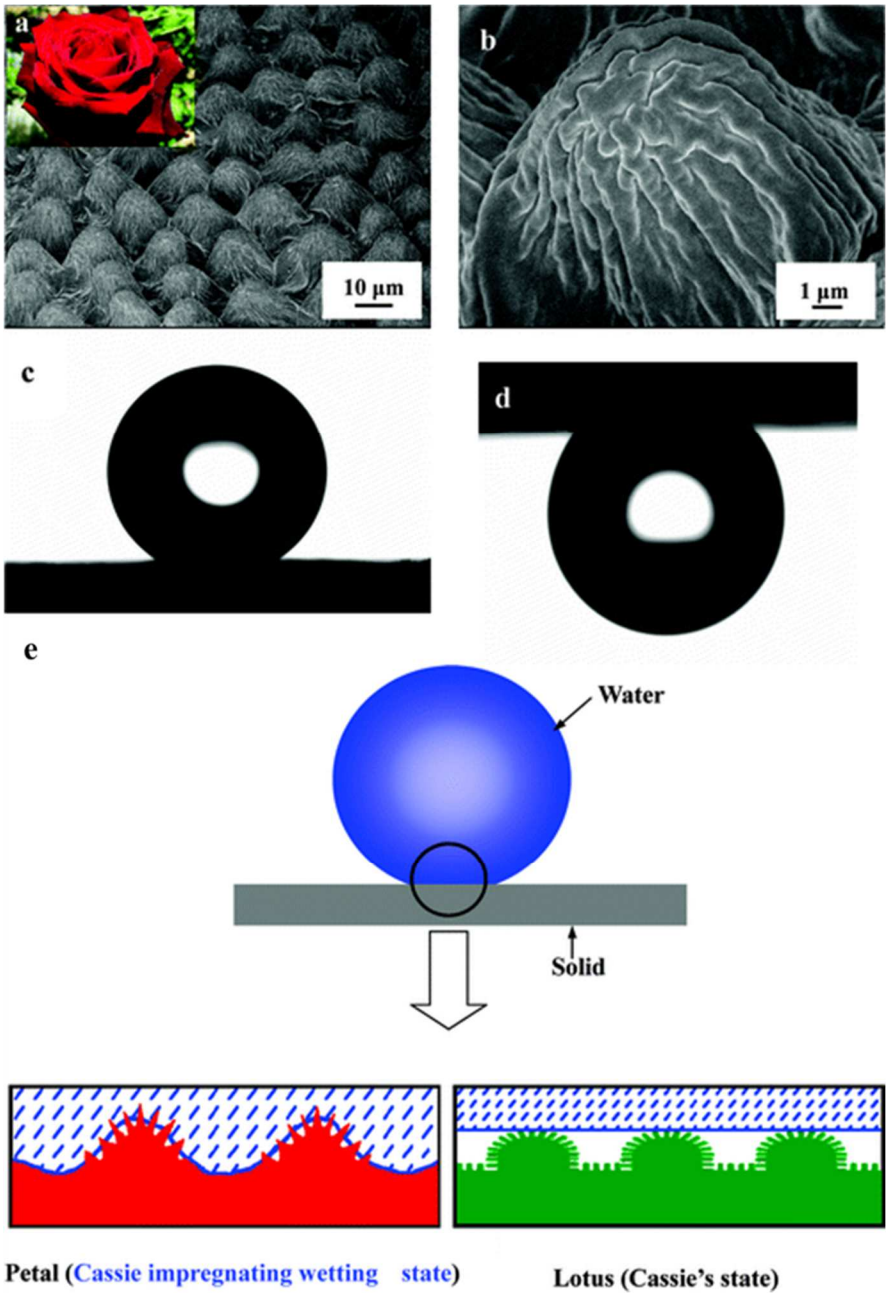

Figure 2.15. SEM images of the surface of a red rose petal, showing (a) a periodic array of micropapillae and (b) nanofolds on each papillae top. (c) Shape of a water droplet on the petal's surface, indicating its superhydrophobicity with a contact angle of 152.4°. (d) Shape of water on the petal's surface when it is turned upside down. (e) Schematic illustrations of a drop of water in contact with the petal of a red rose (the Cassie impregnating wetting state) and a lotus leaf (the Cassie's state) [84].

Another plant that has inspired the development of artificial water-repellent surfaces is the Nepenthes pitcher plant [43]. It retains an intermediate liquid within the rough microstructures of its inner walls, creating a continuous liquid surface. SEM reveals neatly arranged micron-sized groove structures, each containing directionally aligned microcavities (Figure 2.16) [85, 86]. Drawing inspiration from this mechanism, Wong et al. developed Slippery Liquid-Infused Porous Surfaces (SLIPS) by infusing a lubricating liquid into a porous solid matrix [43]. The smooth interface generated by the liquid-infused surfaces can eliminate droplet pinning and enable droplets to slide at small sliding angles (less than 5°). Furthermore, these surfaces exhibit a self-healing mechanism due to capillary forces, which allows them to restore their slippery properties when damaged [43].

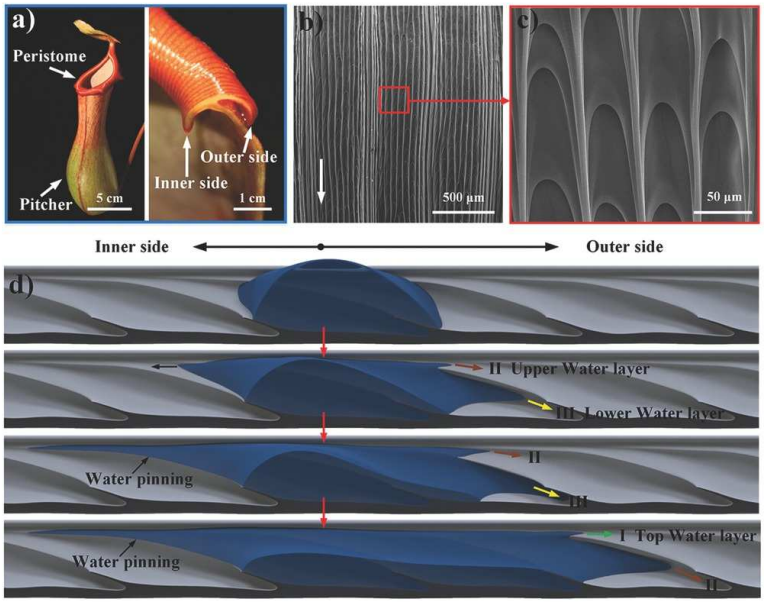

Figure 2.16. (a) Optical images of a pitcher of Nepenthes alata (left) and its cross-section (right). (b, c) SEM image of the peristome surface and its magnified image showing two-order microgrooves and periodic duck-billed microcavities scattering

along the second-order microgroove. The arrow in (b) shows the direction toward the inner side. (d) Three-dimensional illustration of the water-transport process. A strong water rise induced by the gradient wedge of the overlapping microcavities results in continuous water transport toward the outer side. Water pinning at the sharp edge prevents water flowing toward the inner side [85, 86].

In addition, certain body parts of animals also exhibit water-repellent properties. For instance, the legs of water striders achieve superhydrophobicity through nanosized grooves on micron-sized hairs and a low surface energy keratin wax layer [87]. Furthermore, some insects' wings possess superhydrophobicity, which helps reduce dust adhesion and enhances their flight capabilities. Zheng et al. studied the directional adhesion on the wings of the butterfly Morpho aega [88]. SEM revealed that the wings are covered with numerous square micron-sized scales, which are periodically distributed radially outward from the central axis of the body (Figure 2.17). Each scale surface is adorned with numerous individual nano-sized ridges. Water droplets on the wing surface exhibit high contact angles over 150° and the butterfly can achieve directional cleaning by adjusting its wing posture to reversibly switch between different rolling and pinning states. Oh et al. investigated the surface structure and wettability of cicada wings from four different species, finding that they all possess nanopillar structures of varying heights (ranging from 50 nm to 400 nm) [89]. Water droplets exhibited superhydrophobicity on three of the cicada wings and hydrophobicity on last one, as shown in Figure 2.18. Additionally, Aideo et al. studied the hydrophobic

behaviour of dragonfly and damselfly wings, [90] discovering that their wing structures consist of micron-scale polygonal networks with randomly distributed nano-oval fibrils within the meshes. The hydrophobicity of dragonfly wings was slightly better than damselfly wings, with both contact angles ranging between 120° and 136°.

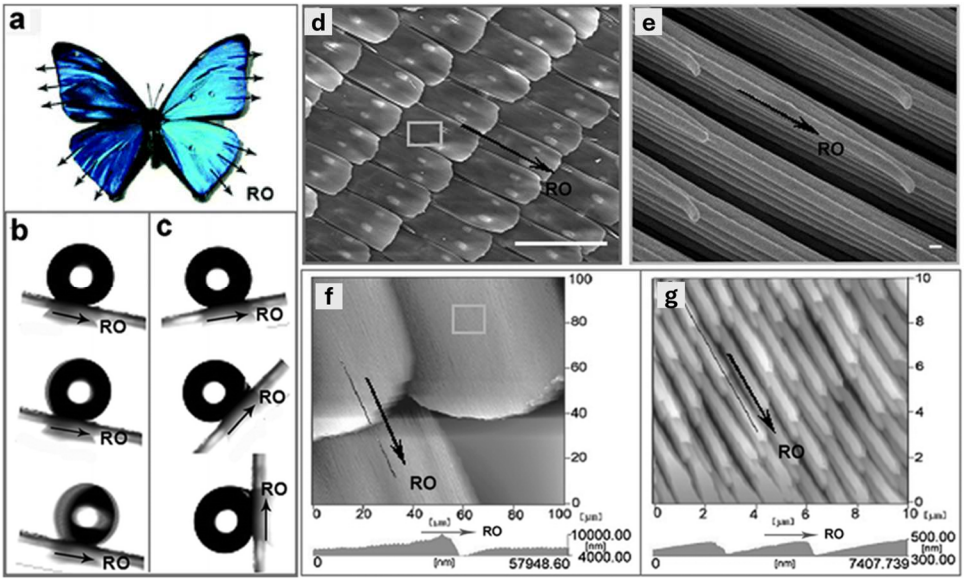

Figure 2.17. Directional adhesion on superhydrophobic butterfly wings. (a) An iridescent blue butterfly M. aega. The black arrows denote the radial-outward (RO) direction away from the body's centre-axis. (b) The droplet easily rolls along the RO direction when the wing is tilted toward downwards by 9°. (c) The droplet is firmly pinned on the wing that is tilted upward, even when fully upright. (d, e) SEM and (f, g) AFM images of hierarchical micro- and nanostructures on the surface of the wings [88].

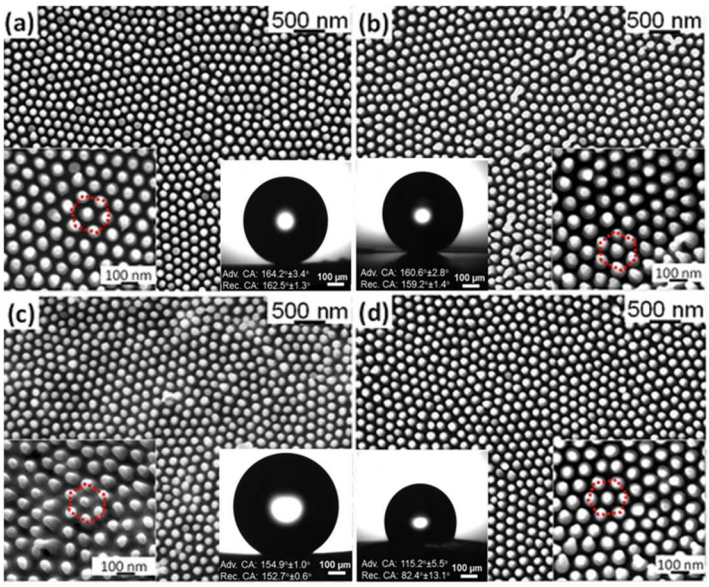

Figure 2.18. Top-view SEM image and contact angle of wings for (a) *N. pruinosus*, (b) *N. tibicen*, (c) *Me. dorsatus*, and (d) *Ma. septendecim* [89].

Moreover, it is noteworthy that some insect wing structures can even exhibit bactericidal properties. Ivanova et al. discovered that the nanopillar arrays on cicada wings possess bactericidal effects, capable of penetrating and killing attached *Pseudomonas aeruginosa* cells [91]. The bactericidal activity remained effective even after the cicada wing surface was coated with a 10 nm thick gold layer, indicating that the bactericidal properties stem from the physical characteristics of the wing surface rather than surface chemistry. Hasan et al. tested the bactericidal activity of cicada wings against seven different bacteria, finding that the wing structures were more effective against Gram-negative bacteria compared to Gram-positive bacteria, likely due to the thicker and more rigid peptidoglycan layer of Gram-positive bacteria [92]. Building on these findings, Pogodin et al. developed a biophysical model of cell interaction with the nanopillars on cicada wings, revealing that cell rupture occurs due

to excessive stretching of the cell membrane between the nanopillars [93]. They also found that Gram-positive bacterial cells could be made susceptible to the nanopillar bactericidal mechanism by reducing their rigidity through microwave radiation.

Furthermore, Bandara et al. found that dragonfly wings can effectively kill *Escherichia coli* [94]. Unlike the bactericidal mechanism of cicada wings, the bactericidal activity of dragonfly wings is achieved through strong adhesion between the nanopillars and the bacterial extracellular polymeric substances (EPS), and the subsequent shear forces generated by continued bacterial movement after fixation.

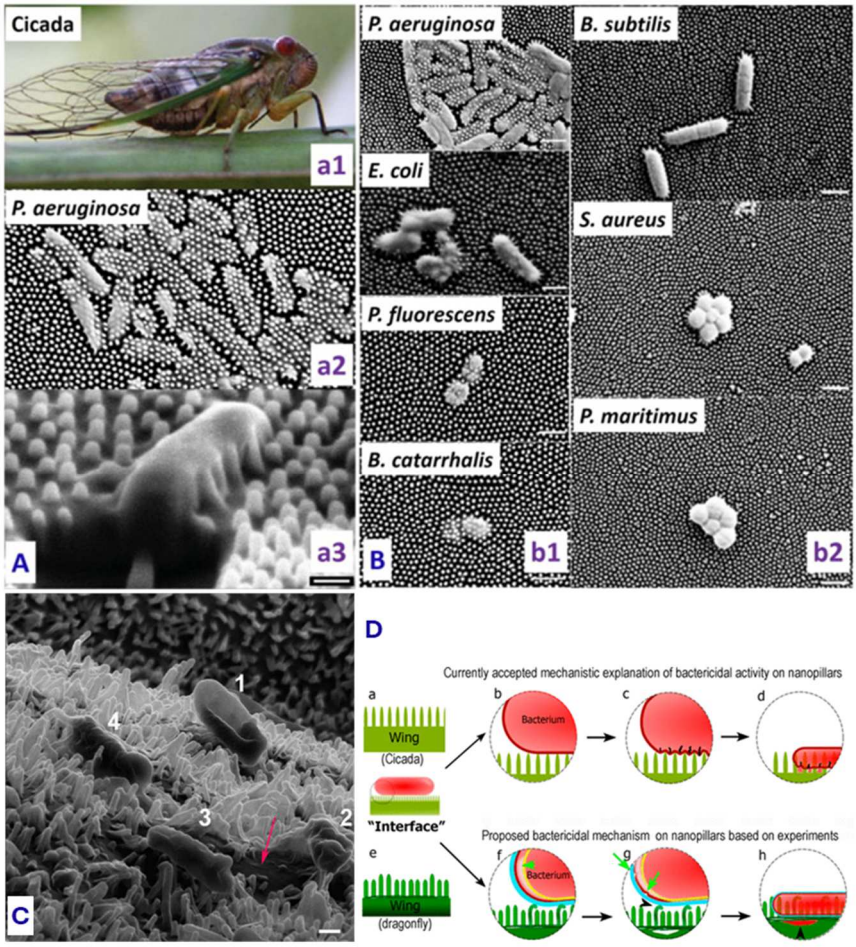

Figure 2.19. (A) (a1) Photograph of cicada insect (*Psaltoda claripennis*). (a2) *Pseudomonas aeruginosa* cells on the nanostructured cicada wing penetrated by the

nanopillar structures. (a3) Representative SEM image of a *Pseudomonas aeruginosa* cell sinking between the nanopillars on the cicada wing surface [91, 95]. (B) Selective bactericidal activity of the Cicada wing surface against (b1) Gram negative (*P. aeruginosa*, *E. coli*, *P. fluorescens*, *B. catarrhalis*) and (b2) Gram positive bacteria (*B. subtilis*, *S. aureus*, *P. maritimus*) [92, 95]. (C) Four different *Escherichia coli* bacteria attached on uncoated nanopillar surface of dragonfly wing indicate progressive dying stages and (D) Proposed mechanism of bactericidal activity of nanopillars [94].

2.3 Artificial water-repellent and antibiofouling surfaces

2.3.1 Mechanism of biofouling

Biofouling refers to the undesirable accumulation of biological materials such as microorganisms, plants, algae, and animals on surfaces. [96] In the healthcare industry, biofouling specifically refers to biofilms, which are structured community of microbial cells encapsulated within a self-produced polymeric matrix that adheres to a surface [1]. Sauer et al., through their research on *Pseudomonas aeruginosa*, proposed that biofilm formation follows a cyclical process occurring in five stages [97]. The first stage begins with planktonic (free-floating) cells initially attaching to a surface through weak and reversible interactions. Subsequently, as the cells adhere, they begin producing extracellular polymeric substances (EPS), which are composed of proteins, polysaccharides, and nucleic acids, leading to more stable and irreversible adhesion [1]. The EPS matrix protects the cells and allows them to communicate and coordinate through quorum sensing, a chemical signalling process. The biofilm then matures into

a structured community where differentiated cells can exhibit increased resistance to antibiotics and other antimicrobial agents. Eventually, cells from the biofilm may disperse to new surfaces, perpetuating the cycle, as shown in Figure 2.20a. Sauer et al. subsequently proposed a new, more inclusive model of biofilm formation to address the limitations of their original model [98]. These limitations include whether non-surface-attached bacterial aggregates are considered biofilms and the various environments and conditions of biofilm formations. Their new model summarizes biofilm formation into three stages. The first stage involves the initial aggregation or attachment of bacteria. Bacteria can adhere to surfaces, host tissues, or one another, forming initial clusters. This can happen via specific adhesin-mediated binding, EPS bridging, or entrapment in host or environmental polymers (such as mucus or corrosion products). In some cases, planktonic cells are continuously recruited to these nascent aggregates, especially in open systems where fresh cells enter with fluid flow. Bacterial colonies will then expand through growth and aggregation. Once initial clusters form, they expand through a combination of cell division, recruitment of additional cells, and ongoing EPS production. The biofilm architecture (such as flat layers, mushroom-like microcolonies, or suspended flocs) depends on multiple factors, including nutrient availability, flow conditions, and the nature of the surrounding environment (host tissue, industrial pipelines, soil particles, etc.). During this stage, microenvironments develop within the biofilm, leading to gradients in oxygen, nutrients, pH, and signalling molecules. These gradients can drive phenotypic diversification, antibiotic tolerance,

and complex interactions among different species when forming multispecies biofilms. In the final stage, bacteria can leave the biofilm either as aggregates or individual cells through various mechanisms. Unlike the original five-step model, which emphasizes a single dispersal event, this updated view recognizes multiple routes for cells to leave. Dispersal can be triggered by nutrient depletion, enzymatic degradation of the EPS, changes in local signalling (e.g., lowering of cyclic di-GMP), or host immune responses. Cells can exit as individual planktonic cells or as intact clumps of various sizes, each carrying the protective traits of the biofilm. These dispersed cells or aggregates can then seed new sites, forming fresh biofilms and repeating the cycle, as shown in Figure 2.20b.

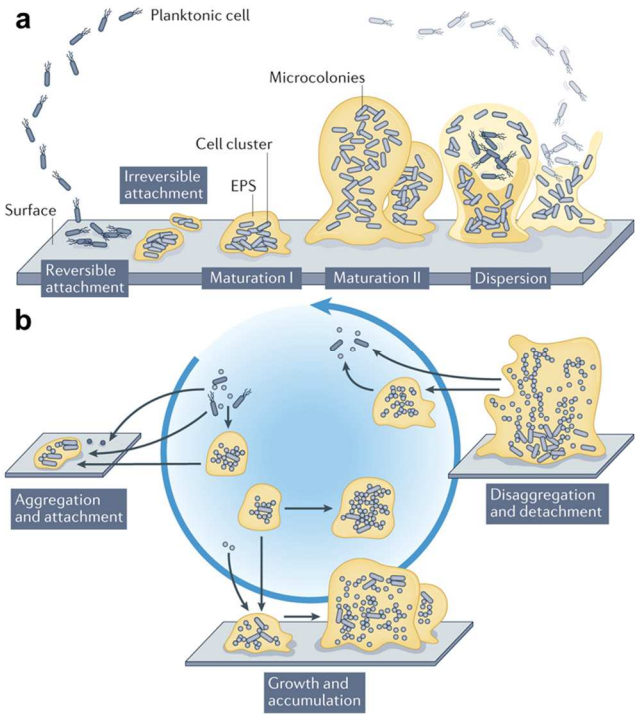

Figure 2.20. (a) The original five-step model of biofilm development and (b) expanded conceptual model of biofilm formation [98].

2.3.2 Artificial surface with water repellency and antibiofouling properties

As research into the water-repellent surface structures of nature deepens and interest in the healthcare industry grows, artificial biomimetic superhydrophobic and antibiofouling surfaces are attracting increasing attention. These surfaces can effectively prevent the adhesion of moisture and contaminants, while also inhibiting the growth and spread of bacteria by combining water-repellency and antibacterial functionality. Inspired by the surface structures found on taro and lotus leaves, Wang et al. fabricated hierarchically structured diamond films with two distinct features, a primary coating of micro-sized hemispheres and a secondary dense nanodiamond crystalline layer [99]. The synthesized structured surfaces exhibit superhydrophobic and self-cleaning properties even without surface modifications. The structured surfaces are capable of resisting 90–99% of bacterial adhesion. Additionally, the wear resistance is enhanced by a factor of 20 compared to that of exposed commercial substrates, such as titanium alloys, silicon, quartz glass and ceramics.

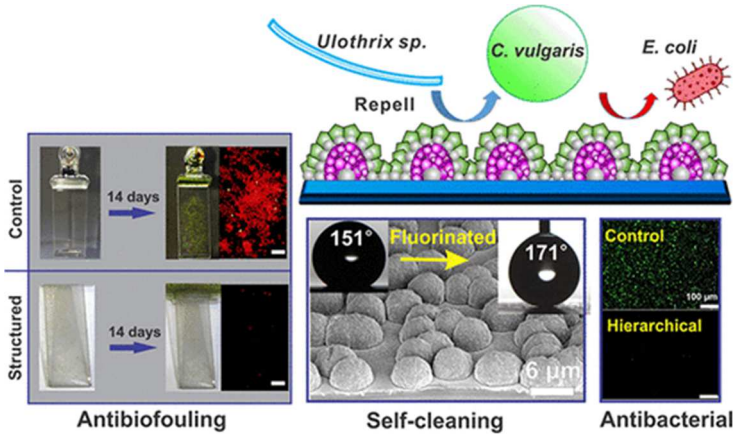

Figure 2.21. Robust biomimetic hierarchical diamond architecture with a self-cleaning, antibacterial, and antibiofouling surface [99].

Liu et al. fabricated a nanostructured surface by sintering silica nanoparticles onto an aluminium substrate [100]. Superhydrophobic surface with antibacterial properties is then fabricated by subsequently immobilizing the antimicrobial agent lysozyme within the nanostructure and modifying with fluorosilane. This engineered surface demonstrated effective resistance against the bacterial strains *S. Typhimurium LT2* (>99.99997% log-cycle reductions) and *L. innocua* (>99.99% log-cycle reductions) compared to the planar aluminium.

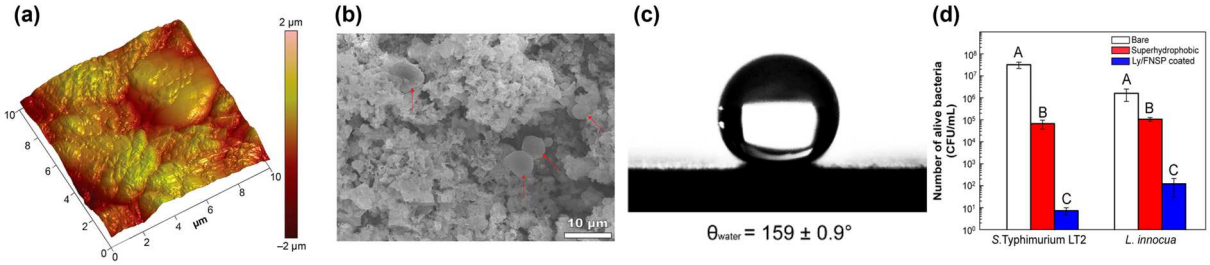

Figure 2.22. (a) AFM image, (b) SEM image, (c) water contact angle and (d) antibacterial behaviour of lysozyme and fluorinated silica nanoparticles coating surface [100].

Ozkan et al. employed a different approach with antimicrobial and antithrombotic properties by functionalizing medical grade silicone rubber (SR) with silica and silver nanoparticles and incorporating a nitric oxide (NO) donor. The fabricated surface (SH-SiAgNO) is designed to mitigate infection and thrombosis. [101]. The surface was made with fluorinated SiO_2 and Ag NPs via a dip-coating process and then immersed in the NO donor. This step allowed for the controlled release of NO, which acts as both an antimicrobial agent and a platelet inhibitor, reducing bacterial adhesion and preventing thrombosis. Surface characterization using SEM showed that the untreated

SR surface was smooth, while the SH-SiAgNO surface exhibited a hierarchical rough structure due to the incorporation of SiO_2 and Ag NPs as shown in Figure 2.23a. The treated SH-SiAgNO shows superhydrophobicity, as shown by the water contact angle of 154° as shown in Figure 2.23b, which minimizes liquid adhesion and enhances antifouling properties. The addition of Ag NPs and the synergistic release of NO are also important for the antimicrobial functionality of the surface. As can be seen from Figures 2.23c1 and c2, after 24 hours of exposure to *Escherichia coli* (*E. coli*, Gram-negative) and *Staphylococcus aureus* (*S. aureus*, Gram-positive), the number of colony forming units (CFU) of E. coli was reduced by >99.9% and the number of colony forming units (CFU) of S. aureus was reduced by >99.8% compared to the control untreated SR surface. At the same time, platelet adhesion was reduced by >96.1% compared to the untreated SR (Figure 2.21c3). Furthermore, as shown in the cytotoxicity test results in Figure 2.23c4, SH-SiAgNO does not impair cell viability.

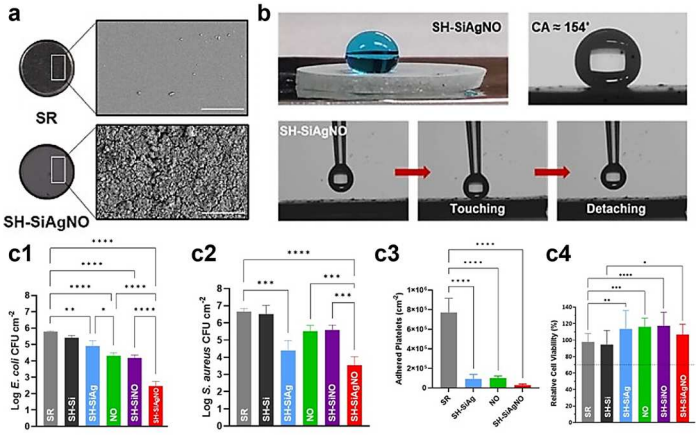

Figure 2.23. (a)SEM images of SR and SH-SiAgNO. (b) Wettability of SH-SiAgNO surfaces. Antibacterial tests against (c1) *E. coli* and (c2) *S. aureus*. (c3) Platelet density on different surfaces. (c4) Cytocompatibility of SH-SiAgNO surfaces [101].

2.4 State-of-the-art of ZnO water-repellent antibiofouling surfaces

2.4.1. Basic properties and synthesis of ZnO nanostructures

Zinc oxide (ZnO) is a widely utilized inorganic material, notable for its direct wide bandgap of 3.37 eV in the near-ultraviolet spectrum, which significantly influences its optical absorption characteristics [102]. ZnO nanostructures can be synthesized using a variety of chemical and physical methods, with precise control over reaction parameters enabling the fabrication of structures with specific morphologies and dimensions [103]. Commonly employed synthesis techniques include hydrothermal synthesis, chemical precipitation, electrochemical deposition, and chemical vapor deposition, each offering distinct advantages in terms of scalability, purity, and structural control. Hydrothermal synthesis is notable for its ability to produce well-defined nanostructures under controlled temperature and pressure conditions, utilizing aqueous solutions of zinc precursors. By tuning precursor type and concentration, PH, temperature, reaction time, and additives, researchers have achieved a broad range of ZnO nanostructures—from nanowires and nanorods to nanosheets and flower-like arrays [104-106]. Gerbreders et al. systematically investigated how reaction temperature, solution PH, precursor concentration, and different surface-active/capping agents govern the growth rates of distinct ZnO crystal faces, thereby making it possible to obtain nine different ZnO nanostructures under a unified synthesis protocol [104]. They showed that ZnO's polar facets exhibit anisotropic growth rates because these faces are more susceptible to directed adsorption or etching by OH^-

ions in solution. By applying multi-stage temperature settings or switching the pH during hydrothermal growth, researchers induced the formation of novel morphologies like flower-like or tubular ZnO structures. Moreover, introducing cationic polymers (such as polyethyleneimine, PEI) preferentially inhibits lateral growth while promoting axial extension—thus increasing the aspect ratio of ZnO nanorods or nanowires. Conversely, using citrate as an additive selectively binds to the (001) plane and blocks vertical growth, leading to sheet-like or stacked-layer ZnO.

Besides these direct influences on crystal growth, the condition and transformation of the ZnO seed layer itself also have a critical impact on nanowire (or nanorod) density, size, and orientation. In a recent study, Liu et al. explored how ammonia in an alkaline environment influences ZnO seed layers [105]. They reported that high concentrations of NH_3 not only promote the formation and exchange of $[Zn(OH)n]^{2-}$ complexes but also extensively etch and modify the seed layer during the early stages of hydrothermal growth, causing significant seed-layer dissolution followed by re-nucleation. Consequently, above a certain ammonia threshold, the number density of ZnO nanowires first increases and then decreases, with noticeable changes in their orientation. Thus, understanding and controlling these seed-layer dynamics is crucial for large-area, highly uniform, and orientation-specific growth of ZnO nanowire or nanorod arrays.

Hydrothermal temperature and duration also play decisive roles in morphological evolution. For instance, Mohan et al. produced ZnO materials under different

conditions and observed morphologies ranging from rod-like (1D) and flower-like (3D) structures to near-spherical (0D) shapes simply by altering temperature (100–150°C) and reaction time (1–5 hours) [106]. Their detailed characterizations (XRD, FTIR, TEM) uncovered correlations between grain size, structural defects, and surface functional groups, all of which influence how ZnO grows, dissolves, and re-precipitates to form unique nanostructures. Notably, higher temperatures generally led to smaller average grain size but also introduced additional processes (e.g., dissolution and secondary precipitation), which can give rise to hollow, branched, or otherwise highly complex architectures.

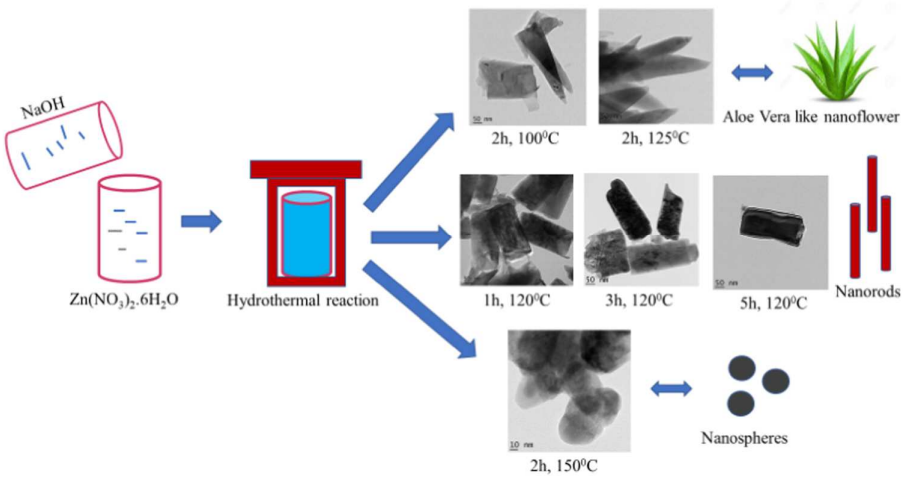

Figure 2.24. Hydrothermal synthesis of various nanostructures under different reaction parameters [106].

Chemical precipitation is also one of the most cost-effective and straightforward synthesis approaches for ZnO, wherein soluble zinc salts (e.g., zinc nitrate, zinc acetate) react with a base (NaOH, $NH_3 \cdot H_2O$, etc.) to form intermediate $Zn(OH)_2$ species that later convert to ZnO. Researchers often tune variables such as precursor

concentration, solution pH, temperature, and complexing agents to direct the final morphology. This route is especially attractive for large-scale production of ZnO nanoparticles, despite the challenge of controlling agglomeration and crystallinity without subsequent annealing. Akpomie et al. employed a facile one-pot chemical precipitation strategy to produce ZnO nanoparticles for removing bromophenol blue dye, simultaneously demonstrating antifungal efficacy against key filamentous fungi [107]. Such findings highlight how controlled precipitation conditions, particularly pH manipulation and stirring protocols, can yield stable and bioactive ZnO structures in a single synthetic step.

In contrast, electrochemical deposition affords precise control over ZnO film thickness and crystal orientation directly onto conductive substrates such as indium tin oxide (ITO) glass or metals. The technique typically involves a three-electrode cell where Zn^{2+} ions are reduced and incorporated into growing ZnO under carefully adjusted voltage/current conditions. By tuning ionic strength, additives (e.g., halides or organic ligands), and deposition temperature, one can target arrays of nanorods, nanosheets, or other anisotropic forms with strong substrate adhesion. Yang et al. demonstrated the successful electrodeposition of ZnO nanosheets on ITO, highlighting a layered, plate-like morphology and strong UV emission [108]. Xu et al. illustrated how selective adsorption of Cl^- or other anions can inhibit crystal growth along the c-axis, redirecting the ZnO nanostructure into platelets or rods depending on the relative binding energies of different facets [109]. These examples collectively underscore the

versatility of electrochemical routes, which can yield functionally tailored ZnO coatings especially suited to electronic, biosensing, or photocatalytic devices.

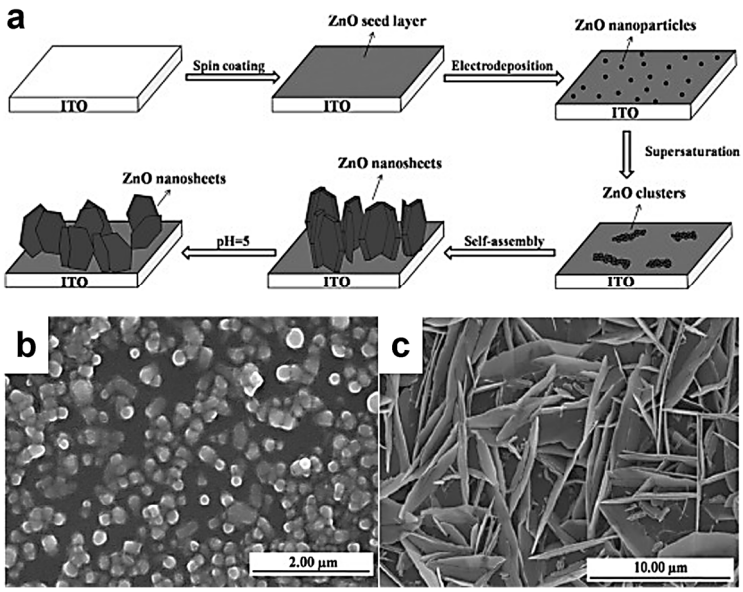

Figure 2.25. (a) Electrochemical deposition process. (b) SEM image of the seed layer. (c) The SEM image of ZnO nanosheets electrodeposited under conditions of: pH = 5.0, T = 80 °C, $[Zn^{2+}]$ = 0.1 M, 3.0 V [108].

Chemical vapor deposition (CVD) processes, including variations such as atmospheric-pressure CVD (APCVD), metal-organic CVD (MOCVD), and aerosol-assisted CVD (AACVD), can produce high-quality ZnO thin films—often doped for optoelectronic applications. In CVD, volatile Zn precursors (e.g., diethylzinc, zinc acetylacetonate) react with an oxidizing agent (water vapor, methanol, oxygen) at elevated temperatures on a heated substrate, forming uniform ZnO layers. Ponja et al. reported gallium-doped ZnO films via AACVD under oxygen-poor conditions, achieving resistivities as low as 7.8×10^{-4} Ω·cm alongside high optical transparency [110]. Such

doped TCO (transparent conducting oxide) films are critical in photovoltaics and display technologies.

Table 2.1 Comparison of different routes for ZnO nanostructures

Method	Advantages	Limitations
Hydrothermal Synthesis	1. Better crystallinity and more controlled ZnO morphology. 2. Well-suited for complex micro-/nanostructures (e.g. nanopillars, nanoflowers). 3. Can achieve high product purity and improved structural order.	1. Requires a high-pressure apparatus, increasing cost and safety concerns. 2. Morphology control may still be limited if temperature/pressure are not sufficiently high.
Chemical Precipitation	1. Simple process, minimal equipment requirements, suitable for large-scale production. 2. Mild reaction conditions (often near-ambient pressure or slightly elevated temperature). 3. Morphology can be partially tuned by pH, surfactants, etc.	1. Fine control over particle size distribution and morphology is challenging. 2. Post-annealing is often required to improve crystallinity. 3. Extra film-processing steps are needed for conductive films/devices.
Electrochemical Deposition	1. Allows direct ZnO film or oriented array growth on conductive substrates. 2. Flexibility in controlling film thickness and morphology (nanorods, nanosheets, flower-like arrays). 3. Operates at relatively low temperatures.	1. Requires specialized electrochemical equipment and conductive (or semiconducting) substrates. 2. Deposition on large areas or complex-shaped substrates can be restricted. 3. Strong sensitivity to solution composition and applied potential.
Chemical Vapor Deposition	1. Facilitates rapid formation of high-quality ZnO thin films on large-area or continuous production lines. 2. Highly suitable for precise doping (e.g., Ga, Al) to	1. Equipment and precursor costs can be high. 2. Often requires elevated temperatures.

	produce TCOs and other advanced electronic materials. 3. Good compatibility with various substrates and excellent uniformity.	3. Organometallic precursors can pose safety and environmental concerns. 4. Detailed parameter control (gas flow, temperature, deposition rate) is necessary.

2.4.2 Antibacterial mechanism of zinc oxide

Although the antibacterial activity of ZnO nanoparticles (ZnO-NPs) has garnered significant attention, the exact antibacterial mechanism is not yet fully understood. Nevertheless, existing studies have proposed several distinctive mechanisms, including the formation and release of reactive oxygen species (ROS) [111, 112], the release of antibacterial Zn^{2+} ions [113, 114] and the direct contact of ZnO-NPs with cells [115, 116], all of which can cause cellular damage and thereby achieve antibacterial effects.

The release of ROS is the most widely accepted mechanism for ZnO's antibacterial activity. ROS includes highly reactive ions and free radicals, such as superoxide anion (O_2^-), hydrogen peroxide (H_2O_2), and hydroxyl radicals (OH•), which damage cells by inducing oxidative stress responses [117]. When ZnO is exposed to UV light ($\lambda \leq$ ~370 nm), electron-hole pairs are generated in the conduction and valence bands due to its large exciton binding energy. While bulk ZnO mainly absorbs light in the near-UV range due to its intrinsic band gap (~3.37 eV), defect states, oxygen vacancies, or high specific surface area modifications can extend its photocatalytic activity to the visible light range by enabling sub-bandgap absorption and defect-mediated charge transfer [118, 119]. These pairs react with water to produce OH• and H^+, and the electrons react

with oxygen to generate intermediates such as O_2^-, H_2O_2, and OH• [120]. However, the mechanism of ROS generation is controversial. Some studies indicate that ROS production is dependent on light exposure, while others suggest that ROS can be generated even in dark conditions. Prasanna et al., through testing the effect of ZnO-NPs on *Staphylococcus aureus*, found that ZnO could generate ROS even in the dark, supporting the findings of Xu et al., which suggest that particle size and specific surface area of ZnO may lead to ROS release under dark conditions [121, 122]. This effect can be attributed to defect-induced ROS generation, where oxygen vacancies and surface defects in ZnO promote electron transfer reactions, leading to the formation of reactive oxygen species without external light activation [123]. Additionally, Padmavathy and Vijayaraghavan studied the bactericidal efficiency of ZnO-NPs of different sizes (12 nm, 45 nm, and 2 μm) and found that 12 nm ZnO-NPs exhibited the best efficiency, which attributed to their higher surface area leading to increased ROS release and consequently fatal damage to bacteria. This effect was observed under both UV and visible light conditions [124].

Another proposed antibacterial mechanism of ZnO-NPs is their release of zinc ions (Zn^{2+}), which disrupts the normal physiological functions of bacteria. The cytotoxic effects of Zn^{2+} are manifested through the inhibition of active transport, disruption of amino acid metabolism, and impairment of enzyme systems [125]. In addition to the direct interactions mentioned above, it can also further aggravate oxidative stress by producing ROS, thereby damaging bacterial cell membranes, proteins and nucleic

acids. Ahmed et al. employed an Allium cepa root-tip assay to systematically compare the effects of ZnO nanoparticles, bulk ZnO, and ionic Zn^{2+} on plant cells to give insights into Zn^{2+}-related mechanisms [126]. Their findings demonstrated that ZnO-NPs not only caused mitochondrial disruption and chromosomal abnormalities but also increased the generation of intracellular ROS, supporting the notion that released Zn^{2+} upon nanoparticle dissolution will actively perturbs cellular homeostasis. Although these experiments were conducted in a plant model, the elevated ROS generation, DNA damage, and enzyme inactivation underscore broad toxicological and antimicrobial effects, potentially extending to bacterial pathogens. In order to maintain the bactericidal properties of Zn^{2+} release while minimizing damage to host cells, Huang et al. presented a strategy to optimize Zn^{2+} release while mitigating its toxicity by synthesizing a Zn^{2+}–ε-poly(L-lysine)–protocatechuic aldehyde hybrid nanoparticle system (ZEP NPs) [127]. By incorporating Zn^{2+} into a self-assembled nanostructure, the researchers achieved local, on-demand ion release capable of destroying bacterial membranes within protein-rich environments. ZEP NPs exhibited potent bactericidal effects both in vitro and in vivo, while displaying minimal toxicity to host cells. Similarly, Wen et al. focused on harnessing Zn^{2+} release for the dual purpose of antibacterial activity and bone regeneration in a dental implant model [128]. They devised a mesoporous TiO_2 coating (MTC) on titanium substrates to confine ZnO nanoparticles, thereby generating a more controlled and sustained Zn^{2+} release profile. They demonstrated that a gradual ion release not only provided prolonged inhibition of key

oral pathogens but also improved the adhesion, proliferation, and osteogenic differentiation of bone marrow mesenchymal stem cells by capitalizing on the high surface area and ordered pore structure of TiO_2, shows that loading environment (in this case, a mesoporous coating) can mitigate bursts of Zn^{2+} and their potential cytotoxicity, while preserving potent antibacterial and osteogenic functions.

Moreover, it has been proposed that direct contact of ZnO NPs with bacterial cells may induce cellular damage, thereby contributing to their antibacterial properties. For example, Brayner et al. observed that *Escherichia coli* exposed to ultrafine ZnO-NPs exhibited gram-negative cell membrane disorder [129]. TEM images showed not only membrane damage of the bacteria cells, but also accumulation and internalization of ZnO-NPs within them. This direct interaction increased membrane permeability, thereby compromising cell integrity and disrupting its function. Similarly, Huang et al. showed that direct contact between ZnO-NPs and bacterial membranes led to membrane disorder in both gram-positive and gram-negative bacteria (*Staphylococcus aureus* and *Streptococcus agalactiae*) [130]. In addition, studies investigating the role of nanoparticle size and shape in mediating these interactions provide additional evidence that the direct contact of ZnO NPs and bacteria can achieve bactericidal effects. Zhang et al. demonstrated that smaller ZnO particles, with higher specific surface area, were more effective than larger particles in physically disrupting bacterial membranes, thereby enhancing antibacterial effects [131]. Furthermore, Matuła et al. reported that under dynamic conditions, collisions between ZnO nanostructures

(especially anisotropic forms such as nanorods) and bacterial cells generate significant nanomechanical stress [132]. This stress is able to pierce the cell wall, causing greater cell damage compared to spherical nanoparticles. Overall, in addition to the chemical toxicity associated with Zn^{2+} release, ZnO-NPs can improve their antibacterial efficacy by physical direct contact with bacterial cells through the combination of nanomechanical stress and membrane disruption.

2.4.3 Antibiofouling application of ZnO nanostructure-based water-repellent surfaces

Due to the inherent bactericidal properties of ZnO, various studies in recent years have explored the fabrication of water-repellent surfaces incorporating nanoscale ZnO to achieve both bactericidal and anti-adhesion against bacteria [133, 134]. This section provides a concise overview of the applications and recent progress of water repellent surfaces composed of various ZnO nanostructures in anti-biofouling tests.

Incorporating ZnO nanoparticles during surface preparation is a common way for fabricating such mentioned surfaces. Rahmah et al. employed a chemical precipitation method to produce a modified ZnO/PVC nanocomposite cluster surface with superhydrophobicity, achieving a contact angle of 160±2° [135]. Additionally, after modification with Ag and Fe_2O_3, the surface exhibited antibacterial properties against bacterial Klebsiella spp. and S. epidermidis, with the percentage of inhibition zone for both bacteria being approximately 25%. Gao et al. also used a chemical precipitation

method to dope cotton fabric with nanorod-shaped ZnO, preparing Ce-doped ZnO and Ag-deposited ZnO nanostructures with different Ce and Ag molar contents [136, 137]. The resulting ZnO NPs exhibited hydrophobicity with a contact angle of 103°. The optimal contact angle of 148° was achieved with 2.5% Ce doping, resulting in antibacterial rates of 83%, 85%, and 78% against *S. aureus*, *C. albicans*, and *E. coli*, respectively. For the Ag-doped ZnO, the maximum contact angle of 139° was obtained with 3% Ag doping, and the antibacterial efficacy against *S. aureus*, *E. coli*, and *C. albicans* reached 91%, 96%, and 98%, respectively. Furthermore, the Ag-doped ZnO demonstrated notable anti-mildew performance against *A. flavus*, highlighting its potential for broader antimicrobial applications, including the prevention of fungal contamination. In addition to doping ZnO NPs during the fabrication process, some studies have focused on creating ZnO-dominated nanoscale structured surfaces, such as nanotubes, nanopillars, and nanorods. These structures due to their enhanced surface area and high aspect ratio, can improve antibacterial and antifouling performance by altering surface wettability, facilitating photocatalytic activity, and promoting mechanical disruption of microbial membranes. Inspired by the disordered nanopillar structures on dragonfly wings, Tang et al. prepared ZnO/Au nanopillars using a combination of hydrothermal and photo-reduction methods. The photo-reduction process involves the reduction of metal precursors under light irradiation, which promotes the deposition of gold nanoparticles onto the ZnO nanostructure, which enhanced the photocatalytic and antibacterial properties. The surface modified

with PDMS exhibited superhydrophobicity with a water contact angle of 152°. The antibacterial and anti-adhesion rates against *E. coli* exceeded 99.99% after 24-hour of incubation, and even in the dark, the bactericidal rate remained at 65.5% [138].

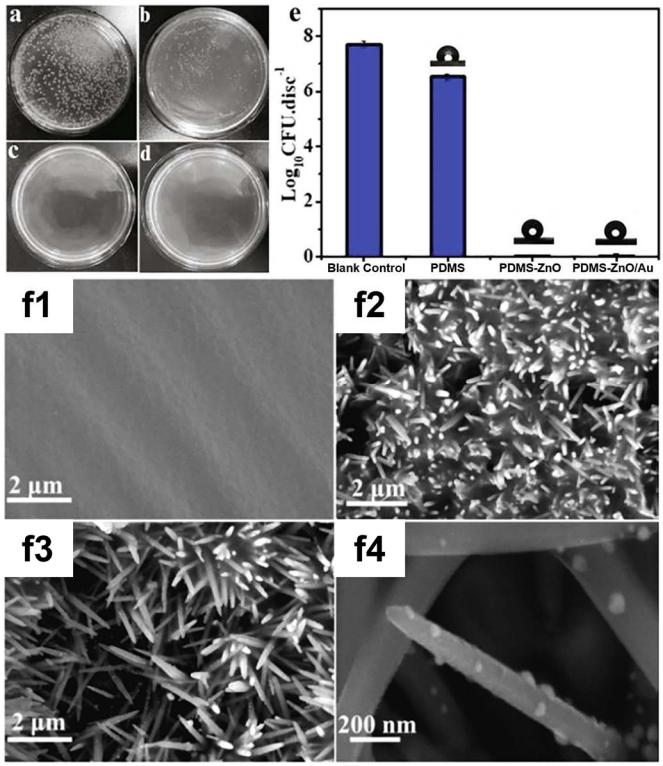

Figure 2.26. Colony formation assay for *E. coli* attached on modified surfaces during 24-hour incubation to assess antiadhesive activity: (a) blank control, (b) PDMS (c) PDMS-ZnO (d) PDMS-ZnO/Au, (e) the colony numbers for different samples. The insets in (e) show the water contact angles of respective samples. (f) SEM images of (f1) PDMS, (f2) PDMS-ZnO and (f3) PDMS-ZnO/Au. (f4) is an enlarged SEM image of PDMS-ZnO/Au [138].

Wang et al. employed an electrochemical deposition method to fabricate ZnO nanorods on Indium Tin Oxide (ITO) surfaces. After grafting PDMS via UV-induced modification, the surface exhibited superhydrophobicity with a contact angle of 158.1

± 3.7°. The grafting process involved spin coating a fresh PDMS solution onto the ZnO surface followed by UV irradiation to induce the formation of Zn–O–Si bonds. Unbound PDMS was then removed by sequential solvent washing with tetrahydrofuran and ethyl acetate to ensure stable and uniform modification. The number of *E. coli* on treated surface was significantly reduced under Field Emission Scanning Electron Microscope (FESEM, which utilizes a field emission electron source instead of the conventional thermionic electron gun used in regular SEM), as shown in Figure 2.27, which was reduced by 99.55% compared with the control group and 94.45% compared with the uncoated ZnO [139].

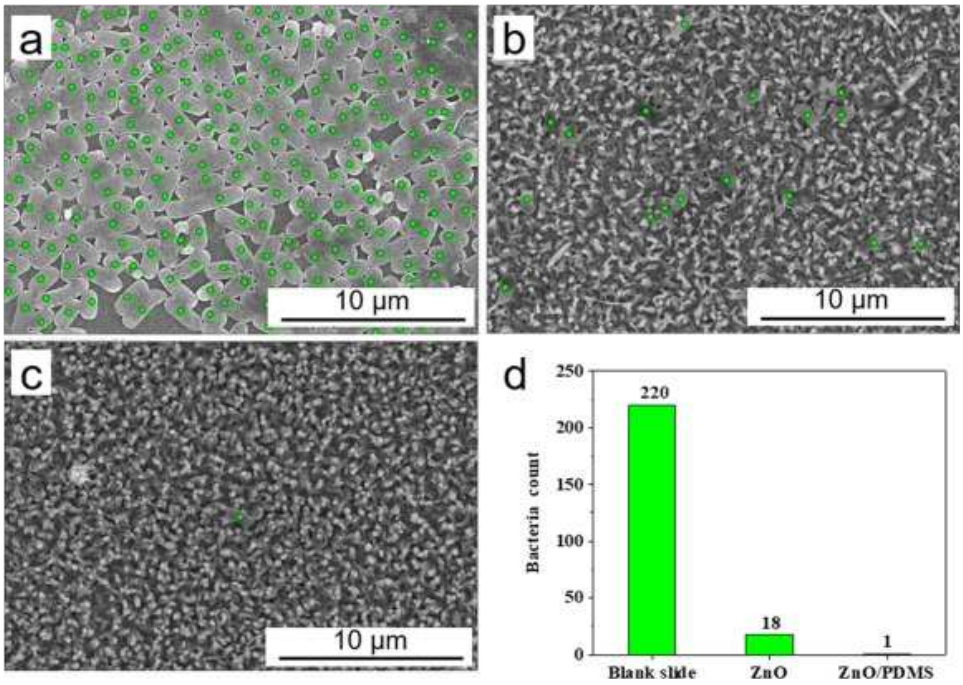

Figure 2.27. FESEM images of *Escherichia coli* on (a) blank slide, (b) ZnO, (c) ZnO/PDMS (d) histogram of bacterial counts. The green dots in the SEM images are visible *E. coli* on the surface [139].

Furthermore, Ozkan et al. conducted research inspired by the pitcher plant, fabricating SHS and LIS surfaces containing ZnO NPs and Cu NPs on medical-grade silicone rubber tubes (Saint-Gobain™ Tygon™ Formula 3350 silicone rubber (SR) tubing). These surfaces exhibited significant anti-adhesion activity against *E. coli*, reducing the adhesion rate lower from about 11 $\log_{10}$ CFU/cm^2 to 5 $\log_{10}$ CFU/cm^2 over 7 days compared to untreated silicone rubber tubes. [140].

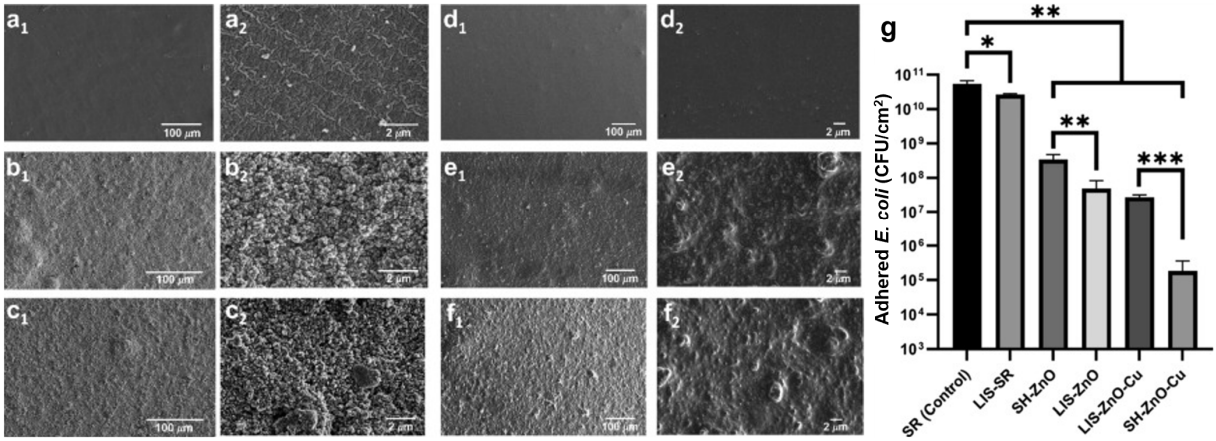

Figure 2.28. SEM images of the surface morphologies of (a1-a2) bare SR tube, (b1-b2) SH-ZnO, and (c1-c2) SH-ZnO-Cu at different magnifications. (d1-d2) LIS-SR, (e1-e2) LIS-ZnO, and (f1-f2) LIS-ZnO-Cu at different magnifications. (g) Graph demonstrating the reduction in adhered E. coli from the surface of various tubings after 7-day drip flow bioreactor study [140].

However, it is noteworthy that although ZnO nanomaterials demonstrate effective bactericidal properties, their potential cytotoxicity and associated risks to human health require thorough investigation and careful consideration. For instance, ZnO NPs have been shown to generate ROS, leading to oxidative stress, inflammation, and potential DNA damage in mammalian cells and may also cause pro-inflammatory responses

and apoptosis through ROS-mediated pathways. Additionally, ZnO dissolution in biological environments releases Zn^{2+} ions, which can disrupt cellular homeostasis and contribute to cytotoxic effects, particularly in pulmonary and epithelial cells [141, 142]. Therefore, although ZnO nanomaterials hold great promise for antimicrobial applications, their potential cytotoxic effects require careful risk assessment. Future research should focus on optimizing their physicochemical properties to balance antimicrobial efficacy and biocompatibility to ensure their safe application in biomedical and environmental fields.

2.5 Summary of knowledge gaps and research challenges

Based on the literature review, the following issues regarding the preparation of ZnO water-repellent surfaces for anti-biofouling applications will be investigated in this work.

1. Structure design and biocompatibility

Designing and fabricating suitable nanostructures is essential for subsequent water-repellent treatment of ZnO samples and for maintaining their inherent bactericidal properties. Specifically, the ideal morphology is to fabricate a biomimetic nanopillar array similar to the surface of a cicada wing, thereby achieving a composite bactericidal effect of nanopillar mechanics and zinc oxide photocatalysis. Additionally, it is important to ensure that the fabricated samples are non-cytotoxic to mammalian cells since ZnO nanomaterials may release Zn^{2+} ions or generate ROS during photocatalysis, which may affect cell viability. Cytotoxicity testing can ensure that the

fabricated surfaces are safe and stable in the application environment, thereby improving its practical feasibility and application potential.

2. Durability and longevity

Most existing antibiofouling materials suffer from performance degradation over extended use, making long-term efficacy a significant challenge. Ensuring the stability and functionality of these materials over weeks to months of application remains a major challenge. Furthermore, developing materials that can self-regenerate or repair during use would significantly enhance the durability and lifespan of antifouling materials.

3. Mechanism of action research

Although various ZnO antibiofouling surfaces have been developed, there is still a lack of in-depth understanding of their specific mechanisms of action. This limits the ability to optimize the ZnO nanostructure-based surfaces to enhance their multifunctionality. Further research is needed to explain the mechanism by which ZnO-based materials affect bacteria and achieve their bactericidal efficacy.

CHAPTER 3 FABRICATION AND OPTIMIZATION OF BIOINSPIED ZINC OXIDE NANOPILLARS

3.1 Introduction

Building on the literature review in Chapter 2, this chapter fabricates cicada-wing-inspired biomimetic ZnO nanopillar structures by using hydrothermal synthesis and systematically optimises their morphology to obtain uniform, highly controllable arrays. The wing pillars in nature measure about 65–95 nm in diameter and 380–510 nm in height, providing the benchmark for the synthetic design. The growth of ZnO nanostructures is strongly influenced by reaction mechanisms and synthesis parameters, often leading to uneven morphology, agglomeration and random orientation. Accordingly, the central aim here is to refine pillar alignment and size distribution to produce a stable, repeatable cicada-wing-like surface. ZnO nanopillars are first grown directly on zinc substrates, and the influence of key growth variables is examined. During optimisation, parameters such as substrate orientation and reaction time are tuned to improve array uniformity while suppressing irregular growth and agglomeration. Finally, the morphology, size distribution and crystal structure of the optimised pillars are characterised by SEM, AFM and XRD, confirming that the desired bio-inspired architecture has been faithfully reproduced.

3.2 Methodology

3.2.1 Materials

Materials used for the fabrication of ZnO nanopillars include pure zinc foils (Fisher

Scientific UK, 99.9%, 0.62 mm in thickness) as the substrate, and sodium hydroxide pellets (*NaOH*) and zinc nitrate hexahydrate crystals ($Zn(NO_3)_2 \cdot 6H^2O$) as the reactants. Other reagents used in subsequent experiments will be introduced in the relevant methodology sections. Unless otherwise specified, all reagents were obtained from Sigma-Aldrich (UK).

3.2.2 Fabrication of ZnO nanopillars

The zinc foils were cut into small substrates with the dimensions of 1 cm × 1 cm. Since zinc foils are highly susceptible to oxidation, they were polished using 2000-grit sandpaper for surface cleaning, ensuring the removal of organic residues and natural oxide layers, followed by thorough rinsing with DI water. The substrates were then ultrasonically cleaned using a Shesto Ultrasonic Cleaner at 25°C, sequentially in ethanol, acetone, and deionized (DI) water, for 5 minutes in each medium and dried with nitrogen (N_2) flow before use.

Briefly, ZnO nanopillars were prepared by immersing bare zinc substrates into an alkaline zincate solution, which was formed by mixing 35 mL of 0.43 mol/L $Zn(NO_3)_2 \cdot 6H_2O$ with 35 mL of 3.43 mol/L NaOH. The solution was then heated and stirred using an MS-H280-Pro stirring hot plate at 100 °C, with the beaker sealed, and maintained for 45 minutes. The samples were removed from the solution after fabrication and dried using N_2 flow after rinsing with DI water. Here, $Zn(NO_3)_2 \cdot 6H_2O$ serves as the precursor material that provides the zinc (Zn^{2+}) ions and NaOH provides hydroxide ions (OH^-). During the hydrothermal reaction, the Zn^{2+} ions dissolve into the

solution and react with hydroxide ions (OH^-) to form $Zn(OH)_2$, which further transforms into ZnO. The key reaction steps are as follows:

$$Zn(NO_3)_2 + 2H_2O \rightarrow Zn(OH)_2 + 2HNO_3$$

$$Zn^{2+} + 2OH^- \rightarrow Zn(OH)_2$$

$$Zn^{2+} + 4OH^- \rightarrow Zn(OH)_4^{2-}$$

$$Zn(OH)_2 \rightarrow ZnO \downarrow + H_2O$$

$$Zn(OH)_4^{2-} \rightarrow ZnO \downarrow + H_2O + 2OH^-$$

These formulas illustrate the precipitation mechanism of ZnO, where $Zn(OH)_2$ and $Zn(OH)_4^{2-}$ act as intermediates before ZnO formation. The dissolution of zinc atoms into the solution leads to an increase in the concentration gradient of zinc ions near the bare zinc substrate, and the presence of hydroxide shifts the equilibrium toward the formation of $Zn(OH)_4^{2-}$, which subsequently decomposes to ZnO and ultimately resulting in the formation of ZnO nanopillars.

3.2.3 Characterisation of ZnO nanopillars

Surface morphology was observed using SEM and AFM. SEM images were taken using Zeiss EVO 10 Materials SEM at an acceleration voltage of 15.0 kV. The AFM (Cypher S AFM from Oxford Instruments) images were taken using the air tapping mode to minimize sample damage and artifacts while providing high-resolution imaging of the ZnO nanostructures, with a scan size of 3 × 3 or 1 × 1 μm^2 and a scan rate of 1.0 Hz to capture detailed surface morphology and obtain high-quality image results while maintaining fast imaging efficiency.

X-ray diffraction (XRD) was employed to identify and characterize the crystal structure of the ZnO nanopillars, confirming phase purity and crystallographic orientation. Data were collected using a Proto AXRD Benchtop diffractometer (Proto, USA) operated at 30 kV and 20 mA with a Cu Kα source (λ = 1.54251 Å). The samples were analyzed over the 2θ range of 20–80° using 0.0149° increments.

3.3 Results and Discussions

Figure 3.1 presents a representative high-magnification SEM micrograph of the ZnO nanopillars produced under the initial, unoptimized hydrothermal conditions (100 °C, 45 min). Two markedly different morphologies are evident within the same field of view. First, compact domains of vertically aligned nanopillars grow normal to the Zn substrate. Second, isolated “explosive” clusters of randomly oriented nanorods erupt from regions where pillar nucleation was clearly hindered. Image-analysis statistics collected over ten independent areas (about 50 μm² each) show that approximate 60% of the substrate is covered by the desired vertical pillars, whereas rest is occupied by the disordered rods. This abnormal growth phenomenon may be closely related to the uneven deposition and dissolution of $Zn(OH)_2$ during the synthesis process. When the NaOH concentration is high or the local pH value is high, $Zn(OH)_2$ is easily deposited on the substrate surface as a white solid covering layer, thereby affecting the normal oriented growth of nanopillars. On the one hand, the deposited layer may hinder the uniform nucleation of some areas, causing the growth of ZnO to show different rates in different areas. On the other hand, the slow dissolution

of $Zn(OH)_2$ may lead to the random nucleation and lateral growth of ZnO, causing some nanocolumns to extend along the other directions instead of the preferred growth direction of vertical, thereby forming a disordered irregular structure. In addition, the uneven deposition of $Zn(OH)_2$ may also cause changes in the diffusion rates of local Zn^{2+} and OH^- ions, causing competitive growth of ZnO nanostructures in certain areas, further exacerbating the phenomenon of morphology loss of control.

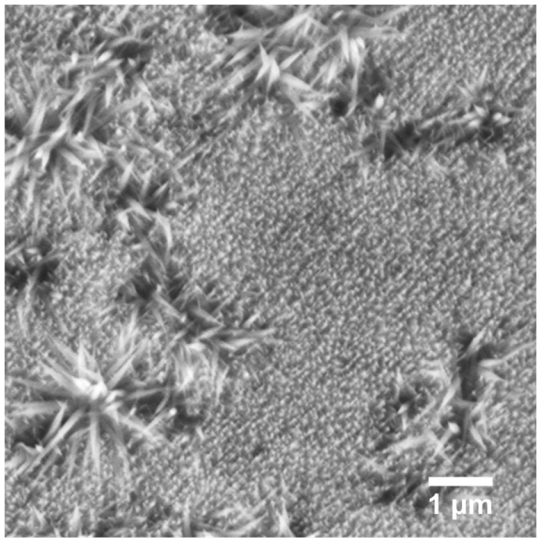

Figure 3.1. SEM image of fabricated ZnO nanopillars before optimization.

In view of the above situation, the placement of the zinc substrate involved in the reaction was geometrically optimized. a second Zn foil (1 cm × 3 cm × 0.62 mm) was bent into a right-angle bridge and placed horizontally at the bottom of the reaction beaker with a gap left, and the substrate to be prepared into the sample was placed horizontally on the bridge-shaped bracket so that both its up and downward-facing side were exposed to the precursor solution. This seemingly minor change has two decisive consequences. First, orienting the growth substrate so that its downward-facing surface contacts the solution prevents deposition of the white $Zn(OH)_2$ precipitate,

thereby reduced the negative impact to the surface morphology. Second, gravity aids the axial growth of the nanostructures, promoting a more nearly perpendicular (z-axis) alignment of the nanopillars. The efficacy of the optimisation is evident in Figure 3.2, where explosive nanorods have virtually disappeared, and the pillar coverage rises to 99%.

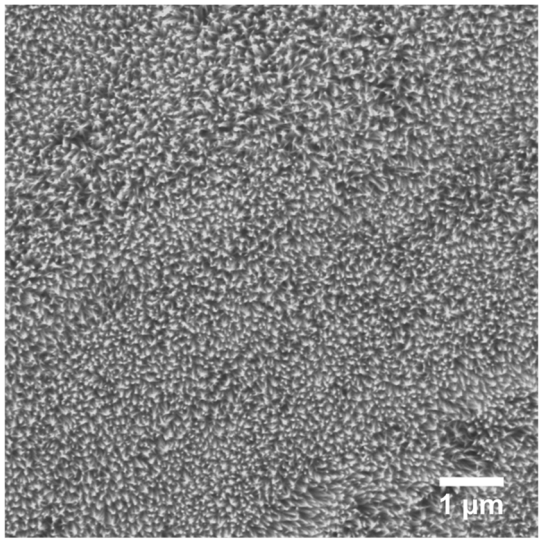

Figure 3.2. SEM image of fabricated ZnO nanopillars after optimization.

Building on the comparisons presented in Figures 3.1 and 3.2, which illustrate the morphology in small observation areas for the unoptimized and optimized samples, SEM images were further acquired over a larger area (Figure 3.3) to verify these trends and ensure the accuracy of the results. The unoptimized ZnO sample (Figure 3.3a) exhibits relatively large and unevenly distributed particles, with pronounced agglomeration and a rougher surface. In contrast, the trend of growth of ZnO nanopillars become more uniformly distributed and exhibit reduced agglomeration after the optimization (Figure 3.3b). The overall surface appears smoother and almost no crystal agglomeration is observed, indicating that the improved hydrothermal

conditions effectively control the nucleation and growth of crystals, thereby obtaining a more homogeneous ZnO nanopillar array.

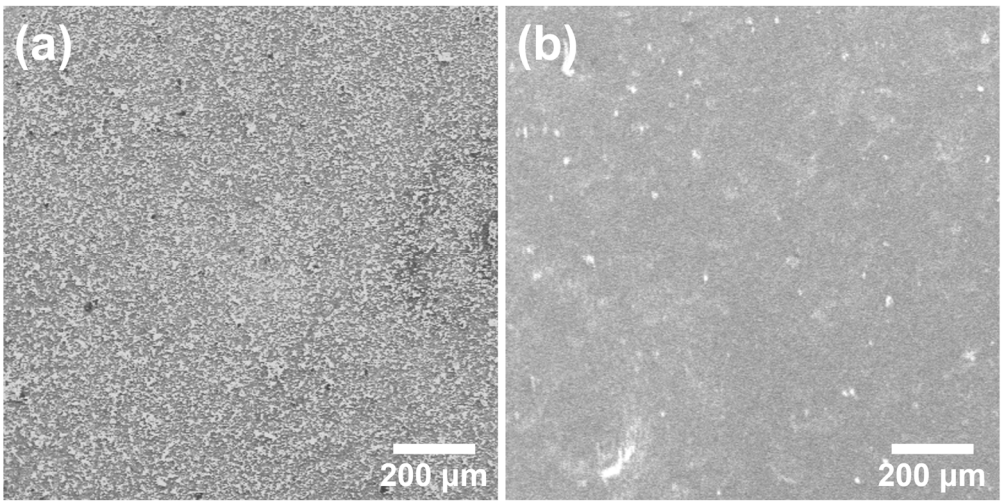

Figure 3.3. SEM image of fabricated ZnO nanopillars (a) before and (b) after optimization in a large observation area.

Figure 3.4 shows the XRD pattern of optimized hydrothermally grown ZnO nanopillars. The prominent diffraction peaks are located at 2θ ≈ 31.8°, 34.4°, 47.5°, 56.6°, 62.9°, and 68.0°, which can be assigned to the (100), (002), (102), and (103) planes of the hexagonal wurtzite ZnO phase (JCPDS No. 36-1451). Among these peaks, the (002) reflection intensity at 2θ ≈ 34.4° is the highest, indicating a strong preferred orientation along the z-axis. This pronounced (002) peak is characteristic of solution-grown ZnO nanostructures, indicating that crystal growth occurs primarily in the direction perpendicular to the substrate surface. In addition to the ZnO peak, weak reflections attributed to the underlying Zn substrate were observed at lower 2θ angles (e.g., around 43.3° and 70.0°). The sharpness of the ZnO peak and the absence of

detectable impurity peaks indicate that the as-prepared ZnO has well crystallinity and phase purity.

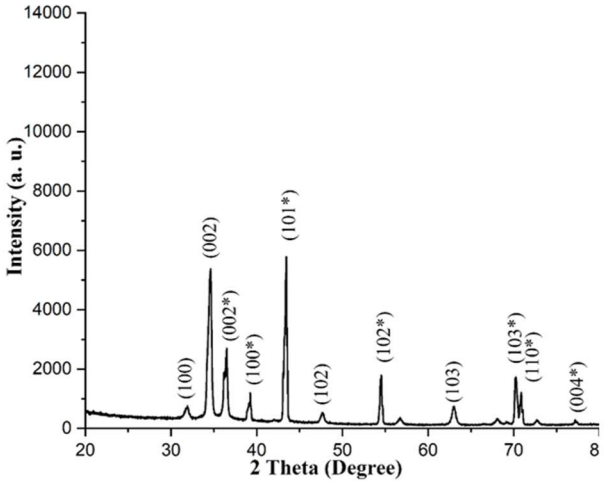

Figure 3.4. XRD results of optimized ZnO nanopillars.

To fine-tune the planar alignment of the ZnO nanopillar arrays after optimization, the hydrothermal reaction time was systematically adjusted while keeping all other parameters (temperature, precursor concentration, and pH) constant. From the AFM images presented in Figure 3.5, a clear evolution in the morphology of ZnO nanopillars is observed as a function of reaction time. The nanopillars are relatively short and exhibit a less uniform distribution at shorter reaction times (15 and 30 minutes), indicating that nucleation and early-stage growth dominate the process. By extending the reaction time to 45 minutes, the nanopillars attain an optimal balance between height and density, resulting in a well-aligned and homogeneous array that closely mimics the natural cicada-wing topography. This intermediate reaction time appears to provide sufficient time for crystal growth and structural regularization without promoting excessive coalescence or aggregation. In contrast, a further increase in reaction time

to 60 minutes results in pronounced pillar growth, which, although beneficial in enhancing dimensional parameters, also introduces crowding and partial agglomeration that could compromise the uniformity of the array. Therefore, the 45-minute sample represents the optimal condition for fabricating a biomimetic cicada-wing surface, as it achieves a desirable trade-off between dimensional control and structural integrity and was used in subsequent studies.

It worth noting, however, that the AFM tip itself can introduce measurement artifacts, especially in the lateral (diameter) dimension. The size of standard commercial AFM probe tips typically ranges from a few nanometres to several micrometres, which can cause the measured diameter to be larger than the actual value. Therefore, while the height range can be determined, additional morphological measurements (such as SEM) are needed to validate the diameter of the fabricated nanostructures.

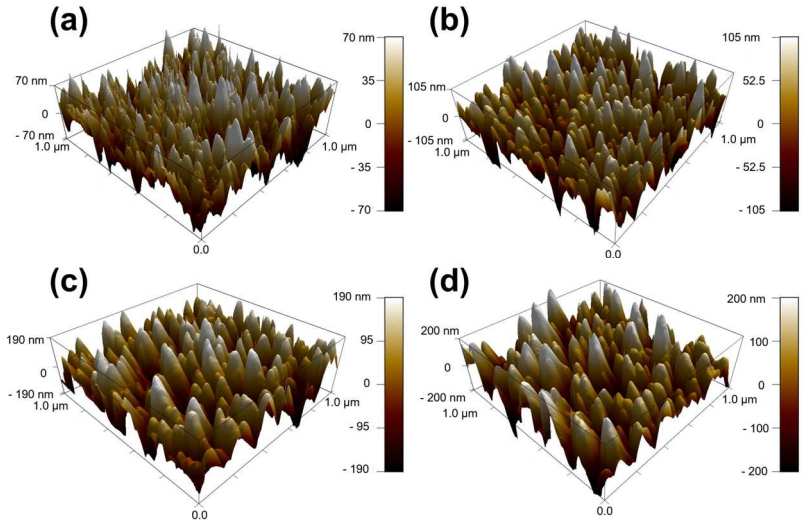

Figure 3.5. AFM images of fabricated ZnO nanopillars with reaction time of (a) 15 min, (b) 30 min, (c) 45 min and (d) 60 min.

3.4 Conclusion

The work in this chapter successfully prepared and optimized the ZnO nanopillar array, which simulated the nanopillar structure of cicada wings in morphology. By adjusting the substrate placement method, the influence of the $Zn(OH)_2$ deposition layer on the growth uniformity was effectively reduced, and by optimizing the hydrothermal synthesis time, a highly controllable ZnO nanopillar array was successfully obtained. Under the optimal reaction conditions of 45 minutes, the obtained ZnO nanopillars showed uniform size distribution and good arrangement direction and showed excellent crystal quality and surface uniformity. The experimental results show that the morphology of ZnO nanopillars significantly affects their surface functions. Shorter hydrothermal reaction time (15–30 min) resulted in lower nanopillar height, uneven distribution, and lack of bionic features of cicada wings; while extending the reaction time to 60 minutes can obtain higher nanopillars, but it will also cause agglomeration and destroy the uniformity of the structure. Therefore, the 45-minute reaction condition achieved the best balance between morphology, size and arrangement uniformity, so that the ZnO nanopillar array successfully reproduced the biomimetic characteristics of cicada wings.

CHAPTER 4 WETTABILITY AND BACTERICIDAL PROPERTIES OF BIOINSPIRED SUPERHYDROPHOBIC SURFACES

4.1 Introduction

This chapter builds on the preparation and characterization of zinc oxide (ZnO) nanopillars described in Chapter 3 and investigates how these nanostructures can be used to create surfaces that have both self-cleaning properties and bactericidal activity. In recent years, superhydrophobic surfaces have attracted much attention due to their low surface energy, which effectively inhibits the spread of water droplets, thereby reducing the adhesion of dirt and microorganisms. However, in complex biological environments, superhydrophobicity alone is often not enough to completely inhibit bacteria. To address this limitation, we coated the prepared ZnO nanopillars with a layer of polydimethylsiloxane (PDMS) to achieve superhydrophobicity of the sample. At the same time, by keeping the PDMS coating thin, the morphology of the ZnO nanopillars remains visible, thereby retaining the inherent photocatalytic activity of ZnO under visible light irradiation and the generation of reactive oxygen species (ROS). These ROS damage the bacterial cell wall and other intracellular components, ultimately leading to cell death. A synergistic effect between "passive anti-adhesion" and "active bactericidal action" is achieved.

In this chapter, the wettability of the fabricated PDMS/ZnO nanostructures was first characterized, including measuring water contact and sliding angles, and performed droplet impact experiments to confirm the stability of the coatings. Microscopic and

elemental analyses such as X-ray diffraction (XRD) and Fourier transform infrared spectroscopy (FTIR) were then performed to confirm the presence and distribution of the coatings, and photocatalytic experiments were performed to confirm their photocatalytic activity under visible light. Next, the bactericidal and anti-adhesion properties of these surfaces were evaluated using *Staphylococcus aureus* (*S. aureus*, Gram-positive bacteria) and *Escherichia coli* (*E. coli*, Gram-negative bacteria). The overall antimicrobial biofouling efficacy of the superhydrophobic surfaces was quantified by comparing bacterial growth and coverage at different incubation periods (18 and 72 hours).

The results presented in this chapter validate the feasibility of combining thin PDMS-based superhydrophobicity with ZnO-mediated photocatalysis to improve antimicrobial performance. In addition to demonstrating the direct effectiveness of this "dual-action" approach, the results also provide insights into the effects of different coating thicknesses and exposure to multiple cycles incubation on the bactericidal efficacy, as well as the biocompatibility of the fabricated surfaces. These observations lay the foundation for subsequent chapters where we will explore other surface treatment and modification routes to expand the range of antifouling strategies for ZnO-based nanostructures.

4.2 Methodology

4.2.1 Materials

The materials (pure zinc foils) and reagents (sodium hydroxide, zinc nitrate

hexahydrate, ethanol, acetone, and deionized (DI) water) used for the pre-treatment and preparation of ZnO nanopillars have already been discussed in Chapter 3.2.1. PDMS, SYLGARD 184 Silicone elastomer curing agent, and ethyl acetate were utilized for coating the ZnO nanopillars. *S. aureus* and *E. coli* were employed in the bactericidal efficacy testing. The LIVE/DEAD BacLight bacterial viability kit was obtained from Fisher Scientific (UK). Other reagents used in subsequent experiments will be introduced in the relevant methodology sections. Unless otherwise specified, all reagents were obtained from Sigma-Aldrich (UK).

4.2.2 Modification of ZnO Nanopillars

The samples used in this chapter are superhydrophobic surfaces based on ZnO nanopillars (Chapter 3). The fabricate nanopillar surfaces were coated with a thin layer of PDMS to modify their wettability. Typically, the PDMS solution was prepared by mixing 1 mL of PDMS polymeric base, 0.1 mL of silicone elastomer curing agent, and 100 mL of ethyl acetate, followed by stirring at 250–280 rpm in a beaker using an MS-H280-Pro stirring hot plate at room temperature. The 10:1 ratio of PDMS, as recommended by the manufacturer, provides a balance between flexibility and mechanical strength, ensuring the polymer fully cures without becoming excessively brittle or remaining too soft. The well-stirred solution was then drop-cast using an Eppendorf Research Plus micropipette onto the ZnO nanopillar surfaces (5 μL per sample) to form a thin coating and subsequently cured in an Genlab MINO oven at 80 °C for 6 hours. For comparison, thicker PDMS coating samples were also prepared

by drop-casting 25 μL (instead of 5 μL) onto the ZnO nanopillar surfaces and curing under the same conditions. Additionally, comparative samples of pure PDMS were prepared using the same 10:1 ratio by directly mixing the PDMS base and silicone elastomer curing agent in a glass Petri dish, followed by curing in an oven with same time.

4.2.3 Characterization of ZnO Nanopillars

Surface morphology was observed using SEM and AFM. SEM images were taken using Zeiss EVO 10 Materials SEM initially, and subsequently with a Thermo Scientific Apreo 2S SEM after an equipment upgrade, at an acceleration voltage of 5.0–15.0 kV. Using different voltages for different sample types can yield clearer images. For example, low kV should be used when observing PDMS-coated samples, which have high surface sensitivity. PDMS-coated samples were coated with 8 nm of Au by sputter deposition before analysis. Bare zinc and ZnO nanopillar samples offered good conductivity but were also coated with gold layers to ensure consistency of the observation parameters. The AFM (Cypher S AFM from Oxford Instruments) images were taken using the air tapping mode to minimize sample damage and artifacts while providing high-resolution imaging of the ZnO nanostructures, with a scan size of 3 × 3 or 1 × 1 μm^2 and a scan rate of 1.0 Hz to capture detailed surface morphology and obtain high-quality image results while maintaining fast imaging efficiency.

The wettability of the samples was evaluated by measuring the static contact angle of 12 μL DI water droplets, dispensed by Hamilton 1750 RNR 500μL syringe which on

a DataPhysics OCA15EC goniometer. The static contact angle was determined utilizing Young-Laplace fitting in the goniometer software and measurements were performed at three randomly selected positions on each surface. To measure sliding angles, the samples to be measured were placed on a slope-adjustable sample stage. A drop of deionized water (12 μL) was deposited on the sample using goniometer. The tilt angle was then gradually adjusted using the stage's knob until the water droplet slid off the sample. The entire process (images and videos) was recorded by the 6.5-fold zoom lens of the goniometer itself, and the sliding angle was manually measured from the recorded images using FIJI (ImageJ 1.54f) software to verify the results obtained from the sample stage. To measure contact angle hysteresis, the needle-in method was employed. A drop of water was deposited onto the sample using the goniometer's needle, with the needle remaining within the droplet. The volume of the droplet was then increased or decreased at a dosing rate of 1 μL/s each time, and the advancing and receding angles were recorded in real-time by the goniometer's automatic droplet profile capturing function. After obtaining all the results, the contact angle hysteresis of the surface was calculated by determining the difference between the advancing contact angle and the receding contact angle. In addition, droplet impact experiments were carried out on the fabricated superhydrophobic surface to evaluate its actual water-repellent performance and structural stability under dynamic environments. The experimental set-up used in droplet impact testing is shown in Figure 4.1. Water droplet impact behaviours were captured using a high-speed camera (FASTCAM Mini UX100,

Photron) at a frame rate of 1000 fps.

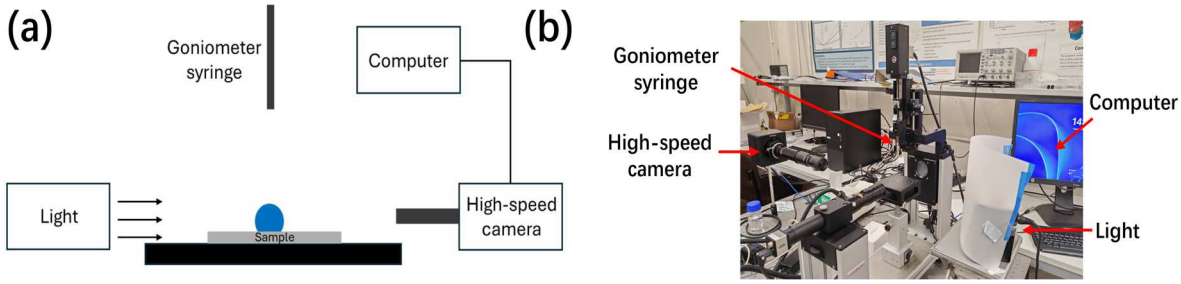

Figure 4.1. (a) Schematic illustration and (b) real set-up of the droplet impact measurement.

XRD was employed to identify and characterize the crystal structure of the ZnO-based samples, confirming phase purity and crystallographic orientation. Data were collected using a Proto AXRD Benchtop diffractometer (Proto, USA) operated at 30 kV and 20 mA with a Cu Kα source (λ = 1.54251 Å). The samples were analyzed over the 2θ range of 20–80° using 0.0149° increments.

FTIR spectroscopy was employed to identify and analyze the characteristic functional groups and chemical bonds present in the samples. The FTIR spectra were collected on a Nicolet iS50 FTIR spectrometer. All spectra were recorded in the range of 4000 to 400 cm^{-1}, with a spectral resolution of 4 cm^{-1} in both absorbance and reflectance mode with the ATR module. Measurements were taken with 256 coadded scans.

Photocatalytic performance was measured using a BMG Labtech CLARIOstar Plus plate reader in fluorescence intensity mode to quantify the degradation rate of fluorescent dye CF633. An excitation wavelength of 625 ± 10 nm and an emission

wavelength of 650 ± 20 nm were set for the fluorescence intensity mode. The CF633 dye was prepared in aqueous solutions (0.01 mg·mL^{-1}) before use. One drop of thirty microliters of 0.01 mg/mL fluorescent dye was placed on different surfaces using pipette. Degradation was monitored indoors under ordinary lighting conditions with a light intensity of 400 lux, and the distance between the light source and the sample was 2.5 m. The experiment was repeated three times under the same lighting condition, with readings taken every 1 hour.

4.2.4 Antibiofouling testing and analysis methods

4.2.4.1 Bacterial culture preparation

Both *E. coli* and *S. aureus* were cultured in 5 mL of Lysogeny broth (LB) overnight at 37 °C for ≈ 18 h with shaking at 180 rpm. The culture was then adjusted to ≈ 1 × 109 (colony-forming units) CFU mL^{-1}.

4.2.4.2 Agar plates preparation

LB Agar was prepared following the manufacturer's instructions and autoclaved for sterility. After removal from the autoclave, a brief cooling period of approximately 5 minutes was allowed, followed by gentle shaking to ensure homogeneity. The agar was then poured into plates near a Bunsen flame, ensuring coverage of the bottom of the plate with agar. A minimum of 12 plates (with three plates for each type of sample, including control, bare zinc, ZnO nanopillars, and PDMS-coated nanopillars) were prepared for the experiment. Each agar plate was sectioned into eight segments labelled from A to H, as shown in Figure 4.2(a).

4.2.4.3 Anti-biofouling test

All sample surfaces were incubated with cultured bacterial solutions for 18 hours and 72 hours. The surfaces were inoculated with the bacterial suspensions in a 3×3 grid of 1-μL aliquots of bacterial culture across the sample surfaces, as shown in Figure 4.2(b). The PDMS-coated ZnO nanopillar surfaces were an exception because of their superhydrophobicity, which allowed small droplets to roll off easily. Instead, a single 9-μL droplet was carefully pipetted onto the surface of PDMS-coated ZnO nanopillars. After the incubation, the samples were transferred into 15-mL centrifuge tubes containing 10 mL of Dey-Engley Neutralising Broth, each accompanied with 7-10 sterile zirconium beads. Subsequently, the tubes were vortex-mixed for 1 minute. Serial dilution of 1:3 (eight times) in sterile phosphate-buffered saline (PBS) within a 96-well plate was then carried out using the neutralising broth suspension. This dilution approach ensured a controlled and gradual reduction in bacterial concentration for accurate analysis. Each row of broth corresponded to the previously sectioned agar plate. Subsequently, three 10-μL droplets from each row of the PBS solutions that had been serially diluted in the 96-well plate were spotted into their designated sections on the LB agar plates, as shown in Figure 4.2(c). Three sets of repeats for each surface were prepared. The plates were then allowed to dry thoroughly around a Bunsen burner. Once all plates had dried, they were placed in a static incubator at 37 °C for 16-18 hours. The plates were removed from the incubator the following day, and the survival of the bacteria was assessed by counting CFU, where colony numbers were

multiplied by the relevant dilution factor [143]. The limit of detection for the assay was set to 1×10^3 CFU.

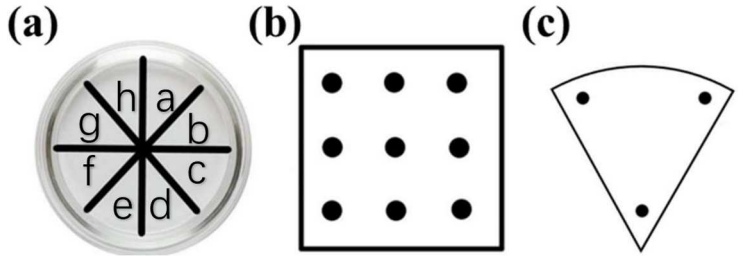

Figure 4.2. Schematic diagram of agar plates preparation and anti-biofouling efficacy testing: (a) Agar plate with divided areas. (b) Bacterial culture spots on surface. (c) bacterial drops on an individual section of the agar plate.

4.2.4.4 Microscope observation

Samples for confocal microscopy (Leica TCS SP8 confocal microscope with 40×/1.40 oil objective) were prepared using the incubated surfaces from the anti-biofouling test. Each sample was gently washed with 30 µL of PBS to ensure the removal of any residual medium. A staining solution was prepared by mixing the PBS with dyes from the LIVE/DEAD™ BacLight™ bacterial viability kit. Then 5 µL of the staining solution was pipetted onto the samples, followed by 15 minutes of storage in the dark. Cells that were dead or dying on the samples because of a compromised membrane stained red, whereas cells with an intact membrane appeared green, as schematically illustrated in Figure 4.3. The parameters for the excitation were set to a wavelength of 488 nm and 561 nm based on the characteristics of the dyes SYTO 9 (green signals) and propidium iodide (red signals), respectively.

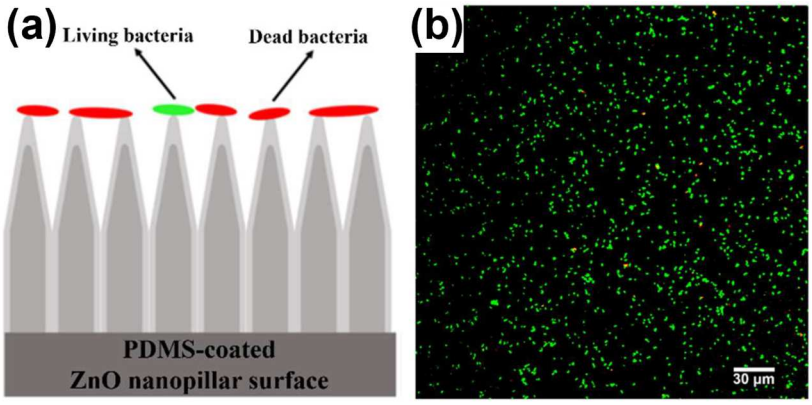

Figure 4.3. (a) Schematic diagram and (b) example image result of LIVE/DEAD staining experiments: Dead bacteria (colour of red) and living bacteria (colour of green).

For SEM analysis, new samples of incubated surfaces following the anti-biofouling protocol were prepared. Each sample was fixed in 4% paraformaldehyde for 10 minutes, then incubated in a series of ethanol-PBS solutions with an increasing ethanol concentration (10, 30, 50, 70, 90 and 100%). Each concentration solution was applied for 10 minutes, except for the 100% solution which required a 20-minute incubation. Dried samples were sputter-coated as described in Chapter 4.2.3 before the SEM analysis.

4.2.4.5 Bacterial coverage calculation

The bacterial coverage on surfaces was characterised utilizing FIJI. In this process, confocal microscopy images were imported into FIJI and subsequently converted to 8-bit images. The pixel intensity distribution in this process was visualized, enabling the identification of selected pixels or regions of interest, which were highlighted in white/grey. Subsequent image analysis included the determination of bacteria count, total area, average size, and coverage area. Figure 4.4 provides an illustrative example

of FIJI's capability in detecting bacteria attached to sample surfaces from confocal microscopy images.

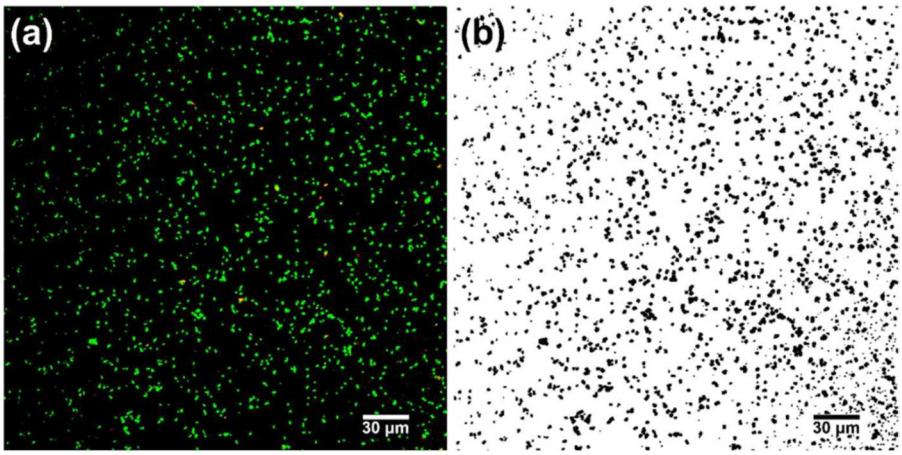

Figure 4.4. Illustrative example of bacteria characterisation based on confocal microscopy images: (a) Original confocal microscopy image and (b) FIJI converted image.

4.2.4.6 Multi-cycle surface tests

A series of multi-cycle surface tests were performed across 3 × 18 hours of incubation periods. The “Anti-biofouling efficacy testing” procedure was then followed for each multicycle test. Each test was subjected to a set of three repeats per surface type. After each test cycle, the surfaces were gently washed using fresh sterile water. The surfaces were then left to dry thoroughly at room temperature with good ventilation for 1 hour before being used for the next set of tests.

4.2.4.7 Cytotoxicity tests

Murine 3T3 fibroblast cells were cultured in Dulbecco's Modified Eagle Medium (DMEM) supplemented with 10% newborn calf serum, 4 mM GlutaMAX, 100 IU/mL penicillin, 100 µg/mL streptomycin, and 20 mM HEPES (4-(2-hydroxyethyl)-1-

piperazineethanesulfonic acid). The revived cell solutions were then seeded in Corning T75 cell culture flasks and incubated for 48 hours at 37°C with 5% CO2. Subsequently, cell attachment and growth were monitored under a phase-contrast microscope, and fresh culture medium was replenished every 2-3 days. When a confluent monolayer was observed, cells were passaged using trypsin-EDTA (0.25%), distributed into new T75 flasks, and confirmed the detachment of cells under the microscope. In this process, the number of viable cells could be determined by measuring a 20-μL aliquot of cell suspension mixed with an equal volume of Gibco Trypan blue stain (0.4%) using the Invitrogen Countess automated cell counter. 3T3 cells were then seeded onto various surfaces. After 15 minutes of incubation at 37°C with 5% CO2 to facilitate cell adhesion, 2 mL of culture medium was pipetted to each well. The cells were further incubated for 18 hours. Alamar blue assay was performed by adding Alamar blue solution to each well, incubating for 2 hours, and measuring absorbance at 570 nm using Infinite 200 Tecan automated luminometer-spectrometer. Cell counting was done by staining cells with trypan blue and using the cell counter. Statistical analysis was carried out using one-way ANOVA in IBM SPSS Statistic, with a 95% confidence interval.

4.3 Results and Discussions

4.3.1 Surface morphology

The morphology (roughness) and interfacial energy of a surface are the key factors in controlling its wettability. Therefore, an AFM characterization of surface roughness

has been carried out on ZnO nanopillar surfaces with and without PDMS coating, as shown in Figure 4.5a and b. The height of the nanopillars produced was mainly distributed between 350 and 400 nm with a typical diameter of 70–80 nm (Figure 4.6). These AFM measurements show that the structures are well-defined and relatively uniform. It should also be noted that the height of the nanopillars can be controlled by adjusting the duration and the concentration of reactants during nanopillar growth, as discussed in Chapter 3.

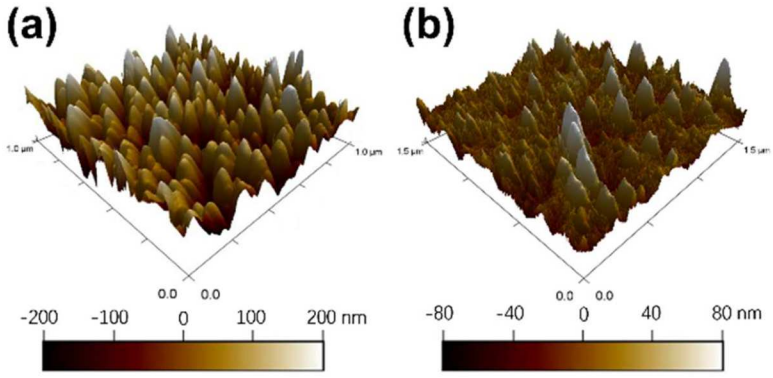

Figure 4.5. AFM images of (a) ZnO nanopillars and (b) PDMS-ZnO. The ZnO nanopillars are still visible after coating the PDMS.

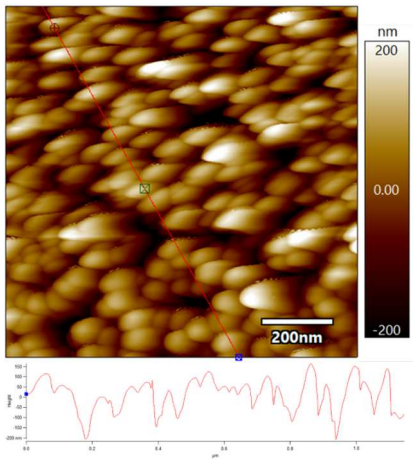

Figure 4.6. AFM image of ZnO nanopillars. The height of the nanopillars was mainly distributed between 350 and 400 nm with a typical diameter of 70–80 nm.

Table 4.1 presents a comparative analysis of surface roughness for different surface treatments; the related AFM images are shown in Figure 4.7. Specifically, the arithmetic average roughness (Ra) of the ZnO nanopillar surface without the PDMS coating was 58.9 ± 8.9 nm, and the RMS deviation (Rq) was 73.9 ± 11.0 nm. For ZnO nanopillar surfaces coated with PDMS, their surface roughness was considerably retained, with the Ra being 39.9 ± 27.4 nm and the Rq being 49.8 ± 33.3 nm. The substantial disparity in standard deviation observed in the roughness of the PDMS-coated nanopillars can be ascribed to the thickness of the PDMS coating. Thinner PDMS layers manifest higher surface roughness, converging toward the roughness levels observed of the uncoated ZnO nanopillars. The high roughness of these nanopillar surfaces was in marked contrast to the flat zinc substrate, PDMS surface, and glass slide.

Table 4.1 Roughness of surfaces

	Ra (nm)	Rq (nm)
ZnO nanopillars	58.9 ± 8.9	73.9 ± 11.0
PDMS-coated nanopillars	39.9 ± 27.4	49.8 ± 33.3
Bare Zinc	9.0 ± 2.0	11.3 ± 2.6
Pure PDMS	1.1 ± 0.3	1.3 ± 0.4
Glass slide	3.2 ± 1.2	4.2 ± 1.8

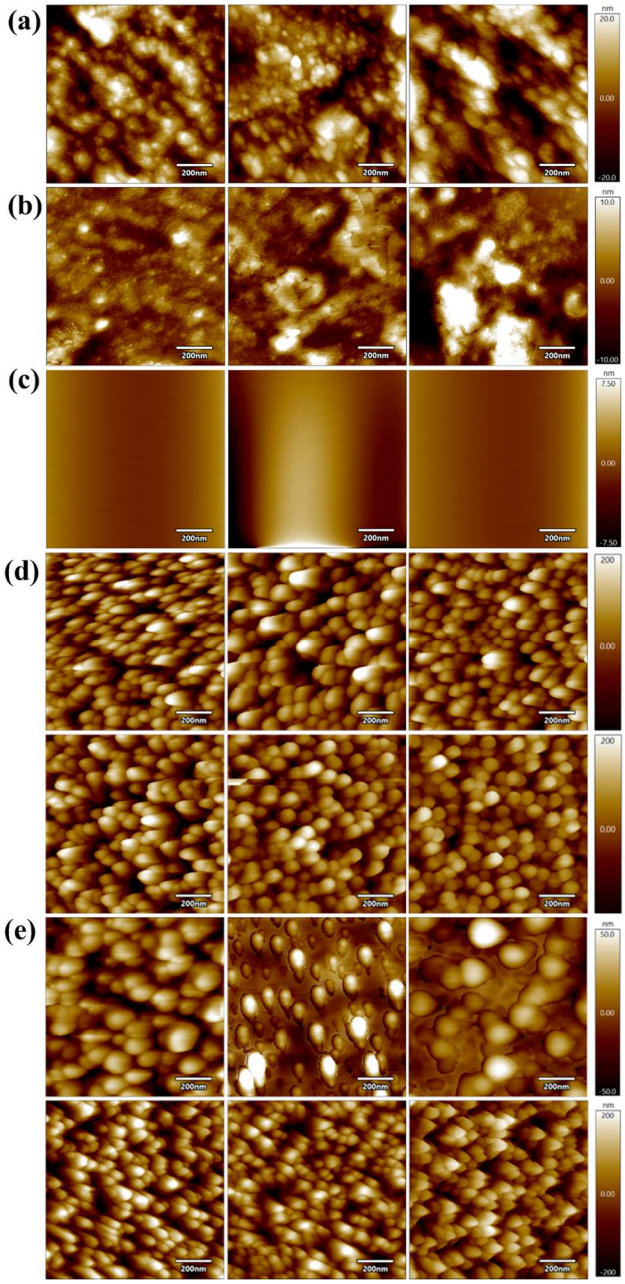

Figure 4.7. AFM images surfaces used in roughness calculation: (a) Bare zinc, (b) Glass, (c) Pure PDMS, (d) ZnO nanopillars and (e) PDMS-ZnO.

In addition to AFM, SEM images were also captured to study the morphology of the nanopillar surfaces before and after PDMS coating. Figure 4.8a shows the surface of typical ZnO nanopillars prepared via a 45 min hydrothermal synthesis reaction. This provides further validation to Figure 4.5a that the surface was indeed composed of

patterned pillar-like nanostructures. Similarly, Figure 4.8b validates the pattern of the PDMS-coated nanopillar surfaces as observed in Figure 4.5b, confirming that the sample exhibits fewer pronounced nanopillars due to the presence of the PDMS layer. Nonetheless, the outline of the nanopillars underneath is still noticeable from the SEM image (the contours and speckles in Figure 4.8b), Although the thickness of the PDMS coating is challenging to measure directly, approximate values can be obtained through mathematical calculation:

$$f = \frac{1.1\ \mathrm{mL}}{101.1\ \mathrm{mL}} \approx 0.011$$

$$\mathrm{V_{PDMS}} = 5\ \mu\mathrm{L} * 0.011 = 0.055\ \mu\mathrm{L} = 5.5 * 10^{-11}\ \mathrm{m}^3$$

$$\mathrm{T} = \frac{\mathrm{V_{PDMS}}}{1\ \mathrm{cm} * 1\ \mathrm{cm}} = \frac{5.5 * 10^{-11}\ \mathrm{m}^3}{1 * 10^{-4}\ \mathrm{m}^2} = 550\ \mathrm{nm}$$

where *f* is the effective solid fraction of PDMS, T is the approximate thickness of thin PDMS coating in this work. In the case of densely packed nanopillar arrays, PDMS may preferentially fill the gaps while leaving the pillars partially exposed. It is worth noting that the thickness of the PDMS coating could be subject to the volume and concentration of PDMS solution used in the coating process, as the calculated results of the thicker PDMS coating control group (using 25 μL drop-cast coating) reached about 2.7 μm, which far exceeded the height of the nanopillars, proving that it would completely cover the surface morphology, which was also confirmed by subsequent SEM results (Figure 4.22b, 4.23b).

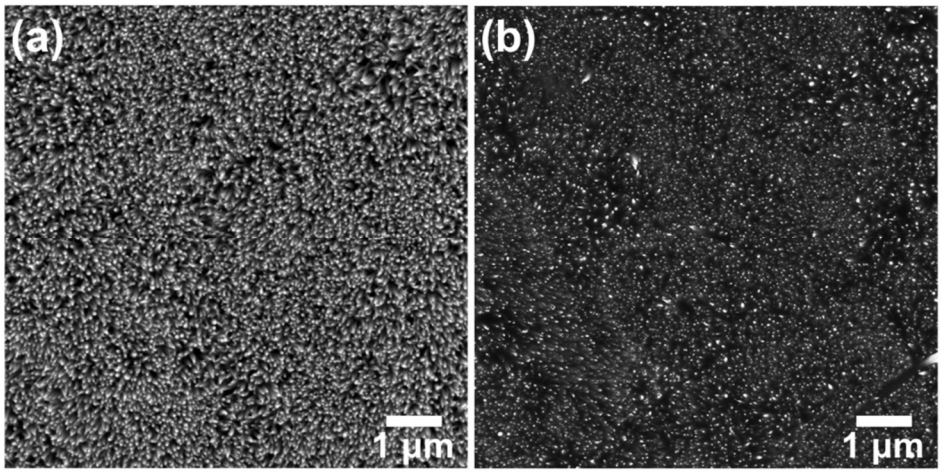

Figure 4.8. SEM images of (a) ZnO nanopillars and (b) PDMS-ZnO. The nanopillars are still visible after adding thin PDMS coating (sparkling tips in Figure b).

4.3.2 Surface characteristics

The crystallographic characteristics of the materials were investigated through XRD analysis, as shown in Figure 4.9. In the XRD spectrum of the ZnO nanopillars and PDMS-coated nanopillars, a prominent diffraction peak is observed at 2θ = 34.6° (002), indicating the highly preferential growth of ZnO nanopillars perpendicular to the substrate surface.

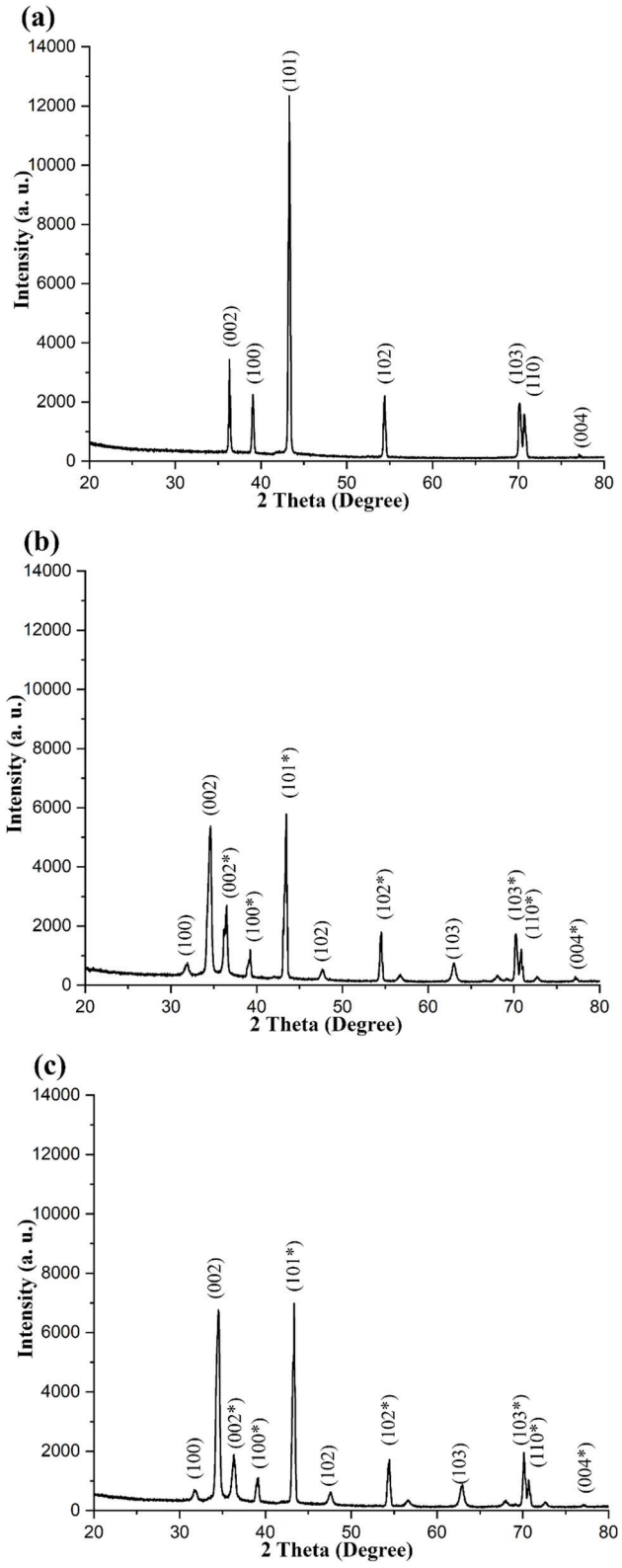

Figure 4.9. XRD results of (a) bare zinc, (b) ZnO nanopillars and (c) PDMS-ZnO.

Further, according to the FTIR results (Figure 4.10), Zn–O bond signals within the range of 500–700 cm^{-1} was identified for ZnO nanopillars fabricated by the hydrothermal synthesis reaction. On the other hand, generally, the presence of impurities corresponding to carboxylate and hydroxyl groups on the surface manifests as a series of absorption peaks spanning 1000–4000 cm^{-1} in the FTIR results. For instance, the peak at 1300–1450 cm^{-1} corresponds to O–H bending, 1400–1600 cm^{-1} corresponds to O═C–O bending, and 1700–1800 cm^{-1} corresponds to C═O stretching. In addition, the peaks at 2800–3000 and 3200–3600 cm^{-1} correspond to C–H and O–H stretching, respectively. These impurity-related peaks are notably absent in the ZnO nanopillar spectrum. The ZnO nanopillars coated with PDMS coating resultant from being exposed to 5 µL of PDMS solution during the coating process exhibit a similar trend, with slight alterations in the Zn–O bond signal, ascribed to the coating. Noteworthy is the absence of signals of Si–CH_3 rocking at 770–800 cm^{-1}, Si–O–Si stretching at 1100–1150 cm^{-1}, Si–CH_3 bending at 1260–1380 cm^{-1}, and Si–CH_3 stretching at 2960–2975 cm^{-1} in the results of PDMS-coated ZnO nanopillars, implying a low concentration of PDMS on the ZnO pillars. To examine the effect of PDMS coating thickness on surface characteristics, FTIR tests have been conducted on the ZnO nanopillar surface with a thick PDMS coating resultant from being exposed to an excessive 25 µL, instead of 5 µL, of PDMS solution during the coating procedure. In contrast, certain signals indicative of PDMS are more readily observed on surfaces with thick coatings.

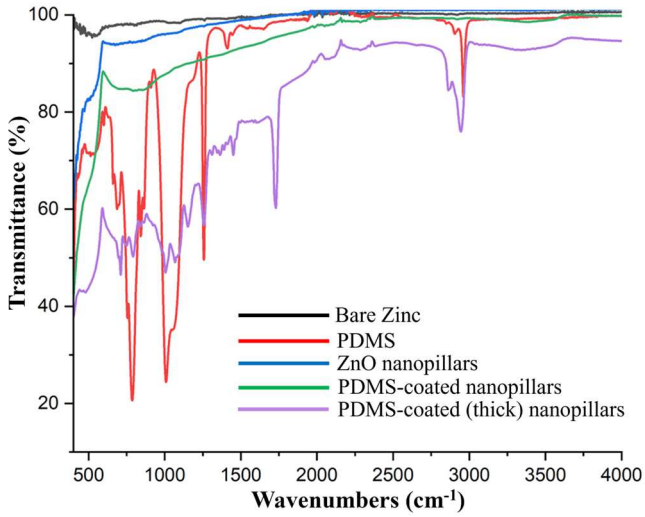

Figure 4.10. The FTIR spectra of samples.

The photocatalytic activities of each surface through fluorescence intensity decay are shown in Figure 4.11. The bare zinc surface exhibits slow degradation of the fluorescent dye. This suggests that the exposed zinc surface, which could form an oxide layer, lacks effective photocatalytic properties against fluorescent dyes. The pure PDMS surface exhibits negligible degradation of the fluorescent dye. In contrast, ZnO nanopillars exhibit rapid photocatalytic activities, degrading the dye within 3 hours. The PDMS coating on the ZnO nanopillars limits direct interaction between the dye molecules and ZnO, restricting the activity of ROS. As a result, the degradation of the fluorescent dye is slower (requiring 5 hours) compared to uncoated ZnO nanopillars, though it remains more effective than the bare zinc surface.

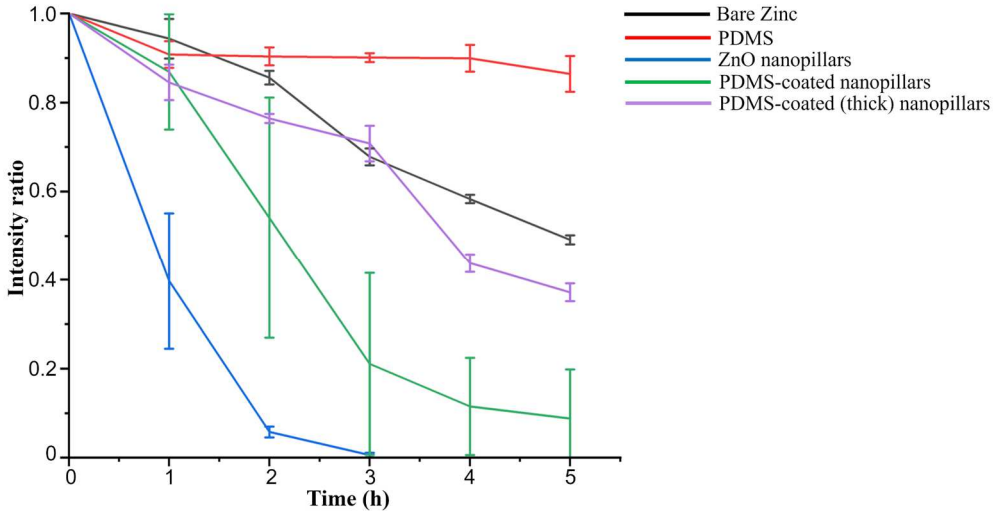

Figure 4.11. Fluorescence intensity changes of CF633 (n=9).

4.3.3 Surface wetting properties

Water is one of the mediums for bacteria to proliferate and spread in the initial stage of biofilm formation [144-146]. It is thus important to understand the wetting behaviour of water on the surfaces. The nanostructured surfaces have been analysed in terms of contact angle (CA) measurements. To better demonstrate the effect of the PDMS-coated nanopillars on wettability, we measured the bare zinc, ZnO nanopillars, and PDMS-coated nanopillars. Specifically, bare zinc exhibited a static contact angle of 77.8 ± 0.6° (Figure 4.12a), with the advancing and receding contact angles being 84.3 ± 1.7 and 46.6 ± 0.7°, respectively. For pure PDMS, the static contact angle was 106.1 ± 1.7° (Figure 4.12b), with the advancing and receding contact angles being 110.8 ± 1.6 and 85.6 ± 0.9°, respectively. This static contact angle is slightly higher than commonly reported value of approximately 100°, which can be influenced by factors such as PDMS concentration, curing conditions and measurement methods. The ZnO nanopillar structure directly obtained from the hydrothermal synthesis

reaction appeared superhydrophilic with a contact angle of 4.0 ± 0.5° (Figure 4.12c) and experimentally unmeasurable contact angle hysteresis. By contrast, the ZnO nanopillar structure coated with PDMS exhibited a contact angle of 152.6 ± 2.8° (Figure 4.12d).

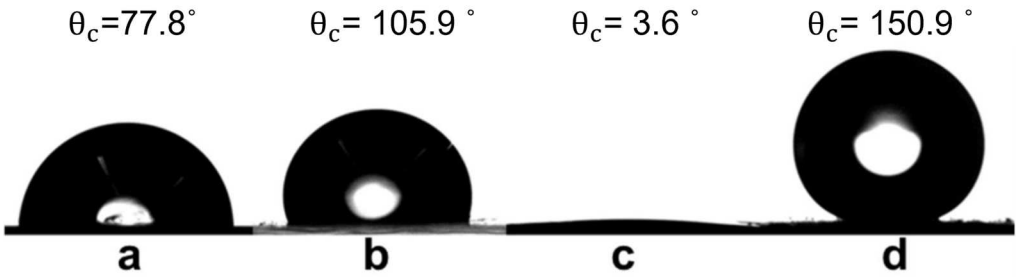

Figure 4.12. Water droplets contact angle on (a) bare zinc, (b)pure PDMS, (c) ZnO nanopillars and (d) PDMS-coated nanopillars.

The stability of the superhydrophobicity on the PDMS-coated ZnO nanopillars was also assessed, as shown in Figure 4.13. The contact angle only decreased about 2° during a 7-day laboratory environment exposure. Moreover, even after an extended exposure period of 21 days, a water contact angle of around 146° was still measured. Further, the contact angle hysteresis of the PDMS-coated ZnO nanopillar surface (now denoted as superhydrophobic) was negligible, with an advancing contact angle of 154.1 ± 0.2° and a receding contact angle of 152.3 ± 0.9°, as shown in Figure 4.14.

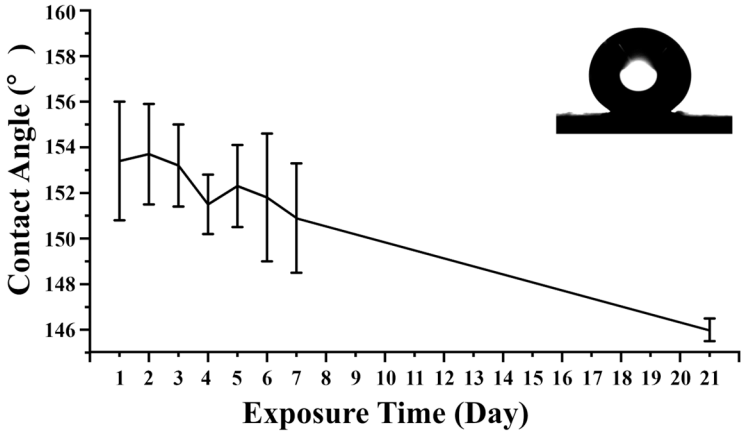

Figure 4.13. Droplet contact angle on PDMS-coated ZnO nanopillars as a function of time. The inset shows that the water contact angle was around 146 ± 0.5° even after 21 days (n=9).

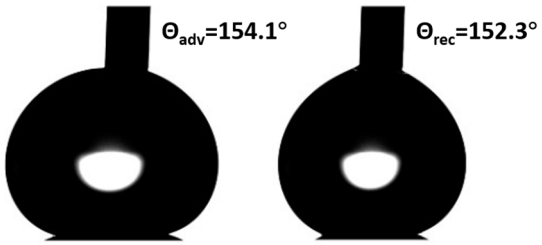

Figure 4.14. Measurement of dynamic contact angles of water on PDMS-coated ZnO nanopillars.

In addition, it is interesting to note that water droplets can roll off of the PDMS-coated nanopillar surface at a tilting angle of 1°, as shown in Figure 4.15. The superhydrophobicity with minimal tilt angle is attributed to the combination of the PDMS coating and the rough ZnO nanopillars. In particular, as shown in Figure 4.8b, the PDMS coating was sufficiently thin to allow the surface roughness and function resulting from the ZnO nanopillars to be preserved.

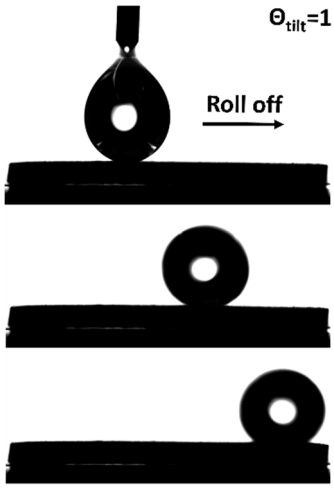

Figure 4.15. Water droplet rolling off on PDMS-coated ZnO nanopillars.

The superhydrophobic surfaces also repelled the impact of water droplets of 2.7 mm diameter at different velocities (U_1 = 0.48 ms^{-1} and U_2 = 1.11 ms^{-1}). Figure 4.16 a and b shows the morphology variations of the droplets after impacting the surfaces with different values of the Weber number (Equation 2.5). It can be found that the droplet directly rebounded from the superhydrophobic surface at a range of *We* values (*We* = 8.62 and *We* = 46.11), which corresponds to the lowest (h =14 mm) and highest (h =70 mm) syringe positions of the goniometer.

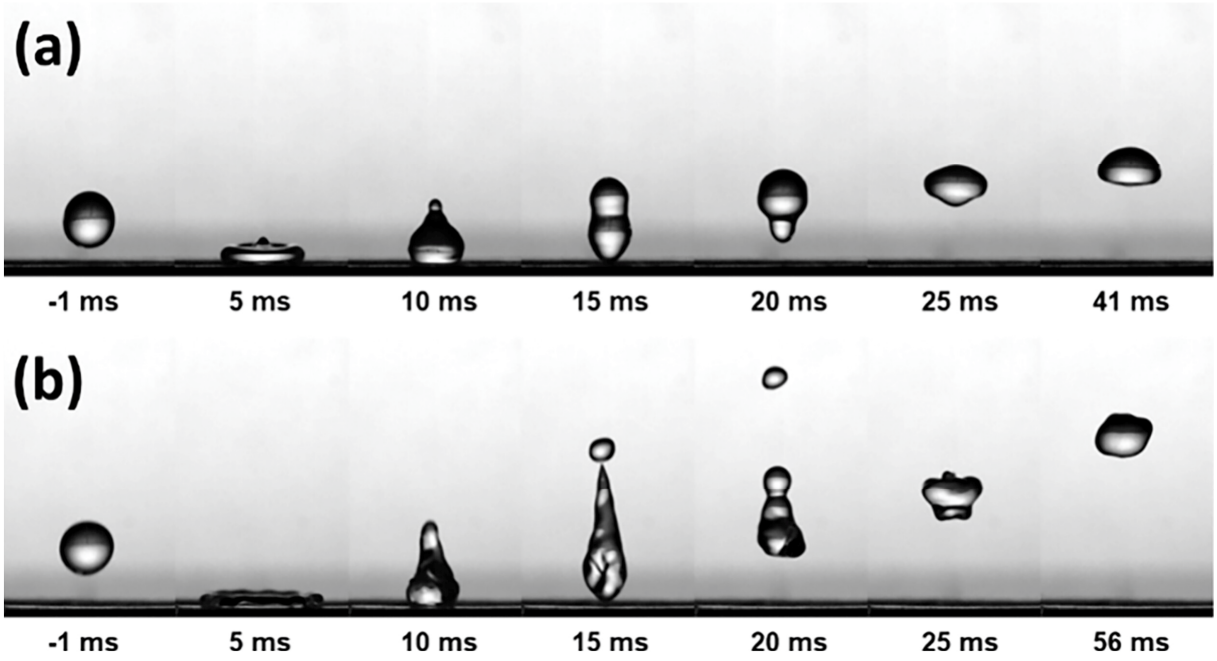

Figure 4.16. Water droplets impacting PDMS-coated nanopillar surfaces: (a) *We* = 8.62 and (b) *We* = 46.11. Droplet impact experiments were captured by a high-speed camera at a frame rate of 1000 fps.

At the beginning of the impact, the droplet recoiled to a pancake shape, which was dominated by inertial effects. This was followed by complete rebounding of the droplet from the superhydrophobic nanopillar structure. However, at a higher *We* (46.11), a satellite droplet was generated from the primary droplet. This was because the kinetic energy is higher than the stabilizing force of the surface tension, causing the rim of the droplet to break up. In addition, as shown in Figure 4.17, the higher *We* also led to a higher maximum height and rebounding speed than the lower *We*. The initial rebound was followed by a series of subsequent rebounds with a gradual decrease in the impact velocity.

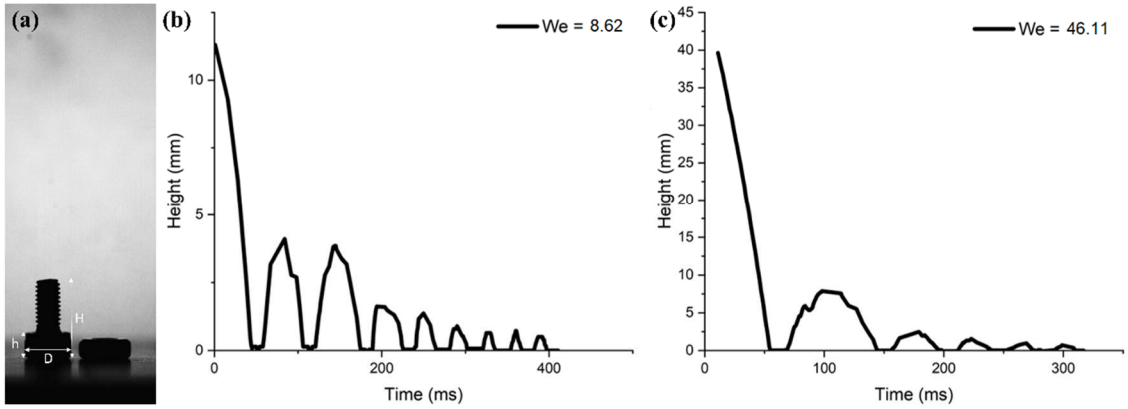

Figure 4.17. (a) Dimension calibration: 1 pixel in the image should be equal to 0.037 mm. Full bouncing series and velocity change of a water droplet (D_o = 2.7 mm) on superhydrophobic PDMS-coated nanopillars with (b) *We* = 8.62 and (c) *We* = 46.11.

Table 4.2 Dimension calibration of droplet impact tests

	Screw total height (H)	Screw head diameter (D)	Screw head thickness (h)
Real size (mm)	9	5.45	3
Pixels	250	148	79
Converting ratio	0.036 mm/pixel	0.037 mm/pixel	0.038 mm/pixel
The converting ratio used in the calculation = 0.037 ± 0.001 mm/pixel (average)			

Table 4.3 Weber number calculation

	Impact time (Frame)	Impact distance (Pixel)	Converted impact time (ms)	Converted impact distance (mm)	Impact velocity calculation (ms^{-1})	Weber number
Impact 1	1	13	1	0.48	0.48	8.62
Impact 2	1	30	1	1.11	1.11	46.11

By contrast, impacting droplets spread immediately against the uncoated surface of ZnO nanopillars (Figure 4.18a). Similarly, the droplet did not rebound on the pure PDMS surface (Figure 4.18b), although it retracted due to its hydrophobicity after spreading out upon impact. Therefore, it is deduced that the superhydrophobic

nanopillar structure prevented the water droplets from spreading into the nanostructure even under impact conditions. Figure 4.14 focuses only on higher We because it represents a critical threshold where inertial forces dominate, making impalement or spreading more likely. This ensures a direct evaluation of surface robustness under strong impact conditions. This further implies that air pockets existed among the nanopillars coated with a thin layer of PDMS, which, as a result, repelled impacting droplets.

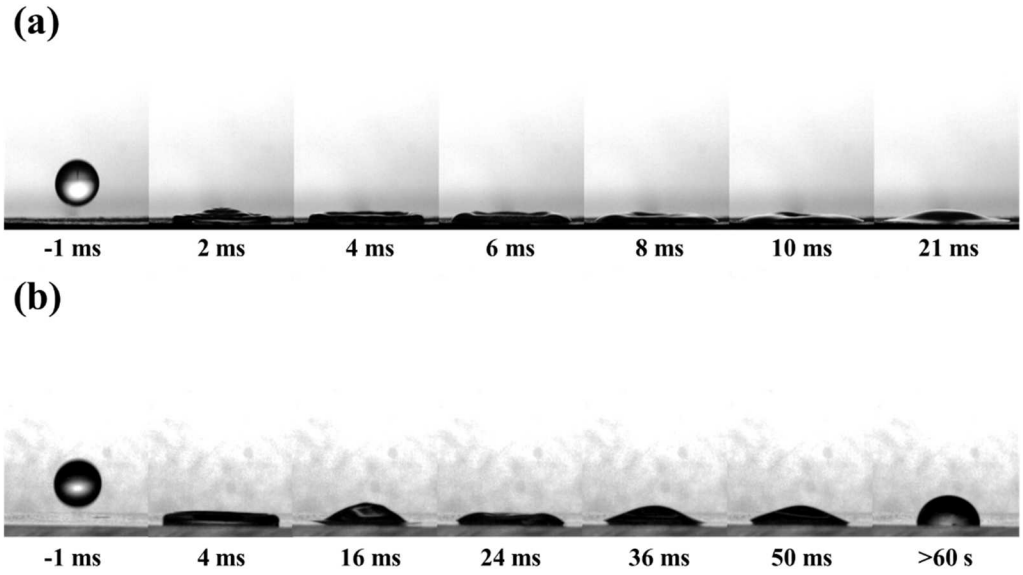

Figure 4.18. Water droplet impacting on (a) uncoated ZnO nanopillar surfaces and (b) pure PDMS surface with *We* = 46.11.

4.3.4 Surface antibiofouling properties

In order to examine the antibiofouling properties of the PDMS-coated ZnO nanopillars, bacterial viability tests were performed with dual staining kits. This allowed us to assess the viability of bacterial populations on the superhydrophobic surfaces as a function of the cell's membrane integrity. Namely, cells that were dead or dying on

the structured surfaces because of a compromised membrane stained red, whereas cells with an intact membrane appeared green, as schematically illustrated in Figure 4.3. The confocal microscopy images of stained *S. aureus* bacterial suspensions incubated for 18 hours on the bare zinc, ZnO nanopillars, and PDMS-coated nanopillars are shown in Figure 4.19a, respectively. The confocal microscopy examination revealed that nearly half amount of *S. aureus* remained alive when exposed to the bare zinc surface, as indicate by green fluorescence signals. In contrast, the bacteria exhibited almost 100% red dead-cell signals on the superhydrophilic ZnO nanopillar surface. However, despite the bactericidal properties, the number of dead bacteria adhering to the superhydrophilic ZnO nanopillar surface accumulated over time, as shown in Figure 4.19bii. The antibiofouling properties of uncoated ZnO nanopillars may be compromised when bacteria cells accumulate and cover the surface, reducing the bactericidal effectiveness through direct bacteria-surface contact [147]. In comparison, the PDMS-coated nanopillar surface showed a noticeable reduction in bacterial presence by observe the signals, although a coexistence of live and dead bacteria persisted. Nonetheless, bacterial coverage was significantly lower with reduction over 95% on the superhydrophobic ZnO nanopillars, likely due to the low adhesion, than on the bare zinc and untreated ZnO nanopillars. SEM images of *S. aureus* on the bare zinc, ZnO nanopillars, and PDMS-coated nanopillars are shown in Figure 4.19b. It is evident that *S. aureus* initiated the formation of biofilm on the bare zinc surface following an incubation of 18 hours. Bacterial remnants that were

deformed/dehydrated were observed on the ZnO nanopillars. This is consistent with the confocal microscopy analysis that showed the nonviability of the bacterial population of *S. aureus* on the uncoated ZnO nanopillars. By contrast, large *S. aureus* colonies were not observed on the superhydrophobic ZnO nanopillars. SEM analysis revealed that *S. aureus* bacteria were present in low numbers and scattered across the PDMS-coated ZnO nanopillars, consistent with the confocal microscopy results. A closer observation (Figure 4.19biii) indicates that some of the bacteria appeared to be structurally deformed after being exposed to the PDMS-coated ZnO nanopillars. Tests were also conducted with an incubation time of 72 hours to examine whether the antibiofouling effect could be sustained on the surfaces for longer durations. The confocal microscopy and SEM images reveal that on the bare zinc surface, *S. aureus* cells were still able to survive and form biofilms (Figure 4.19ci, di). In contrast, the ZnO nanopillars continued to exhibit similar trends to the 18 hours incubation, with an extensive coverage of dead bacteria, as shown in Figure 4.19cii, dii. On the superhydrophobic ZnO nanopillars coated with PDMS, the longer incubation of 72 hours allowed the accumulation of *S. aureus* to moderately increase, as shown in Figure 4.19ciii, diii, in comparison with the 18 hours incubation. Nevertheless, the coverage of bacteria after 72 hours of incubation on the superhydrophobic PDMS-coated ZnO surface was still less than on the uncoated ZnO surface. Also, the bacteria that were residual on the superhydrophobic surface appeared to be dead as showing red signals (Figure 4.19ciii). This is attributed to the extended exposure to the

photocatalytic activities of ZnO underneath the surface that caused the bacteria to be structurally deformed (Figure 4.19diii).

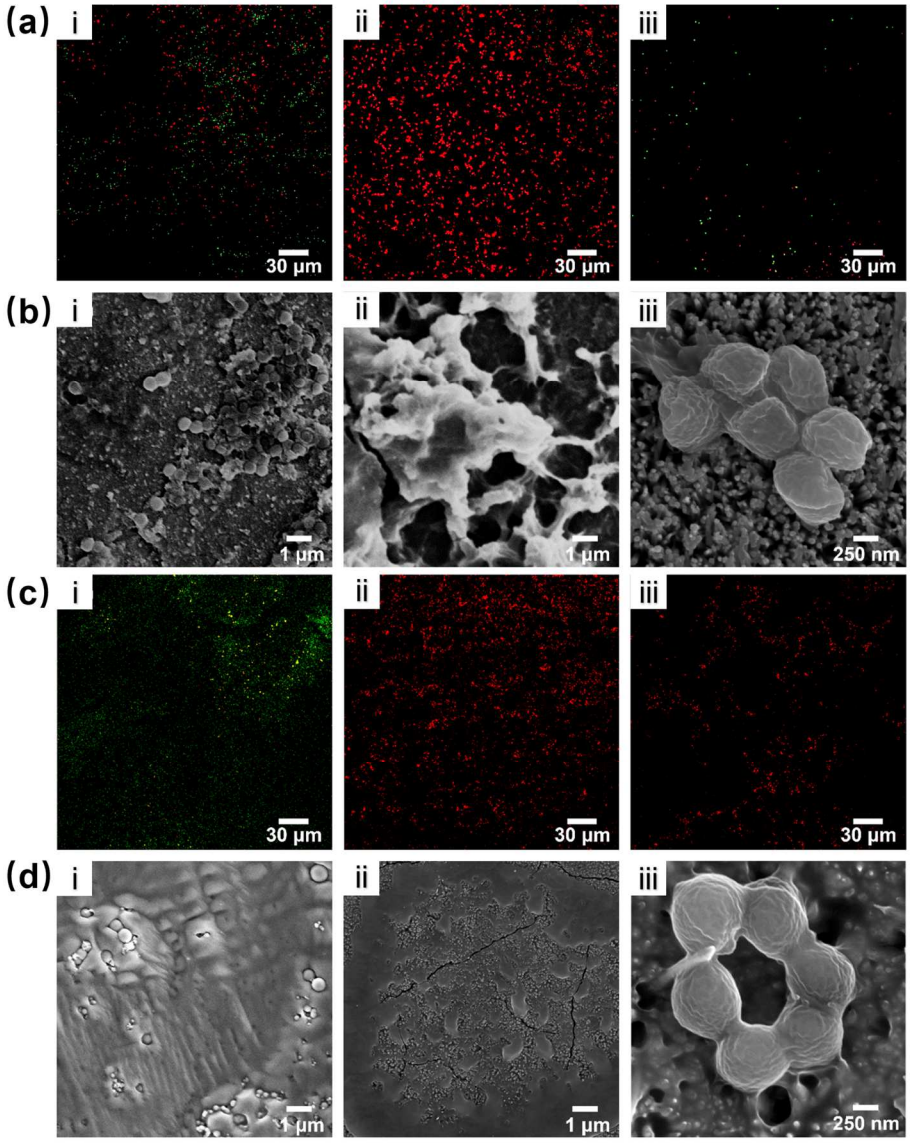

Figure 4.19. Confocal microscopy (a, c) and SEM (b, d) images of *S. aureus* after 18 (a, b) and 72 (c, d) hours of incubation, respectively, on different surfaces: (i) bare zinc, (ii) ZnO nanopillars and (iii) PDMS-coated nanopillars.

Furthermore, the confocal microscopy images (Figure 4.20a) show stained *E. coli* bacterial suspensions incubated for 18 hours on different surfaces: the bare zinc, ZnO

nanopillars and PDMS-coated nanopillars. Similar to the findings with *S. aureus*, most bacteria of *E. coli* were green stained on the bare zinc surface, whereas appeared red stained on the ZnO nanopillars. However, on PDMS-coated nanopillars, the stained *E. coli* emitted red signals indicative of dead cells. This is attributed to the disparities in bacterial morphology and inner structure between *S. aureus* and *E. coli*. Generally, *S. aureus* is usually spherically shaped, with a diameter of approximately 0.5 to 1.0 μm and a thicker peptidoglycan layer than *E. coli*. In contrast, *E. coli* is typically rod-shaped, with a width of 0.5 μm and a length of 1.5 μm [148-150]. The differences in structural morphology between the bacteria may have had an effect on their viability on the nanopillar-based structures. The shape of the *E. coli* bacteria could have had greater surface contact with the nanopillar structures than that of *S. aureus*, even in the presence of the PDMS layer. This would impose a stressful stimulus on bacterial cell walls, causing irreparable cell wall rupture and bacterial death [151]. Indeed, SEM images (Figure 4.20b) further illustrate that bacteria of *E. coli* with disfigured appearances were observed on both the uncoated ZnO nanopillars (Figure 4.20bii) and the PDMS-coated ZnO nanopillars (Figure 4.20biii). This was more notable on the uncoated ZnO nanopillar structure, which could cause the bacteria to be punctured as adhesive forces pulled them towards the surface due to its superhydrophilicity [152]. Nevertheless, the PDMS-coated ZnO nanopillars, because of the low interfacial adhesion associated with the superhydrophobicity, reduced the attachment of *E. coli* on the surface. The 72-hour incubation test was also performed for *E. coli*, with

confocal microscopy and SEM images collected to analyse the behaviour of *E. coli* on different surfaces. Bacterial cells on bare zinc still exhibited green signals and displayed a tendency to form large-area biofilms (Figure 4.20ci). SEM observations confirmed the presence of some large-area biofilms on the surface, as shown in Figure 4.20di.

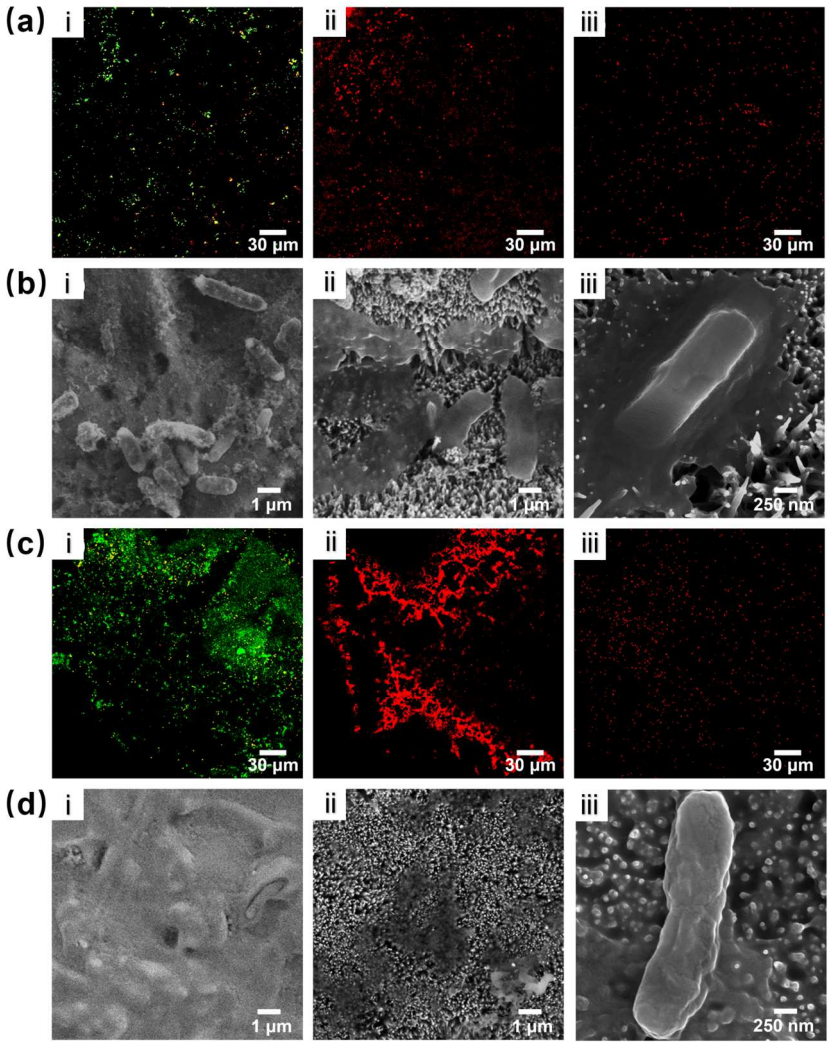

Figure 4.20. Confocal microscopy (a, c) and SEM (b, d) images of *E. coli* after 18 (a, b) and 72 (c, d) hours of incubation, respectively, on different surfaces: (i) bare zinc, (ii) ZnO nanopillars and (iii) PDMS-coated nanopillars.

In contrast, the trend observed after the 72-hour incubation of the uncoated ZnO nanopillars and the superhydrophobic ZnO nanopillars remained essentially consistent with that observed after the 18-hour incubation. It is worth noting that in addition to the results of the above three kinds of surfaces, confocal microscopy and SEM images of the control group, glass, and pure PDMS were also collected at different incubation times (18-hour and 72-hour), as shown in Figures 4.21-23. It is worth noting that the term “control” in this work refers to tests wherein the bacteria are exposed to conditions without any specific surface material. From the results, it can be observed that bacteria could proliferate in the control group and remained active. Similarly, as neither glass nor PDMS possessed inherent anti-biofouling properties, they also allowed substantial proliferation and biofilm formation to take place. Therefore, bacteria on surfaces of ZnO nanopillars with excessive PDMS coatings did not exhibit any noticeable deformation (Figures 4.22 and 23).

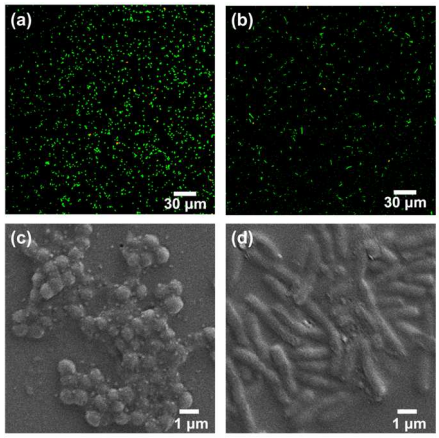

Figure 4.21. Confocal microscopy (a, b) and SEM (c, d) images of bacteria from the “no surface” control group after 18 hours of incubation: *S. aureus* (a, c) and *E. coli* (b, d).

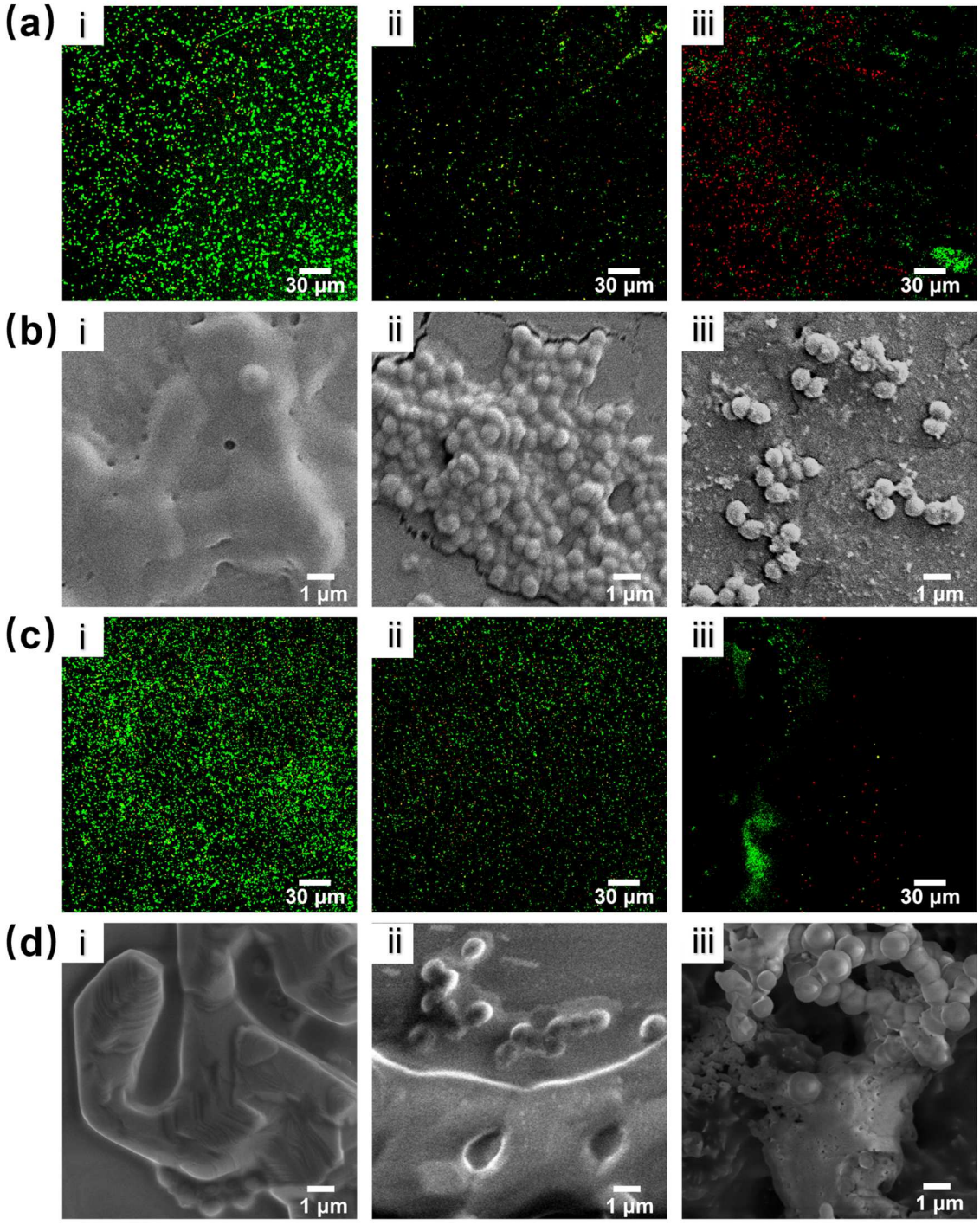

Figure 4.22. Confocal microscopy (a, c) and SEM (b, d) images of *S. aureus* after 18 (a, b) and 72 (c, d) hours of incubation, respectively, on different surfaces: (i) glass, (ii) pure PDMS and (iii) thick PDMS-coated nanopillars.

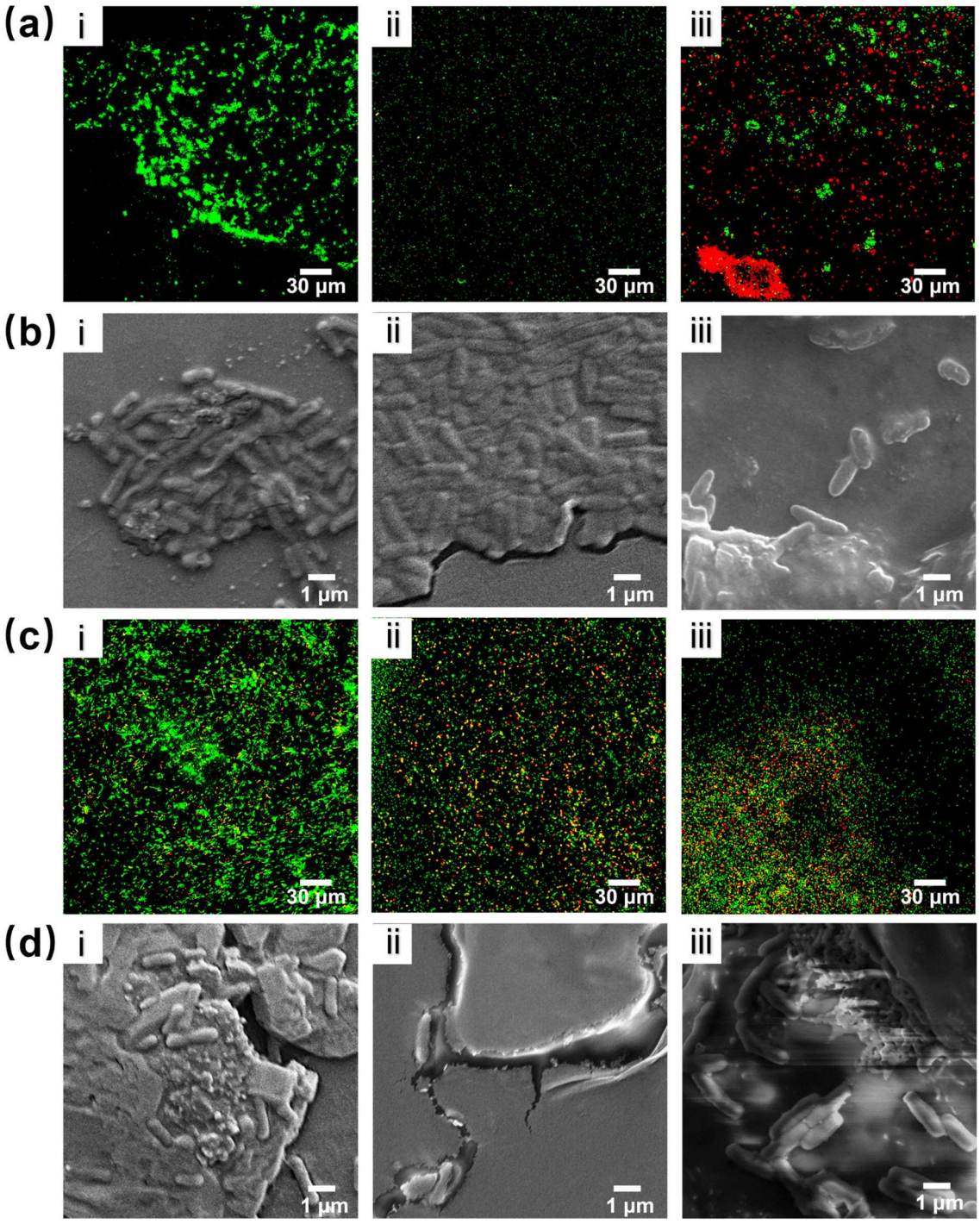

Figure 4.23. Confocal microscopy (a, c) and SEM (b, d) images of *E. coli* after 18 (a, b) and 72 (c, d) hours of incubation, respectively, on different surfaces: (i) glass, (ii) pure PDMS and (iii) thick PDMS-coated nanopillars.

The coverage percentage of bacteria populations on various surfaces was calculated based on the confocal microscopy images, as shown in Figure 4.24 (a) and (c) corresponding to the 18-hour and 72-hour of incubation, respectively [153]. A consistent trend is observed where the bacterial coverage on superhydrophobic PDMS-coated nanopillars was reduced by 96.5% and 87.5% after 18-hour incubation and by 94% and 93% after 72-hour incubation, respectively, compared to the number of *S. aureus* and *E. coli* on glass. This is attributed to the low liquid-solid adhesion associated with the superhydrophobicity of the surfaces that were characterised by the small contact angle hysteresis and tilting angle. At 18-hour of incubation, bacterial adhesion varied widely across the tested surfaces. The highest bacterial coverage was observed on glass substrates, reaching approximately 15% for *S. aureus* and approximately 7% for *E. coli*. In contrast, control surfaces had significantly lower bacterial coverage, below 5% for both bacteria. Surfaces of pure PDMS and bare zinc exhibited moderate bacterial attachment, with percentage coverage ranging between 2% and 5%. PDMS-coated nanopillars had the lowest bacterial coverage, with coverage below 1% for both *S. aureus* and *E. coli*, indicating a significant reduction in bacterial attachment due to a combination of nanoscale topography and surface chemistry. Similar trends were observed after 72-hour of incubation, with bacterial attachment increased for all surfaces. Glass surfaces remained the most susceptible to bacterial colonization, with coverage increasing to approximately 17% for *S. aureus* and 14% for *E. coli*, respectively. Bacterial coverage increased for pure PDMS and

bare zinc, with the increase being more pronounced for *E. coli*. The PDMS-coated nanopillars remained the most effective in reducing bacterial coverage, maintaining values below 2%, demonstrating sustained antibacterial efficacy. Quantitative analysis showed that bacterial attachment was significantly affected by surface properties, including material composition and nanostructure. PDMS-coated ZnO nanopillars exhibited excellent antibacterial properties at both incubation times, effectively reducing bacterial attachment. Additionally, the antimicrobial properties of the surfaces are quantitatively illustrated in Figure 4.24(b) and (d), using colony-forming units (CFU) calculation. Notably, there was very few CFU that could be detected from the samples which had been exposed to the superhydrophilic ZnO nanopillars in both the cases of 18-hour and 72-hour incubations. This is consistent with recent studies that nanostructures of ZnO can exhibit antimicrobial activities through bacterial cell wall damage [154, 155]. In particular, a recent study used a similar approach to the development of ZnO nanopillars coated with PDMS for antibacterial applications [138]. It is noteworthy that in our case, the ZnO nanopillars exhibited more uniform upright morphologies, which had been preserved even in the presence of PDMS coatings (Figure 4.7b). This makes it possible to enhance the antimicrobial properties of the surfaces through a combination of the two following complementary mechanisms: (a) direct bacterial membrane puncture and (b) photocatalytic activities of ZnO. However, there is a possibility that PDMS layers exceeding a certain thickness, typically several nanometres, could impede or slow down the photocatalytic activity [15, 156]. Thicker

PDMS layers also obscure the nanopillar structure, hindering the mechanical stress of the pillars against the bacteria. This will affect the surface's anti-biofouling behaviours, as shown in Figure 4.22, Figure 4.23 and Figure 4.25. The "PDMS-coated nanopillars" mentioned in Figure 4.24 are all thin coating samples. For Figure 4.25, the 18-hour incubation period was sufficient to allow *S. aureus* and *E. coli* to enter the exponential growth phase, allowing the evaluation of their proliferation on the PDMS-coated nanopillar surfaces.

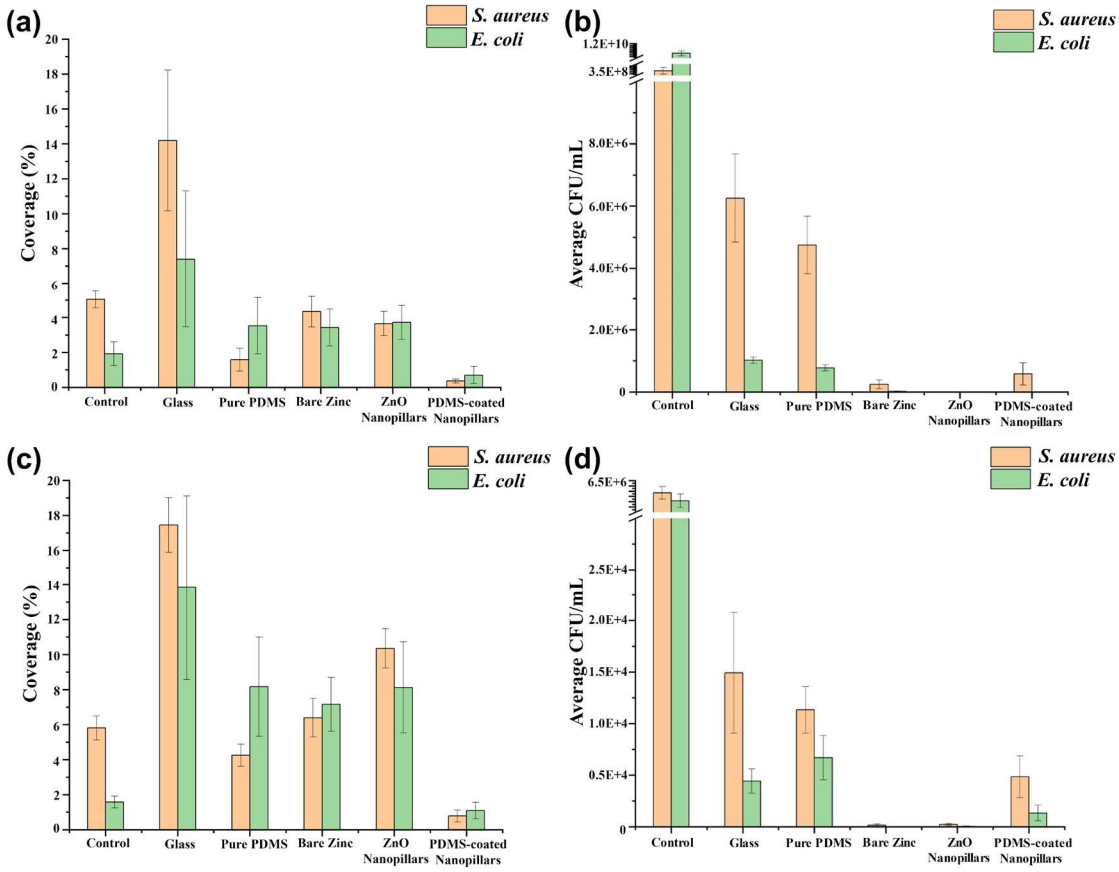

Figure 4.24. The coverage percentage of bacteria population after (a) 18-hour and (c) 72-hour incubation, (n=27). The number of colony forming units (CFU)/mL on each surface sample after (b) 18-hour and (d) 72-hour incubation, (n=27).

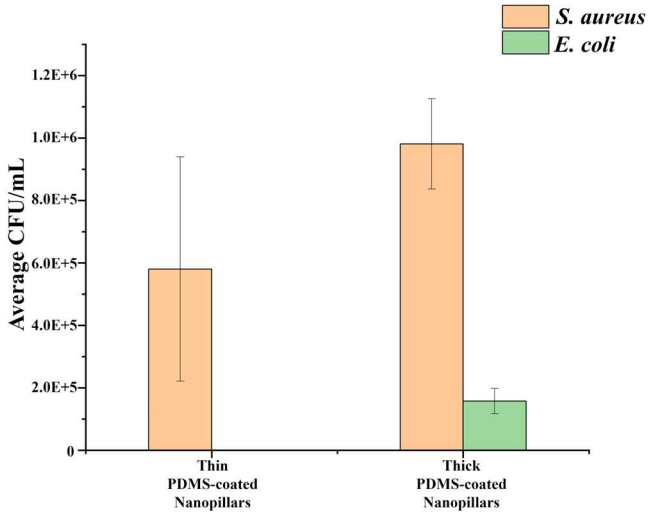

Figure 4.25. The number of colony forming units (CFU)/mL on different PDMS-coated nanopillar surfaces after 18-hour incubation (n=27).

On the other hand, the number of CFU on ZnO nanopillars is significantly lower than glass and pure PDMS (over 99.9%). Further, the CFU results on bare zinc surface also showed the same trend, which may be attributed to the presence of an ZnO layer, which could contribute to inhibit bacterial activity. However, given that live bacteria signals can be widely found on the zinc surfaces under confocal microscopy, they are not considered to be resistant to biofouling. Furthermore, to evaluate the efficacy of superinfection prevention, 3 rounds of multi-cycle tests were implemented (Figures 4.26 and 4.27). The antibacterial response and behaviour of each sample type over the multiple cycles of testing aligned consistently with the trends observed in the initial anti-biofouling efficacy testing.

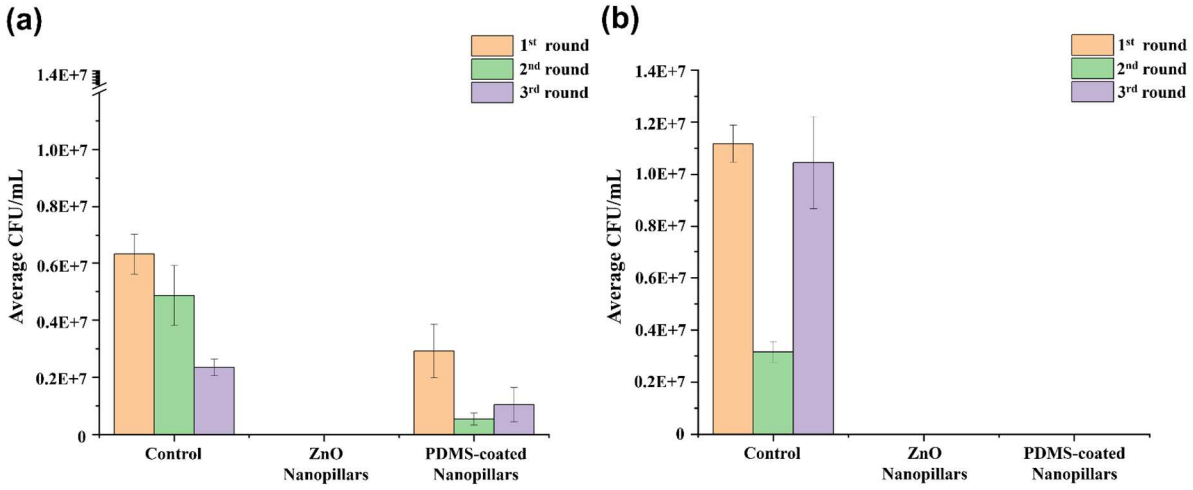

Figure 4.26. The number of colony forming units (CFU)/mL on the ZnO nanopillar-based surfaces of (a) *S. aureus* and (b) *E. coli* after three rounds of 18-hour incubation (n=27).

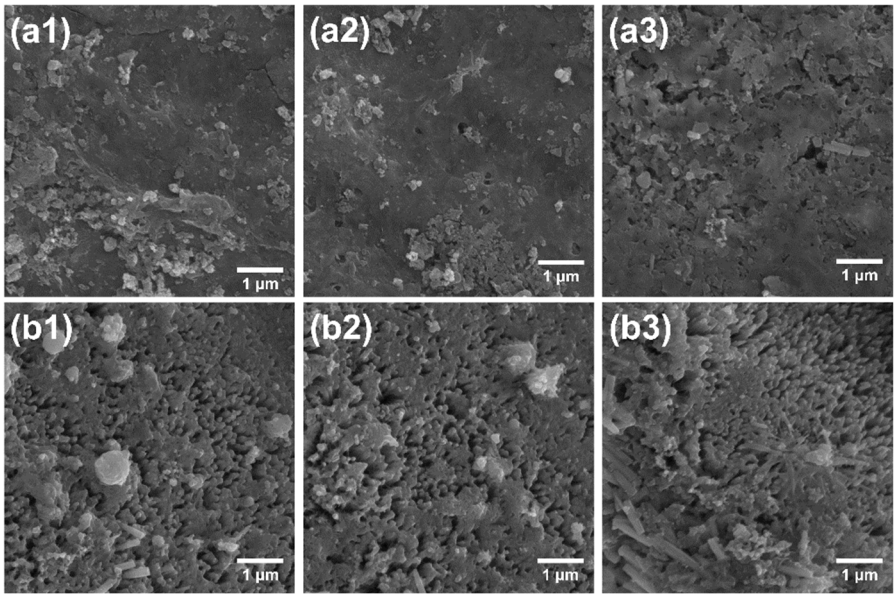

Figure 4.27. SEM images of surface morphology after multi-cycle tests: (a) ZnO nanopillars and (b) PDMS-coated ZnO nanopillars.

In addition, ZnO nanopillars and PDMS-coated nanopillars showed no signs of cytotoxicity against mammalian Murine cells (Figure 4.28), implies that the metabolism

of resazurin in the Alamar blue solution was not significantly different, and consequently, the viability of the 3T3 fibroblast cells remained unaffected. The treated surfaces exhibited biocompatibility, as indicated by the absence of significant cytotoxic effects against mammalian cells. The average absorbance at 570 nm per cell remained comparable across all surfaces, suggesting that cell viability was maintained without adverse effects.

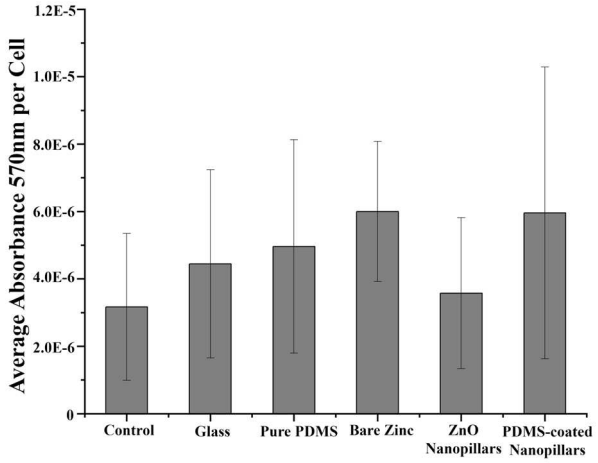

Figure 4.28. Cytotoxicity results from different surfaces (n=9).

4.4 Conclusion

In conclusion, ZnO nanopillars were coated with PDMS to form superhydrophobic surfaces with antibiofouling properties. Droplets of water on these superhydrophobic surfaces exhibited large apparent contact angles and low contact angle hysteresis of within 3°. In addition, such surfaces showed low droplet adhesion, characterized by a low tilting angle of 1°. The liquid repellence of the surfaces was further demonstrated by droplet impingement tests, where impinging droplets bounced off over a range of Weber numbers (8–46). Notably, the PDMS-coated ZnO nanopillars exhibited effective

antibiofouling behaviours under ambient illumination due to the intrinsic photocatalytic activities of ZnO nanomaterials. Therefore, the superhydrophobic PDMS-coated ZnO surfaces integrated a low interfacial adhesion and bactericidal effect. This synergy, without requiring additional UV illumination or antimicrobial agents, makes the PDMS-coated ZnO nanopillar surfaces a promising material for antibiofouling applications.

CHAPTER 5 WETTABILITY AND INHERENT ANTIBACTERIAL PROPERTIES OF LUBRICANT-INFUSED SURFACES

5.1 Introduction

The thin PDMS/ZnO superhydrophobic surface introduced in Chapter 4 demonstrated effective antibiofouling properties, killing *S. aureus* (Gram-positive) and *E. coli* (Gram-negative) while significantly reducing bacterial adhesion. However, the long-term stability of superhydrophobic surfaces remains a critical challenge in practical applications. Exposure to environmental factors (such as humid environment) over time or subject to mechanical damage can degrade their superhydrophobicity, thereby affecting their antibiofouling efficacy. In contrast, lubricant-infused surface (LIS) is designed by infusing low interfacial tension liquids into micro/nanostructures to form a dynamic lubricating layer, which provides a more stable and durable anti-biofouling strategy through its sustained slipperiness as well as self-healing properties.

To systematically investigate the bactericidal and anti-adhesion mechanisms of LIS and compare different surface engineering strategies for water-repellent surfaces, this chapter presents the fabrication and evaluation of LIS samples prepared by infusing PDMS-based silicone oil into ZnO nanopillar arrays (LIS-ZnO), as well as a fluorosilane-coated superhydrophobic surface (SHS-ZnO) as a control. One major difference between the experimental design in this chapter and that in Chapter 4 is the choice of superhydrophobic control. The PDMS-coated ZnO nanopillars used in the previous chapter were not chosen as controls in this chapter to avoid potential

experimental confounding factors. Specifically, since the lubricant infused into the LIS is also PDMS-based, using a similar coating material as a control would introduce overlapping material properties that could mask the intrinsic differences between LIS and traditional superhydrophobic coatings. To ensure a more rigorous comparison, a chemically different silane-based superhydrophobic surface was used, which not only eliminates interference caused by identical material properties but also serves as a referenced material that has been extensively studied in the literature due to its ability to form low surface energy superhydrophobic coatings.

Another key distinction between this chapter and Chapter 4 is the selection of bacterial cultures, which are Gram-negative bacterial *Escherichia coli* (*E. coli*) and *Pseudomonas syringae pv. Syringae* (*Pss*). *E. coli* was selected for its well-documented ability to form robust biofilms across diverse environments, while *Pss* was chosen for its unique adhesion properties and its propensity to develop dynamic biofilm structures. This chapter aims to investigate the anti-biofouling ability of the prepared surfaces against bacteria with different biofilm formation patterns. Since Gram-positive bacteria (such as *S. aureus*) have a thicker peptidoglycan layer and their cell wall structure is very different from that of Gram-negative bacteria, differences in biofilm inhibition rates due to intrinsic differences in cell wall composition may be falsely attributed to material efficacy.

In this chapter, a series of wettability, photocatalytic, and anti-biofouling experiments were conducted to systematically assess the performance of LIS-ZnO.

Wettability testing included measuring the water CA, SA, and CAH of the surface. The stability of the lubricating layer was further characterized by tape stripping tests and repeated droplet wetting cycles, which allowed quantification of its stability under mechanical and environmental stresses. Photocatalytic testing was measured by both optical observation and by reading the intensity changes of fluorescent dye droplets placed on samples using the microplate reader. Comparative antibacterial testing was performed using *E. coli* and *Pss* to evaluate the viability and attachment/adhesion of bacteria on bare Zn, ZnO nanopillars, SHS-ZnO, and LIS-ZnO. By focusing on two bacterial species with different biofilm formation strategies, the work in this chapter provides new insights into how LIS-ZnO mechanisms mitigate bacterial colonization, highlighting their potential applications in the healthcare industry.

5.2 Methodology

5.2.1 Materials

The materials (pure zinc foils) and reagents (sodium hydroxide, zinc nitrate hexahydrate, ethanol, acetone, and DI water) used for the pre-treatment and preparation of ZnO nanopillars have already been discussed in Chapter 3.2.1. Silicone oil (polydimethylsiloxane, $[-Si(CH_3)_2O-]_n$, molecular weight = 74.15, viscosity = 20 cSt) and 1H,1H,2H,2H-perfluorooctyl silane (FAS) were utilized for modifications of the ZnO nanopillars. *E. coli* and *Pss* were employed in the bactericidal efficacy testing. The LIVE/DEAD BacLight bacterial viability kit was obtained from Fisher Scientific (UK). Other reagents used in subsequent experiments will be introduced in the relevant

methodology sections. Unless otherwise specified, all reagents were obtained from Sigma-Aldrich (UK).

5.2.2 Modification of ZnO nanopillars

The samples used in this chapter consist of liquid-infused surfaces and superhydrophobic surfaces based on ZnO nanopillars (Chapter 3). The lubricant-infused surfaces of ZnO (LIS-ZnO) were prepared by infusing the ZnO nanopillars with silicone oil, as schematically shown in Figure 5.1. A drop-casting method was adopted in this process. Specifically, 5 μL of silicone oil was pipetted onto the nanopillar surfaces (1 cm × 1 cm) an Eppendorf Research Plus micropipette. Subsequently, the infused samples were tilted at 45° manually to allow the silicone oil to spread over the entire sample surface and kept overnight in a sealed container to remove excess lubricant from the surface.

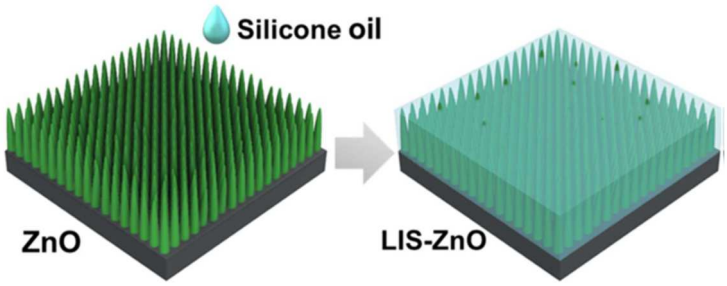

Figure 5.1. Schematic illustration of the preparation process of LIS-ZnO. ZnO nanopillar array is fabricated (left) and then silicone oil is applied, infusing the surface and resulting in a smooth, lubricant-coated LIS-ZnO (right).

The comparative superhydrophobic surfaces of ZnO (SHS-ZnO) were prepared by modifying the ZnO nanopillars with FAS. In this process, typically,10 μL of FAS was pipetted onto a glass slide next to the nanopillar samples in a vacuum chamber,

followed by sealing the chamber and activating the vacuum pump. After the 2-hour vacuum deposition at room temperature, the coated samples were removed from the chamber and placed in a clean, dry, sealed petri dish at ambient conditions for 8 hours to allow the FAS coating to cure.

5.2.3 Microscopy, wettability and stability

Surface morphology was observed using SEM and AFM. SEM images were taken using the Thermo Scientific TF Apreo 2S HiVac SEM at an acceleration voltage of 2.0-15.0 kV. Using different voltages for different sample types can yield clearer images. For example, low kV should be used when observing LIS-ZnO, which have high surface sensitivity. Before the analysis, a 6-nm platinum layer was coated on SHS-ZnO and LIS-ZnO by sputter deposition to aid imaging quality. According to the technicians' advice, platinum has a finer grain size, better conductivity, and lower charging compared to gold, which improves SEM imaging. To compare the changes in microscopic features, both bare zinc and ZnO nanopillar surfaces were also observed after being coated with the same platinum layer. The AFM (Cypher S AFM from Oxford Instruments) images were taken using the air tapping mode to minimize sample damage and artifacts while providing high-resolution imaging of the ZnO nanostructures, with a scan size of 1 × 1 μm^2 and a scan rate of 1.0 Hz to capture detailed surface morphology and obtain high-quality image results while maintaining fast imaging efficiency.

The thickness of the lubricant layer was determined by analysing AFM

force−distance measurements (air tapping force mode) characterised by 4 stages, as shown in Figure 5.2 [157]. Briefly, in stage i, the AFM cantilever remained undeflected prior to the tip contacting the surface. Once the tip of the cantilever was brought to contact the lubricant layer in stage ii, the capillary forces induced by lubricant wetting resulted in a downward pull on the cantilever. This was associated with a sudden negative dip in the force curve. The tip of the cantilever moved through the lubricant layer in stage iii until it contacted the substrate structure. In stage iv, further bending the cantilever led to a continuous positive deflection in the force curve results. The thickness of the lubricant layer was determined by calculating the difference between the snap-in point in stage ii and the hard contact point in stage iv. A total of 50 measurements were conducted, with each measurement taken at different locations on the sample to account for any variability in the lubricant layer. The shortest distance of the measurements was ascribed to the thickness of the lubricant on the nanopillar, while the longest distances were ascribed to the thickness of the lubricant between the nanopillar structure.

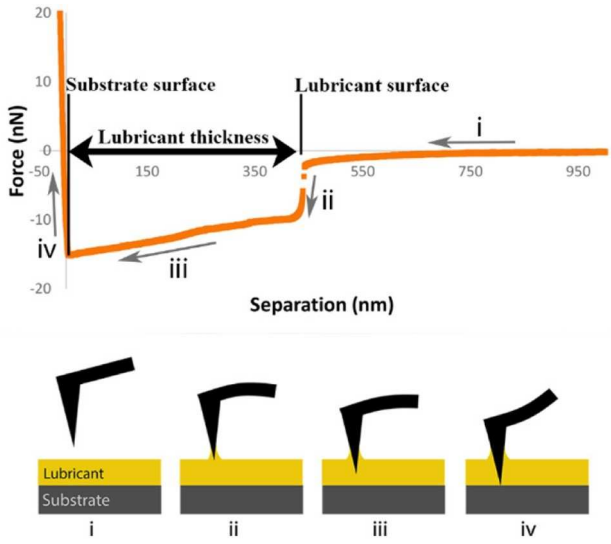

Figure 5.2. Schematic diagram of the meniscus force curve and the stages of contact between the AFM tip and the lubricant [157].

The wettability of the samples was evaluated using the same method mentioned in Chapter 4.2.3. The adhesion force of the droplet on the surface was then collected by the home brew device shown in Figure 5.3, where the volume of the droplet was 10 μL and the movement speed of the stage was 0.25 mm/s. This droplet volume was chosen to ensure a measurable and relevant contact area while avoiding excessive weight effects, and the stage speed was selected to minimize inertia effects and ensuring reliable force readings.

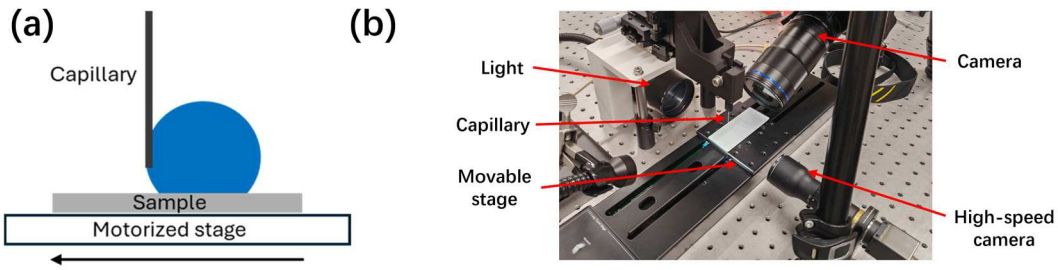

Figure 5.3. (a) Schematic illustration and (b) real set-up of the droplet friction measurement.

Further, the durability of the samples was assessed using the standard tape stripping test, which is commonly employed to evaluate the mechanical stability of lubricant-infused surfaces [158]. This method simulates external mechanical wear and helps determine the retention of the infused lubricant. To quantify the surface stability, the CA of the samples was measured after every 5 cycles of tape stripping. However, it is important to note that variations in applied force and adhesion strength of the tape may introduce minor inconsistencies in the measured CA values. In addition, the stability of LIS-ZnO was evaluated through a series of lubricant weight loss tests. Initially, the weight of the surface of ZnO nanopillars was recorded. After the infusion of silicone oil, one hundred water droplets of 10 μL were allowed to slide over the vertically placed sample of LIS-ZnO. The weight of the sample of LIS-ZnO was measured after the sliding of 25, 50, 75, and 100 droplets, respectively, to assess any loss of lubricant.

5.2.4 Photocatalytic performance

Two methods were used to observe, measure and compare the photocatalytic activities of the surfaces. Firstly, optical observations were performed by visual inspection and recorded using a digital camera to assess the degradation of a fluorescent dye, CF633, exposed to the surfaces. The CF633 dye was prepared in aqueous solutions (0.01 $mg \cdot mL^{-1}$) before use. 30-μL droplets of the aqueous CF633 were placed on the surfaces using pipette, which were then sealed in the same Petri dish with its lid to inhibit evaporation. Optical images of the droplets were recorded

using a Nikon Z7 II camera every 30 minutes for up to 5.5 hours under ordinary indoor conditions with a light intensity of 400 lux and a 2.5-meter distance between the light source and the samples. The 30-minute interval ensures that critical changes are captured, while the 5.5-hour total duration prevents results from being overly influenced by droplet evaporation. The experiments were repeated three times. In addition, a 5-hour spectroscopic analysis was carried out to quantify the degradation rate of fluorescence intensity using a BMG Labtech CLARIOstar Plus Plate Reader with a 12 well plate. The parameters for the fluorescence intensity mode were set to an excitation wavelength of 625 ± 10 nm and an emission wavelength of 650 ± 20 nm based on the characteristics of the CF633 dye. The lighting condition, number of tests and measurement intervals remained consistent with the optical observation. Furthermore, the diffuse reflectance spectroscopy (DRS) results of the ZnO nanopillars were collected to assess their light absorption efficiency and determine their optical bandgap energy, using a Shimadzu UV3600i spectrometer covering the wavelengths of 800 nm to 200 nm. This wavelength range was selected to fully capture ZnO's absorption edge in the UV, as well as its reflectance behaviour in the visible and near-infrared regions.

5.2.5 Anti-biofouling assay

5.2.5.1 Bacterial culture preparation

Overnight cultures of the bacteria *E. coli* and *Pss* were prepared before use. This was done by inoculating a colony of each bacterium to 5 mL of sterile Lysogeny Broth

(LB) (for *E. coli*) [159] or King's B broth (KB) (for *Pss*) [160]. The culture was incubated overnight at 37 °C (for *E. coli*) or 27 °C (for *Pss*), with continuous shaking at 180 rpm.

5.2.5.2 Anti-biofouling test

Three individual test samples for each type of surface were placed inside a single well of a 24-well sterile plate, onto which 500 µL of the bacterial suspension (optical density = 0.25 in fresh LB or KB media) was inoculated for 3- and 24-hour static incubations at 27°C for *Pss* or 37°C for *E. coli*. Tested surfaces were then collected and treated after incubation for bacteria cell observation under the confocal microscope and SEM. The treatment procedures are provided in the supporting information. To assess the bacterial CFU (mL^{-1}), a dilution series was prepared and plated to enable counting of single colonies. Each dilution was tested in triplicate (technical replicates). A cell well with no surface was included as a control to measure the growth of each bacterium in the absence of a potential antibacterial surface.

Samples for confocal microscopy were prepared using the incubated surfaces from the anti-biofouling test. Each sample was gently washed with 30 µL of PBS to ensure the removal of any residual medium. A staining solution was prepared by mixing the PBS with dyes from the LIVE/DEAD™ BacLight™ bacterial viability kit. Then 5 µL of the staining solution was pipetted onto the samples, followed by 15 minutes of storage in the dark. Bacterial viability analysis was then carried out by observing the signals using a Leica TCS SP8 confocal microscope (40×/1.40 oil objective). The parameters for the excitation were set to a wavelength of 488 nm and 561 nm based on the

characteristics of the dyes SYTO 9 (green signals, representing living cells) and propidium iodide (red signals, representing dead cells), respectively.

For SEM analysis, new samples of incubated surfaces following the anti-biofouling protocol were prepared. Each sample was fixed in 4% paraformaldehyde for 10 minutes, then incubated in a series of ethanol-PBS solutions with an increasing ethanol concentration (10, 30, 50, 70, 90 and 100%). Each concentration solution was applied for 10 minutes, except for the 100% solution which required a 20-minute incubation. Dried samples were sputter-coated a 6-nm platinum layer to aid imaging quality before the SEM analysis.

5.2.5.3 Bacterial attachment test

Aiming to evaluate the bacterial adhesion process to each of the surface types, an attachment experiment was performed [161]. Briefly, each type of surface was placed in a 24-well plate in triplicate. The surfaces were covered with 500 µL of *E. coli* or *Pss* bacterial suspension (optical density = 0.25) and incubated statically for 3 hours. Following incubation, the broth was removed, and the test surfaces were transferred to a new 24-well plate. The surfaces were rinsed twice with PBS to remove loosely attached bacteria. The quantity of bacteria present in the wash buffer was determined by serial dilution and plating, representing “weakly attached cells”. Subsequently, 1 mL of fresh PBS was added to each well, and the test surfaces were sonicated for 3 minutes at a frequency of 25 kHz. The obtained liquid was serially diluted and plated in triplicate in LB or KB agar. The viable colonies were counted using same agar

method as anti-biofouling test and denoted as the number of “adherent cells”.

5.3 Results and Discussions

5.3.1 Surface morphology and wettability

SEM and AFM analysis (Figure 5.4a and 5.4c) shows that arrays of vertically oriented nanopillars were grown on the zinc substrate after the hydrothermal process mentioned in Chapter 3. It was confirmed through the microscopic observation that the ZnO nanopillars had a diameter of approximately 70-80 nm, with a height mostly in the range of 280-530 nm (Figure 5.5). These closely arranged nanopillars, with their reasonably uniform pattern as confirmed by SEM image analysis (Figure 5.4a), where the average nanopillar spacing showed a low coefficient of variation. This arrangement provided adequate interstitial spaces for the immobilisation of the lubricant, as evidenced by stable lubricant retention observed in subsequent sliding angle tests. Upon infiltration, the nanopillar array presents a relatively flat lubricated surface, indicating that the interstitial spaces between the ordered nanopillars were filled with silicone oil (Figure 5.4b). The thickness of the silicone oil layer from the top of the nanopillar structure was estimated to be within approximately 20-25 nm, while the thickness of the lubricant layer infused between the nanopillars was on the order of 400-500 nm (Figure 5.4c, Figure 5.6 and Table 5.1). By contrast, the ZnO nanopillars modified with FAS show a random morphology on which no original nanostructure could be identified (Figure 5.7), due to the self-assembly of FAS molecules on the nanopillar structure [162].

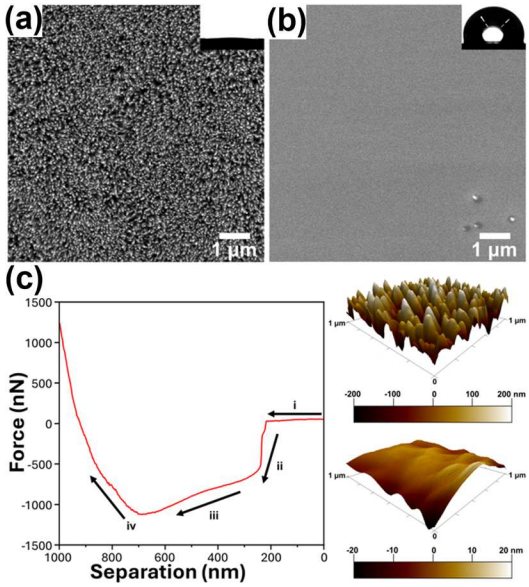

Figure 5.4. SEM images of (a) unmodified ZnO nanopillars and (b) LIS-ZnO. Insets of (a) and (b) show optical images of water droplets. (c) Representative AFM force-distance measurement to characterise the local thickness of the lubricant layer (400-500 nm), with the AFM height images revealing the topographies of ZnO nanopillars (top) and LIS-ZnO (bottom).

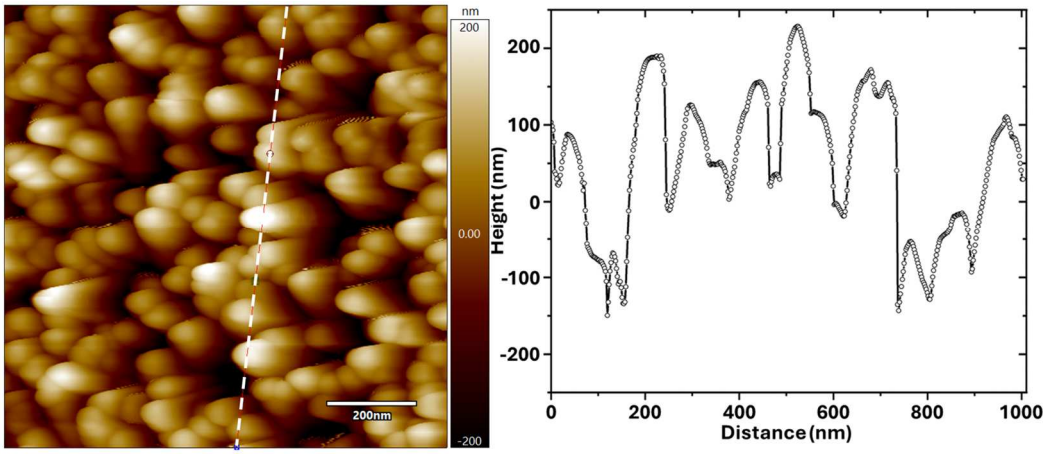

Figure 5.5. AFM image of ZnO nanopillars. The height of the nanopillars was mainly distributed between 280-530 nm with a typical diameter of 70-80 nm.

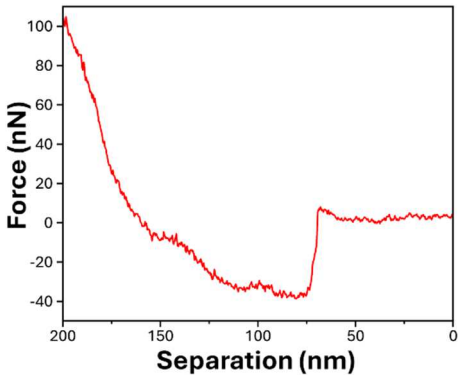

Figure 5.6. Thickness of lubricant layer from the top of nanopillars (approximately 20-25 nm).

Table 5.1. Measurements of lubricant layer thickness (from low to high, in nm)

No.	Thickness	**No.**	Thickness
1	18.8	**26**	240.8
2	21.3	**27**	306.8
3	22.3	**28**	362.6
4	24.1	**29**	368.7
5	24.7	**30**	371.9
6	24.8	**31**	373.6
7	25.3	**32**	375.3
8	26	**33**	376.8
9	27.6	**34**	379
10	27.7	**35**	418.4
11	29.2	**36**	425
12	42.2	**37**	426.3
13	90.9	**38**	430.7
14	119.7	**39**	430.7
15	136.6	**40**	438.7
16	139.6	**41**	439.9
17	143.4	**42**	440.4
18	149.5	**43**	448.5
19	170.3	**44**	451.2
20	176.1	**45**	454.8
21	180.6	**46**	457.1
22	183	**47**	458
23	185.4	**48**	458.3
24	199.5	**49**	462.3
25	221.9	**50**	462.7

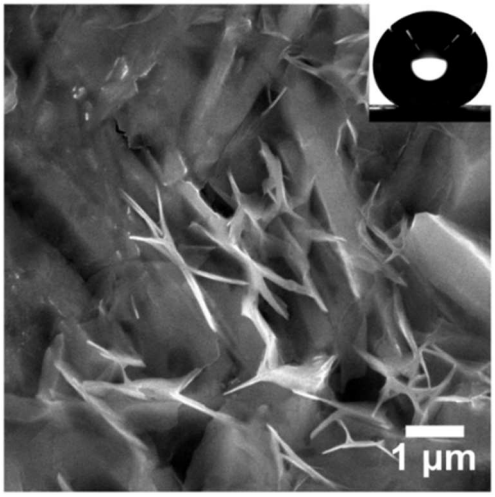

Figure 5.7. SEM image of the SHS-ZnO. The inset of image shows the optical image of a water droplet on the SHS-ZnO with measured contact angles of 155.9 ± 1.6°.

LIS-ZnO exhibited hydrophobicity due to the lubricant infusion, with an average CA of 105.5 ± 2.0°, while unmodified ZnO nanopillars showed superhydrophilicity characterised by a CA of 4.0 ± 0.5°. Meanwhile, no obvious adhesion was observed of the LIS-ZnO during the dynamic testing, where the CAH of water droplets on the lubricant-infused ZnO nanopillars was 2.0 ± 0.5°. Also, water droplets could smoothly slide down the LIS-ZnO at a sliding angle of around 2.1°. On the other hand, the SHS-ZnO exhibited superhydrophobic properties because of the low-surface-energy coating of FAS, with an average CA of 155.9 ± 1.6°. Generally speaking, the more coverage of the FAS coating, the larger the contact angles will be on the surface (Figure 5.8), until the roughness of the formed pattern becomes flattened by excessive coating [163].

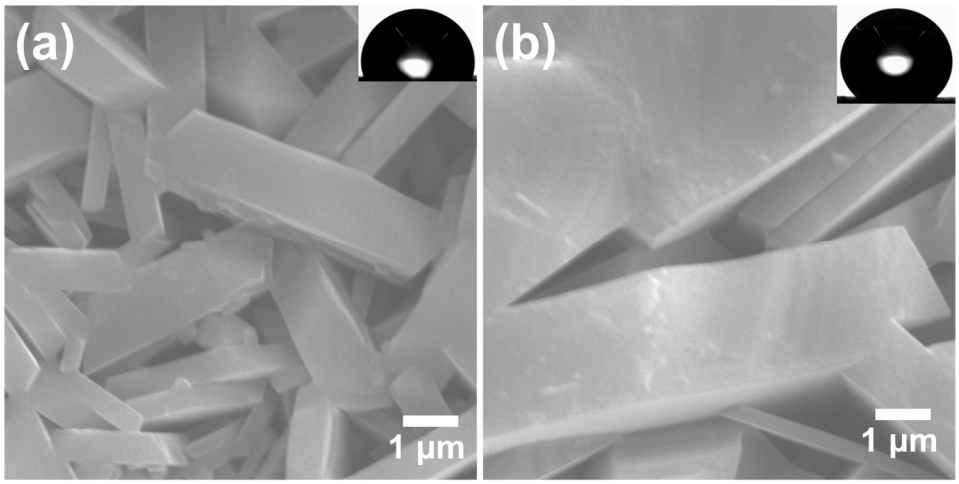

Figure 5.8. SEM images of the SHS-ZnO with FAS coating volume of (a) 5 μL and (b) 20 μL, respectively. The inset of the SEM image shows the optical image of a water droplet on each surface, with measured contact angles of 100.9 ± 2.1˚ and 140.4 ± 1.7˚, respectively.

Nevertheless, the CAH of the SHS-ZnO was 6.6 ± 1.5°, around three times as large as that of the LIS-ZnO. This is attributed to the irregular surface roughness on the FAS-coated SHS-ZnO that could cause more contact line pinning than the slippery LIS-ZnO [164], even if water droplets were still able to roll off the SHS-ZnO at a sliding angle of around 2.6°. The slipperiness of the LIS-ZnO can also be assessed by measuring the adhesion force of droplets. The results shown in Figure 5.9 illustrate three adhesion force measurements of droplets after they reached a steady motion using a home brew droplet friction measurement set-up, which indicate that droplets could move on the LIS-ZnO surface under a very small driving force (represented by the green line, Force = 4.6 μN).

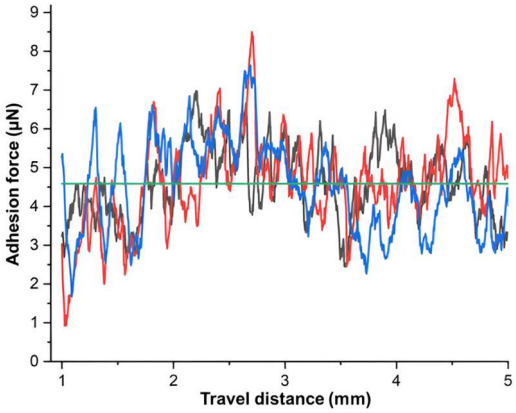

Figure 5.9. Adhesion force of a droplet moving on LIS-ZnO (n=3). The blue, red, and black lines represent the measured data, while the green line indicates the average adhesion force.

It should be noted that while wetting ridges surrounding the water droplets could be identified on LIS-ZnO because of the rise of the lubricant, they did not exhibit a prominent presence, as shown in Figure 5.10. This indicates that the infiltration of silicone oil had been induced via capillary rise infiltration into the interstitial spaces of ZnO nanopillar arrays [165]. As a result, the effectively retained lubricant on the nanopillar arrays imparts self-healing properties to the surface, thus contributing to its mechanical durability.

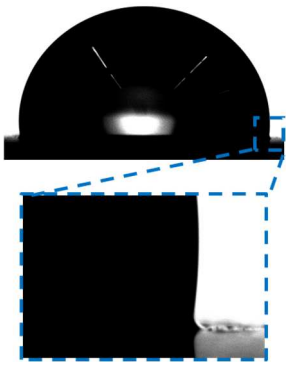

Figure 5.10. Water droplet on the LIS-ZnO. The area marked by the dashed line is magnified to indicate the wetting ridge.

Further, as shown in Figure 5.11, the CA remained stable on LIS-ZnO even after 30 tape-stripping cycles, showing a similar trend to other durability studies of LIS [45, 46]. The CAH of LIS-ZnO was also measured to examine the durability and wettability of the LIS-ZnO after being subject to tape stripping (Figure 5.12). Furthermore, even after 30 cycles, the lubricant layer remained observable under the SEM (Figure 5.13) and water droplets could still slide off the LIS-ZnO at a sliding angle of 5°, with a slower sliding speed compared to the pristine LIS-ZnO (Figure 5.11b). By contrast, the CA on SHS-ZnO decreased after each 5 times tape stripping, showing a rapid decline of superhydrophobicity, until the surfaces ultimately became hydrophilic. Notably, the SHS-ZnO gradually lost its superhydrophobicity over prolonged immersion in bacterial culture medium, as shown in Figure 5.14.

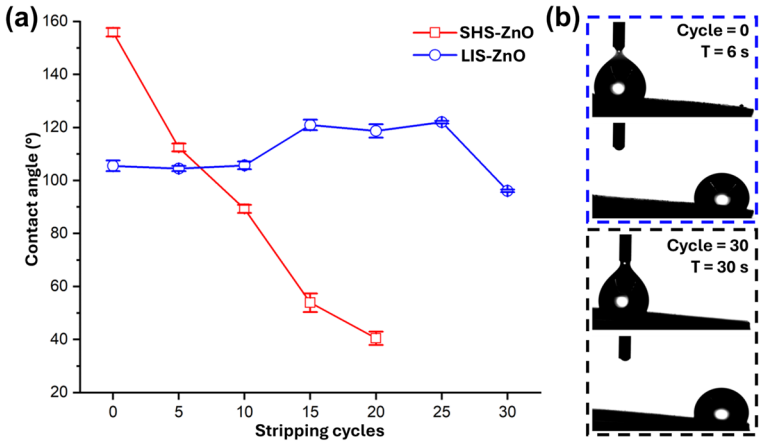

Figure 5.11. (a) The effect of tape stripping on the contact angles of water (5 μL) on SHS-ZnO and LIS-ZnO after tape stripping. (b) Droplet sliding on LIS-ZnO before and after 30 cycles of tape stripping. The angle of inclination is 5°.

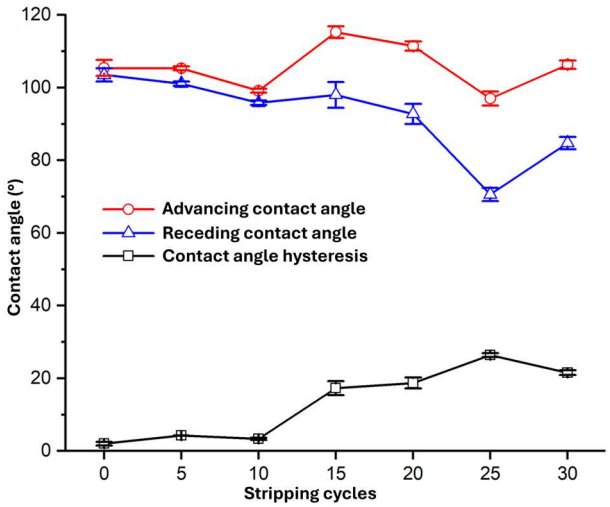

Figure 5.12. Advancing contact angle, receding contact angle and contact angle hysteresis of LIS-ZnO after every 5 cycles of tape stripping.

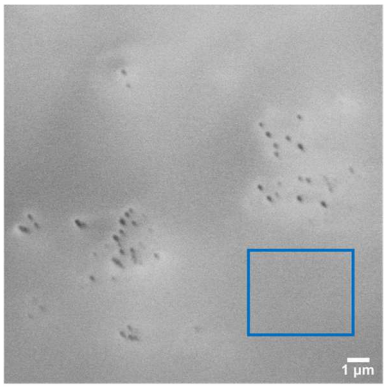

Figure 5.13. SEM image of LIS-ZnO after 30 tape-stripping cycles. The lubricant layer remained observable (the blue frame area as example).

Figure 5.14. Water droplets on SHS-ZnO after the (i) 3-hour and (ii) 24-hour immersion in bacterial culture medium with contact angles being 61.5 ± 3.7˚ and 19.7 ± 0.5˚ respectively.

In addition, the daily CA of LIS-ZnO under ambient conditions was measured over

9 days (Figure 5.15), showing that the exposed LIS-ZnO could still maintain their hydrophobicity. The contrast between LIS-ZnO and SHS-ZnO implies that the lubricant-infused ZnO nanopillar arrays acquired self-healing properties, where silicone oil infiltrated the structures so that droplet spreading and contact line pinning did not prevail as they would on the superhydrophobic surfaces [166]. Indeed, the CA of SHS-ZnO decreased approximately 15 degrees within 9 days of measurement, exhibiting a severe deterioration. Additionally, the loss of infused lubricant due to water droplet sliding was evaluated by measuring the change in sample weight before and after the sliding process using a weighing scale. As shown in Table 5.2 and Figure 5.16, the surface of LIS-ZnO retained approximately 61.7% of the lubricant after the passage of one hundred 10-μL droplets. To further investigate the impact of lubricant depletion on surface wettability, the water contact angle (CA) of LIS-ZnO was monitored every 20 droplet passages, up to a total of 200 droplets. Initially, the CA was 105.5 ± 2.0°, decreasing slightly to 102.2 ± 1.3° after 100 droplets, and further to 101.6 ± 1.2° after 120 droplets. It then remained stable in magnitude until the end of the test, as shown in Figure 5.17. This moderate reduction (approximately 5°) suggests that although some lubricant was inevitably lost or redistributed during droplet sliding, a stable equilibrium could be established once excess lubricant had been removed.

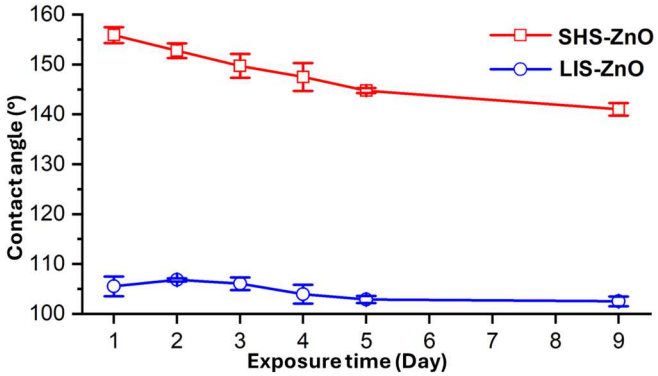

Figure 5.15. Static contact angles on SHS-ZnO and LIS-ZnO as a function of time (in days, n=9).

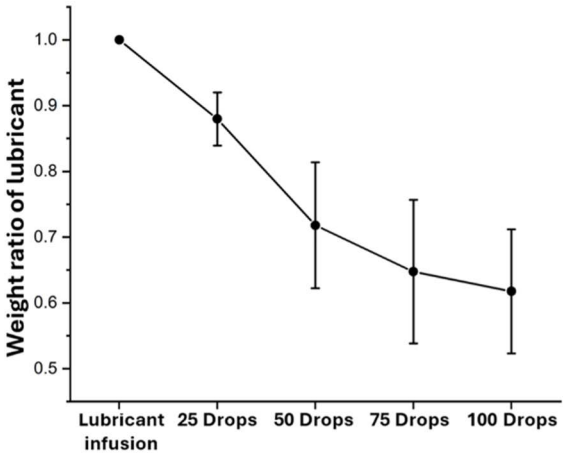

Figure 5.16. Retention of the lubricant in percentage during water droplet sliding tests (n=9).

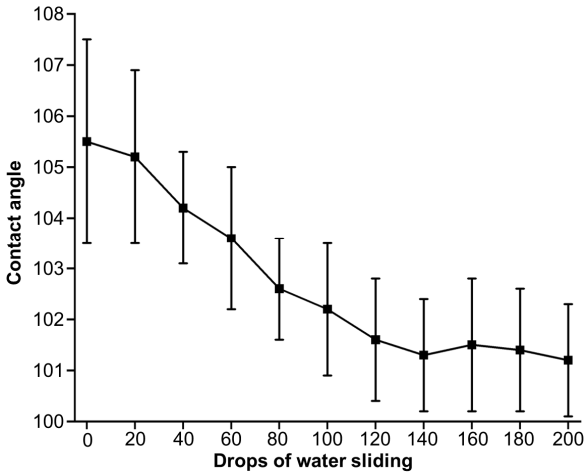

Figure 5.17. Static contact angles on LIS-ZnO during water droplet sliding tests (n=9).

Table 5.2. Retention of the lubricant during water droplet sliding tests

Sample 1	Sample weight (g)	Lubricant weight (g)	Lubricant weight ratio
Initial state	0.448	0	-
Lubricant infusion	0.4519	0.0039	1.00
25 drops	0.4514	0.0034	0.87
50 drops	0.4507	0.0027	0.69
75 drops	0.4505	0.0025	0.64
100 drops	0.4504	0.0024	0.62
Sample 2	Sample weight	lubricant weight	Lubricant weight ratio
Initial state	0.477	0	-
Lubricant infusion	0.4791	0.0021	1.00
25 drops	0.4788	0.0018	0.86
50 drops	0.4783	0.0013	0.62
75 drops	0.4781	0.0011	0.52
100 drops	0.4781	0.0011	0.52
Sample 3	Sample weight	lubricant weight	Lubricant weight ratio
Initial state	0.4209	0	-
Lubricant infusion	0.4233	0.0024	1.00
25 drops	0.4229	0.002	0.83
50 drops	0.4226	0.0017	0.71
75 drops	0.4225	0.0016	0.67
100 drops	0.4223	0.0014	0.58
Sample 4	Sample weight	lubricant weight	Lubricant weight ratio
Initial state	0.4564	0	-
Lubricant infusion	0.4603	0.0039	1.00
25 drops	0.4599	0.0035	0.90
50 drops	0.4591	0.0027	0.69
75 drops	0.4587	0.0023	0.59
100 drops	0.4587	0.0023	0.59
Sample 5	Sample weight	lubricant weight	Lubricant weight ratio
Initial state	0.4682	0	-
Lubricant infusion	0.4731	0.0049	1.00
25 drops	0.4728	0.0046	0.94
50 drops	0.4725	0.0043	0.88
75 drops	0.4722	0.004	0.82
100 drops	0.472	0.0038	0.78

5.3.2 Surface characteristics and photocatalysis performance

The degradation of the fluorescent dye, CF633, demonstrated that the lubricant-infused surfaces of ZnO nanopillars could cause organic compounds to degrade without requiring intense UV light, owing to the inherent photocatalytic activities of ZnO. As shown in Figure 5.18a, after less than 3 hours, the colour of the CF633-loaded droplet on the unmodified ZnO nanopillars almost entirely disappeared, indicating a substantial degradation of the fluorescent dyes under ambient light. Specifically, the electrons in the valence band of the ZnO nanopillars could be excited upon illumination. The empty electron holes (h^+) subsequently reacted with water to form hydroxyl radicals, which then resulted in the oxidation of the fluorescent dye [120, 167]. The performance of the unmodified ZnO nanopillars was immediately followed by the LIS-ZnO, which resulted in intensive discolouration of the dyed droplet after 3 hours. Further, the dyed droplet became entirely colourless after another 2.5 hours. At the end of the discolouration process, the droplet only slightly spread on the LIS-ZnO (after around 5 - 5.5 hours), indicating that the wettability of the surface was largely preserved throughout the degradation of the organic compounds (Figure 5.19). It should also be noted that the photocatalytic activities exhibited by the LIS-ZnO were more efficient than the SHS-ZnO and the bare zinc substrates. To be more specific, there were no obvious changes in the appearances of the dyed droplet on the bare zinc within 3 hours. For the SHS-ZnO, the excessive roughness and thickness of the FAS coating hindered the formation and effectiveness of the radicals, slowing the photocatalysis in

comparison with the LIS-ZnO [156]. This effect may be attributed to the FAS layer acting as a barrier, reducing contact and reaction between the reactive species and the dye droplet, as well as potentially covering the light, thereby limiting photocatalytic behaviour.

Furthermore, as shown in Figure 5.18b, the quantitative characterisation (via the microplate reader) of photodegradation of the fluorescent dye, CF633, as a function of fluorescence intensity was consistent with the trend of optical observations. The unmodified ZnO nanopillars exhibited the highest photocatalytic activity, achieving an almost 100% reduction in fluorescence intensity after 2.5 hours of photodegradation. In comparison, SHS-ZnO and LIS-ZnO showed fluorescence intensity reductions of 44% and 65%, respectively, over the same period. Notably, the fluorescence intensity of LIS-ZnO decreased by 99% after 5 hours, demonstrating its effective photocatalytic properties, whereas SHS-ZnO exhibited only a 63% reduction by the end of the 5-hour test. It was also observed that the fluorescence intensity of the droplet on bare zinc began to drop considerably after 4 hours of photodegradation, eventually matching that of the SHS-ZnO.

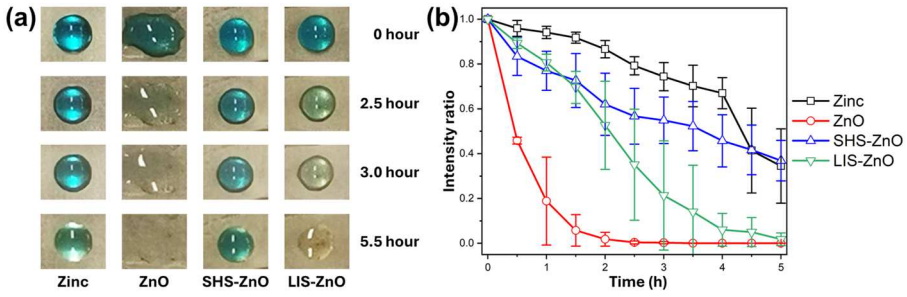

Figure 5.18. (a) Degradation of CF633-loaded droplets on various surfaces (n=9). (b) Fluorescence intensity changes of CF633 (n=9).

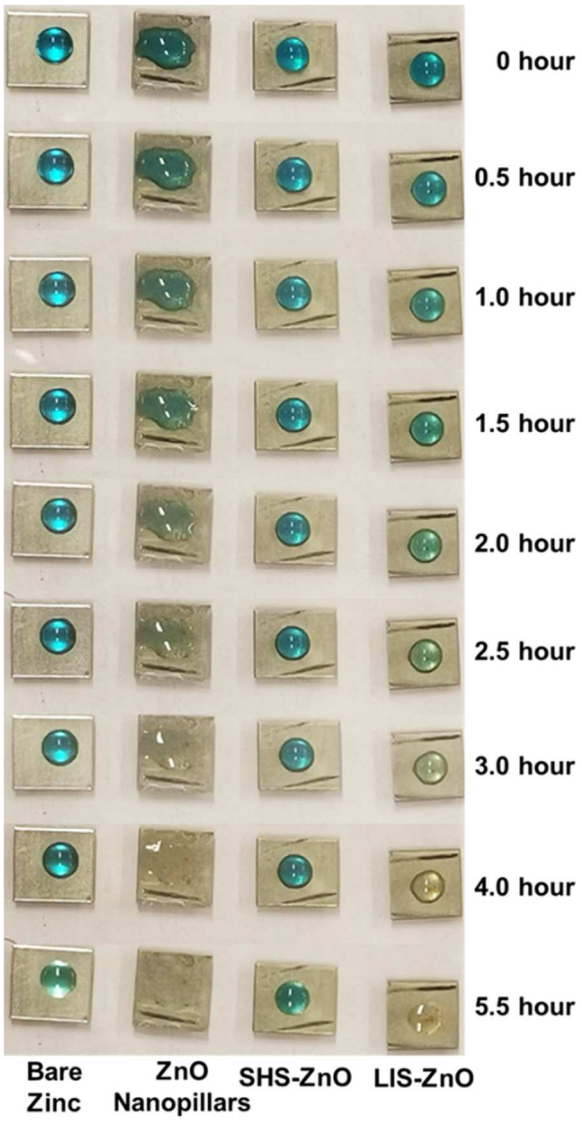

Figure 5.19. Decolorization of droplets on different surfaces during photocatalysis on full timeline.

To further confirm the photocatalytic properties of the prepared samples under visible light, the diffuse reflectance of the ZnO nanopillars was also measured in the wavelength range of 200–800 nm. The diffuse reflectance measurement results of ZnO nanopillars (Figure 5.20) provided the reflectance (R) of the samples to the incident light. The absorption spectrums of the ZnO nanopillars sample were subsequently

obtained using the Kubelka–Munk (K–M) function. The maximum absorbance of the ZnO nanopillars was observed in the violet region of visible light (380-450 nm), reaching approximately 11%. The absorbance rate then decreased and maintained at around 2.5%.

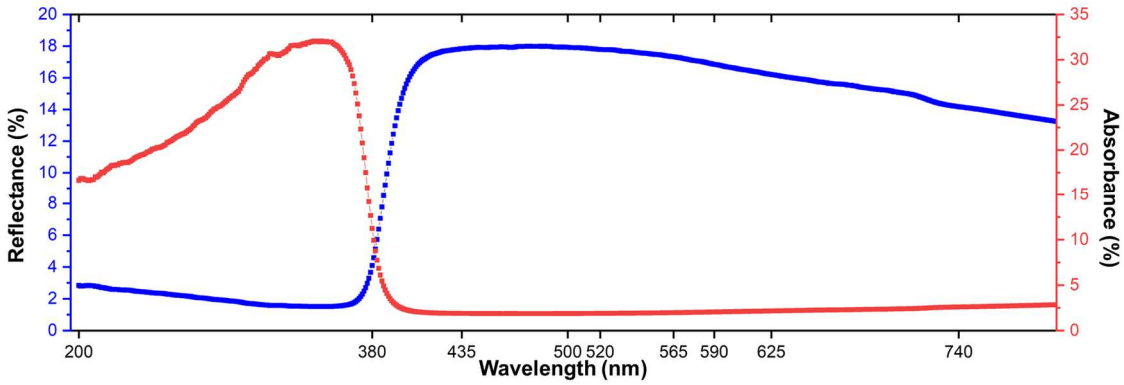

Figure 5.20. Diffuse reflectance spectra of the ZnO nanopillars. The blue curve depicts the relationship between the reflectance percentage and the wavelength, and the red curve shows the absorption spectrum.

The optical bandgap energy E_g of ZnO nanopillars was determined using the Kubelka-Munk function:

$$X - \text{axis} = h * \gamma$$

$$Y - \text{axis} = (F(R) * h * \gamma)^n$$

$$F(R) = \frac{(1-R)^2}{2R}$$

where h represents Planck's constant, v denotes the frequency of the light, R refers to the sample reflectance and n is an exponent which equals 2 in this study since ZnO is a direct bandgap material. The bandgap energy E_g of fabricated ZnO nanopillars was determined by extrapolating the fitted line to the point where it intersects the horizontal

axis (where Y=0). The corresponding photon energy at this intersection represents the bandgap energy. The calculated optical bandgap energy of the ZnO nanopillars was shown in Figure 5.21, to be about 3.25 eV, which is smaller than that of bulk ZnO (3.37 eV) [168]. This was attributed to the relatively large specific surface area of the nanomaterial. Particularly, the ZnO nanopillars were characterised by their high aspect ratio in comparison with bulk ZnO, consistent to the reported correlation of improved photocatalytic activities with high-surface-area ZnO nanocrystals [167, 169]. The improved photocatalytic activity allowed the ZnO nanopillars to perform photocatalytic reactions under visible lights, with the generation of ROS during this process rendering the bactericidal properties to the samples [170]. Notably, the ROS radicals of superoxide (O_2^-) have been ascribed to the antibacterial activity of ZnO nanomaterials under the dark condition [171, 172], indicating that ZnO nanostructures could maintain inherent bactericidal properties in various lighting conditions.

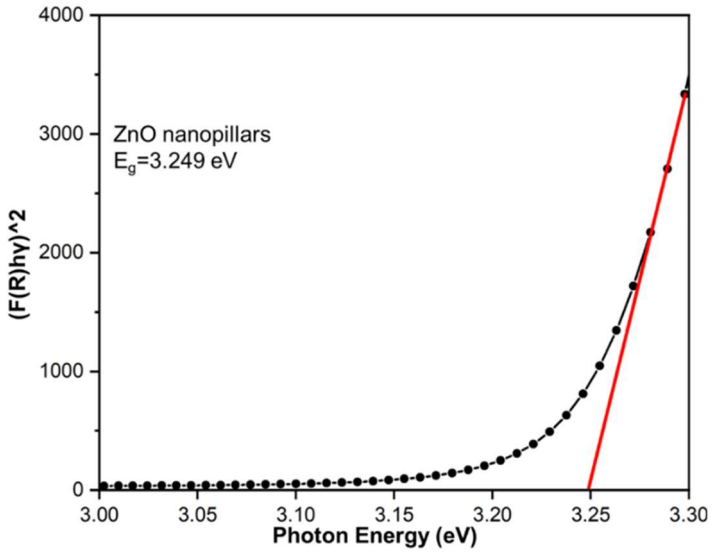

Figure 5.21. Optical bandgap of the ZnO nanopillars.

5.3.3 Anti-biofouling performance

The anti-biofouling effect of the surfaces was studied by firstly assessing the LIVE/DEAD staining results that differentiated live and dead cells using membrane integrity as a proxy for cell viability [173, 174]. Figure 5.22a shows the LIVE/DEAD stained *E. coli* bacteria after 24 hours of incubation on (i) bare zinc, (ii) unmodified ZnO nanopillars, (iii) SHS-ZnO and (iv) LIS-ZnO, respectively. There is a remarkable difference in the viability of *E. coli* populations between the bare zinc and the ZnO-based surfaces. On the one hand, *E. coli* maintained their viability on the bare zinc surfaces, where almost 100% amount of green-signalled cells could be observed. On the other hand, the *E. coli* bacteria on the unmodified ZnO nanopillars exhibited a near-complete reduction in viability, as evidenced by the extensive red signals, which indicate membrane disorganization and bacterial death. SHS-ZnO also exhibited bactericidal properties, though less pronounced than unmodified ZnO, as indicated by the confocal images, where some remaining bacterial cells still emitted green signals alongside the predominant red fluorescence. Additionally, a decrease in the number and intensity of fluorescence signals was observed of SHS-ZnO compared to bare zinc and ZnO nanopillars. One could identify distinct green fluorescence intertwined with the red fluorescence, implying there were viable bacterial populations on the SHS-ZnO even after 24 hours of incubation. However, on LIS-ZnO, the fluorescence signals were substantially reduced by comparison, and only red fluorescence was detected, signifying the complete absence of viable bacteria and confirming its bactericidal effect.

The bacterial viability was further assessed through microscopic examination of bacterial morphologies on the surfaces. Figure 5.22b shows SEM images detailing the morphologies of *E. coli* bacteria in contact with different samples. The rod-shaped morphology of *E. coli* was retained on bare zinc surfaces. However, the *E. coli* bacteria on unmodified ZnO nanopillars and SHS-ZnO exhibited abnormal shapes resulting from disorganised membranes. These morphological damages that led to bacterial death were consistent with the results observed under confocal microscopy. However, it is interesting to note that no full-sized bacteria were distinguished on LIS-ZnO under SEM. There were only nano-sized fragments resembling bacterial silhouettes or remnants, implying membrane disorganisation that led to the release of bacterial components into the lubricant layer on the LIS-ZnO after the incubation [175]. This corroborated the confocal microscopy results that showed moderate fluorescence signals on the LIS-ZnO, which suggested the loss of viability of the *E. coli* bacteria.

To investigate the onset of the bactericidal properties, tests with a short incubation of 3 hours were also conducted on the different samples. As shown in Figure 5.22c, the coverage of the bacteria on the surfaces after the short incubation was reduced by more than 70% compared with that after the 24-hour incubation. It is presumed that the short incubation did not facilitate enough time for the bacteria to attach to the surfaces, especially the SHS-ZnO and LIS-ZnO that featured low interfacial properties. A small portion of the *E. coli* bacteria started to appear red on the ZnO nanopillar-based surfaces, but the majority of the bacteria remained viable. It is deduced that the ZnO

nanopillars did not exhibit adequate bactericidal activity within the 3-hour incubation period, likely because the concentration of ROS acting on the bacteria and the duration of interaction with the bacterial cell membranes had not yet reached effective levels [176, 177]. For this reason, as shown in Figure 5.22d, the morphology of the *E. coli* bacteria remained rod-shaped without any noticeable membrane disorganisation on the bare zinc, unmodified ZnO nanopillars and SHS-ZnO. For the LIS-ZnO of the 3-hour incubation, the appearance was similar to that of the 24-hour incubation. However, the structures that resembled the silhouette of the *E. coli* bacteria were less in quantity, because of the decrease in the quantity of the attached bacteria on the LIS-ZnO.

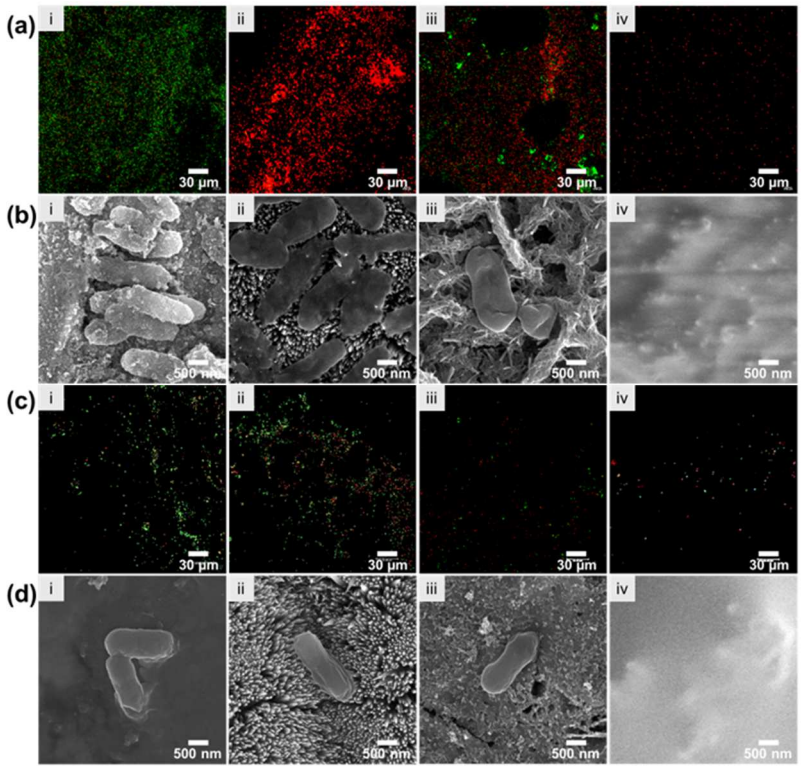

Figure 5.22. (a, c) Confocal microscopy and (b, d) SEM images of *E. coli* after (a, b) 24- and (c, d) 3-hour of incubation on (i) bare zinc, (ii) ZnO nanopillars, (iii) SHS-ZnO and (iv) LIS-ZnO.

Microscopic assessments were also conducted for *Pss*, which has a different biofilm formation mechanism to *E. coli*. Compared to *E. coli* biofilms, which are primarily composed of proteinaceous curli fimbriae and cellulose, those formed by *Pss* exhibited stronger resistance to removal [178]. This is likely because *Pss* produces *alginate exopolysaccharide*, which contributes to a robust extracellular matrix. Additionally, the presence of type IV pili, which, aids in initial attachment and biofilm formation through 'twitching motility', a process where the bacteria use pili extension to attach to surfaces, followed by retraction to facilitate movement [179]. The confocal microscopy images of LIVE/DEAD-stained *Pss* after 24 hours of incubation on bare zinc, unmodified ZnO nanopillars, SHS-ZnO and LIS-ZnO are shown in Figure 5.23a. It can be observed that *Pss* bacterial cells remained alive on the bare zinc surface. SEM results (Figure 5.23b) further demonstrated that the *Pss* bacteria on bare zinc maintained their normal morphology and showed a tendency for biofilm formation. Conversely, nearly all *Pss* bacteria exhibited red signals when they were exposed to unmodified ZnO nanopillars, SHS-ZnO and LIS-ZnO. Structural damage of the *Pss* bacteria on the unmodified ZnO and SHS-ZnO, to different extents, was revealed by SEM images (Figure 5.23b). Particularly noteworthy is the lower bacterial coverage on LIS-ZnO compared to the other surfaces, which suffered from the accumulations of intact and/or damaged bacteria. Hence, antibacterial effect and low adhesion property had been consistently facilitated by the LIS-ZnO for both *Pss* and *E. coli*, despite their difference in bacterial components and biofilm formation modes. When the length of

the incubation was decreased to 3 hours, *Pss*, similar to *E. coli*, could partly survive on SHS-ZnO and LIS-ZnO (Figure 5.23c-d), implying that the 3-hour interaction was not long enough for these surfaces to generate thorough antibacterial effect. It should nevertheless be noted that the coverage of *Pss* on the slippery LIS-ZnO was less than on the SHS-ZnO, and the least among all the surfaces.

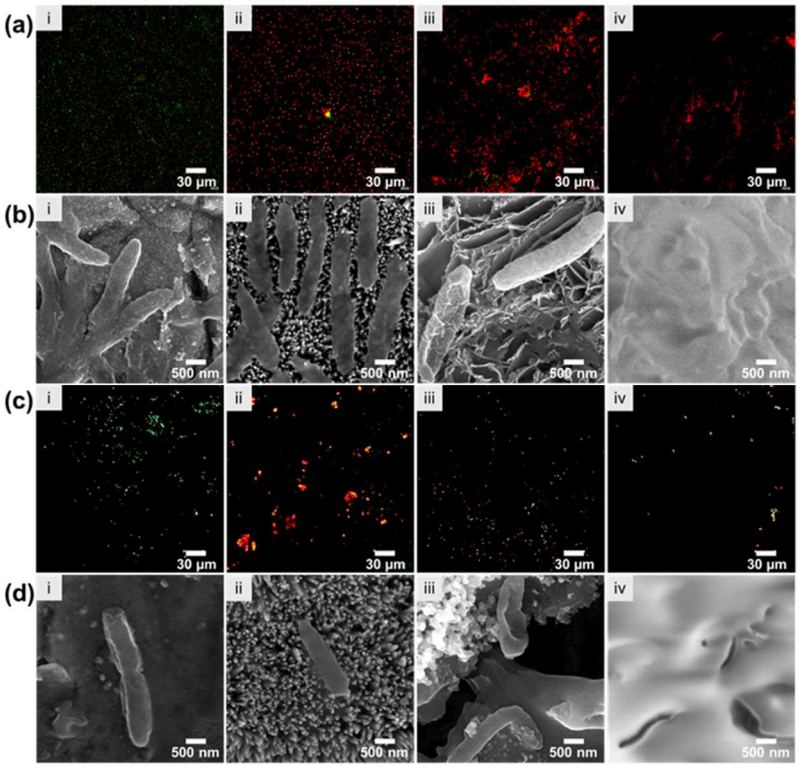

Figure 5.23. (a, c) Confocal microscopy and (b, d) SEM images of Pss after (a, b) 24- and (c, d) 3-hour of incubation on (i) bare zinc, (ii) ZnO nanopillars, (iii) SHS-ZnO and (iv) LIS-ZnO.

The antibacterial property of ZnO materials is mainly attributed to the generation of ROS by photocatalysis, which have a strong oxidising ability to damage cell membranes, leading to the bacterial inactivation [120]. This is why both *E. coli* and *Pss* appeared to be largely killed after 24 h of incubation (and partly killed after 3 hours) on

the unmodified ZnO nanopillars, as illustrated by the microscopic studies. On top of the effect of ROS, the nanopillar structure could also pierce the cell wall and cause further damage to the bacteria [180-182]. However, the high adhesion of unmodified ZnO nanopillars, which was reflected by the low contact angles and extreme contact angle hysteresis, made it easy for bacteria to build up their coverage, reducing the anti-biofouling properties over time, as shown in Figure 5.24. The slippery LIS-ZnO had slower photocatalytic activities than the unmodified ZnO nanopillars due to the presence of the lubricant layer, but the low interfacial adhesion prevented bacterial buildup. It should be further noted that the low adhesion property of the LIS-ZnO was an advantage over the SHS-ZnO, of which the FAS coating also caused uncertainties in the bactericidal activities of the ROS within the relatively short incubation period.

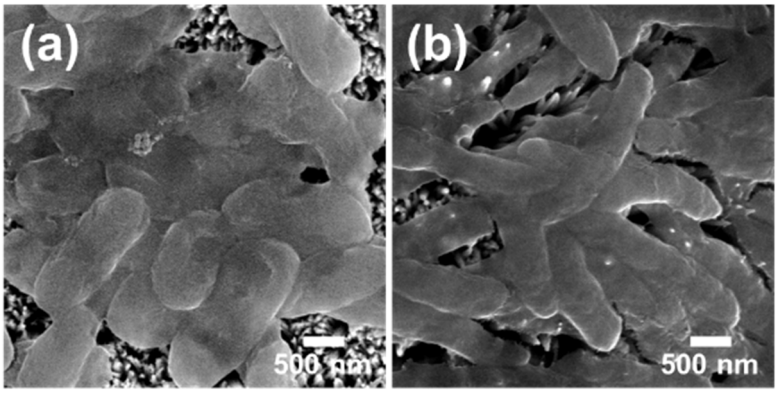

Figure 5.24. (a) *E. coli* and (b) *Pss* build up on ZnO nanopillars.

The anti-biofouling performance on different surfaces was also quantitatively demonstrated in terms of CFU, as shown in Figure 5.25. After 24 h of incubation, the number of live *E. coli* decreased on ZnO nanopillar-based surfaces by nearly three orders of magnitude compared to that of the control group (Figure 5.25a). In particular,

the CFU of *E. coli* on the LIS-ZnO was slightly less in quantity than that on the unmodified ZnO nanopillars. This is attributed to the low adhesion property of the LIS-ZnO, which minimised the bacterial build-up that could undercut the bactericidal effect of unmodified ZnO nanopillars. Similarly, exposure to *Pss* also revealed that LIS-ZnO exhibited the greatest bactericidal effect among all nanopillar-based surfaces, resulting in a reduction of viable bacteria by nearly four orders of magnitude compared to the control group, as shown in Figure 5.25b. It is also worth noting that the CFUs of *E. coli* and *Pss* on LIS-ZnO surfaces were reduced by approximately 70% and 35%, respectively, relative to SHS-ZnO surfaces. In addition, the results of CFU after 3 hours of incubation on the surfaces were also compared (Figure 5.25c-d). It was revealed that, in comparison with the 24-hour incubation that spanned up to 4 orders of magnitude, there was a rather limited decrease (up to about 1 order of magnitude) in the number of viable bacteria on the nanopillar-based surfaces relative to the control group after the short incubation. This explains the uncertainties in the pattern and viability of the *E. coli* and *Pss* bacteria on these surfaces illustrated by the above-discussed microscopic assessments (Figure 5.22c-d and Figure 5.23c-d).

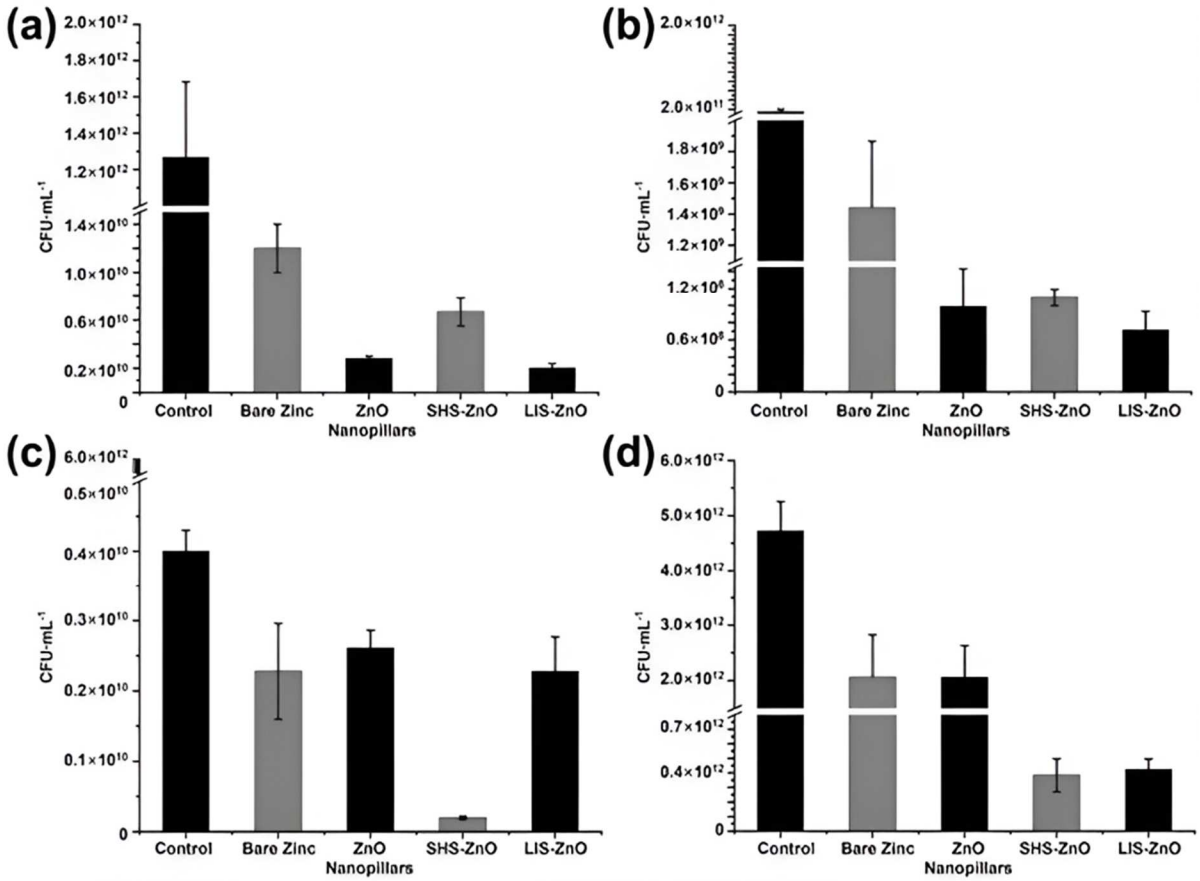

Figure 5.25. The number of colony forming units (CFU)/mL of (a, c) *E. coli* and (b, d) *Pss* on each surface after different incubation lengths: (a, b) 24 hours and (c, d) 3 hours (n=27).

Figure 5.26 illustrates the quantities of bacteria attached to various samples as a function of CFU counts after 3 hours of incubation under two cleaning conditions. Initially, all samples were rinsed twice with PBS solution to remove loosely or weakly attached bacteria, and the recovered PBS solutions were used to quantify these bacteria. The remaining strongly adherent bacteria were then removed through sonication for further quantification. Figure 5.26a presents the adhesion results for *E. coli* after 3 hours of incubation. It is evident that *E. coli* attachment follows a consistent

trend across all surfaces, where the CFU of weakly attached bacteria is significantly higher than that of strongly adhered bacteria. This indicates that *E. coli* was unable to form a persistent biofilm within this time frame. Furthermore, the CFU values for SHS-ZnO and LIS-ZnO are notably lower than those of other surfaces, highlighting their anti-attachment properties. It is also noteworthy that although unmodified ZnO nanopillars exhibit low bacterial attachment, this is attributed to their bactericidal effect (Figure 5.22cii and Figure 5.23cii), which leads to bacterial death and subsequently reduces the CFU detected.

Similarly, SHS-ZnO and LIS-ZnO exhibited resistance to bacterial attachment in the case of *Pss*, as shown in Figure 5.26b. However, unlike *E. coli*, *Pss* adhesion follows a different pattern. On most surfaces, the CFU of strongly adherent *Pss* was higher than that of weakly attached bacteria, except for LIS-ZnO. This can be attributed to *Pss* possessing type IV pili, which enable it to adhere more firmly to surfaces than *E. coli*. Additionally, *Pss* produces *alginate exopolysaccharides* during biofilm formation, further reinforcing its attachment. In contrast, on LIS-ZnO, the CFU of weakly attached *Pss* was greater than that of strongly adhered bacteria, indicating that LIS-ZnO effectively maintains its anti-attachment behaviour even against robust biofilm-forming bacteria.

Quantitatively, compared to the control group, LIS-ZnO reduced the weakly attached *E. coli* and *Pss* by 99.3% and 99.9%, respectively. The CFU of strongly adherent bacteria on LIS-ZnO was also significantly lower, with reductions of 94.1%

for *E. coli* and 99.9% for *Pss*. Notably, the strongly adherent bacteria on LIS-ZnO were fewer than those on SHS-ZnO, which is attributed to the low interfacial adhesion of LIS-ZnO, characterized by its low contact angle hysteresis compared to SHS-ZnO. By contrast, the attachment of bacteria onto the LIS-ZnO tended to be relatively loose, because of the low interfacial adhesion property, in comparison to the SHS-ZnO. As a result, the magnitude of CFU for loosely attached bacteria that were removed from the LIS-ZnO was greater than that from the SHS-ZnO. This further corroborates the microscopic observations, which show that LIS-ZnO prevents both *E. coli* and *Pss* from forming biofilms. Overall, these results demonstrate that while both LIS-ZnO and SHS-ZnO exhibit bacterial anti-attachment properties, LIS-ZnO is particularly effective due to its ability to minimize interfacial adhesion, even against more resilient biofilm-forming bacteria like *Pss*.

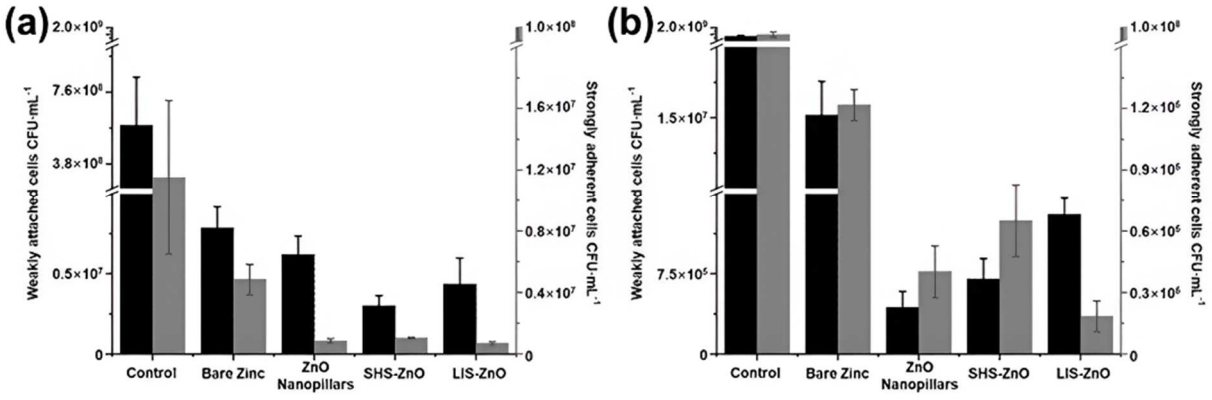

Figure 5.26. The attachment of (a) *E. coli* and (b) *Pss* as a function of CFU on each sample after washing. The length of incubation was 3 hours (n=9). Black bars represent weakly attached cells, while the grey bars represent the strongly adherent cells.

5.4 Conclusions

In conclusion, lubricant-infused ZnO nanopillars have shown anti-biofouling activities and low-adhesion properties. These surfaces were fabricated by infiltrating silicone oil into the interstitial spaces of ZnO nanopillar arrays. The infusion of the lubricant changed the wettability and adhesion property of the nanopillar arrays, resulting in a slippery surface that was characterised by a minimum contact angle hysteresis of 1.5 degrees. Remarkably, the resultant LIS-ZnO from capillary rise infiltration could survive 30 cycles of tape stripping test to retain the slippery properties. Meanwhile, these surfaces retained the photocatalytic activities of the underlying ZnO nanopillars, which can generate ROS to oxidise and degrade organic compounds. This allowed the LIS-ZnO to be more effective at both killing *E. coli* and *Pss* and reducing bacterial attachment than their superhydrophobic counterparts coated with fluoroalkylsilane. Hence, by combining the slippery property and inherent bactericidal property, the LIS-ZnO was endowed with a dual function to tackle biofouling. The simple fabrication, robustness and effective antibiofouling performances make the LIS-ZnO promising for various applications. There is an envision that future research will benefit from enhancing the photocatalytic activities of the lubricant-infused surfaces and the pattern of the underneath ZnO nanopillars. This will generate a twofold improvement in the antimicrobial performances and the durability of the LIS-ZnO.

CHAPTER 6 CONCLUSIONS AND FUTURE WORKS

Although a lot of research has been conducted on the development of surfaces possessing both antibacterial and water-repellent properties, major challenges are still being encountered in achieving long-term stability and sustained anti-biofouling effects under actual environmental conditions. In particular, antibacterial surfaces prepared by traditional methods have often been found to have difficulty maintaining stable performance over extended periods without the reliance on additional chemical bactericides. For example, it was found in our research that although good antibacterial properties were exhibited by traditional ZnO nanostructures, their durability was significantly limited in practical use environments, as they were covered by dead bacteria, which in turn affected their subsequent bactericidal properties. In addition, surfaces treated by commonly used water-repellent methods, such as superhydrophobic surfaces and lubricant-infused surfaces, although significant water-repellent and anti-biofouling capabilities were shown, have been observed to possess poor long-term effectiveness due to the lack of inherent antibacterial properties, thereby necessitating the use of additional antibacterial agents to achieve bactericidal functions. It is thereby indicated that the development of hybrid surfaces with both inherent antibacterial and water-repellent properties is of great research value.

To address these limitations, a biomimetic ZnO nanopillar surface was first prepared by optimizing the hydrothermal synthesis reaction process, which was inspired by cicada wings and resulted in uniform array of nanopillars. Subsequently, a

new type of superhydrophobic surface was successfully developed based on the structural surface. It was achieved that the sufficiently thin PDMS-coated ZnO nanopillar array reached the Cassie-Baxter wetting state, by which bacterial adhesion was significantly reduced due to the minimization of solid-liquid contact. At the same time, effective bactericidal performance against both gram-positive and gram-negative bacteria was achieved by the inherent photocatalytic activity of the ZnO nanopillars, without the addition of chemical agents, thereby overcoming the key limitations of traditional superhydrophobic or lubricant-infused surfaces.

In addition, a complementary approach was provided by the combination of lubricant-infused treatment and ZnO nanopillar arrays, which utilized both physical repulsion and photocatalytic bactericidal effects. It was demonstrated by systematic evaluation that the lubricant-infused ZnO nanopillar surface exhibited strong resistance to gram-negative bacteria with different biofilm formation mechanisms and stability under dynamic conditions. A new precedent for anti-biofouling surfaces was thereby set by this combined approach, and the feasibility of incorporating intrinsic bactericidal functions into lubricant-injected surface structures was demonstrated.

Overall, the research objectives of fabricating and studying the water repellency and antibiofouling applications of surfaces based on ZnO nanopillar structures have been achieved. Based on the results of this thesis, both ZnO nanopillar-based superhydrophobic and lubricant-infused surfaces can exhibit excellent antibiofouling properties compared to untreated zinc substrates and have potential applications in

the healthcare industry. However, several promising research opportunities remain to further expand this study:

1. Further exploration of different surface morphologies could improve the photocatalytic properties of ZnO nanostructures under visible light, thereby enhancing their inherent bactericidal properties. This could include additional nano-structuring of ZnO to increase the specific surface area and potentially reduce the energy bandgap or employing surface modifications such as encapsulation or graphene-based composites.
2. Additional mechanistic studies should be undertaken to clarify how reactive oxygen species (ROS), generated through photocatalytic reactions at the ZnO nanopillar interface, diffuse through the PDMS or silicone oil layers and subsequently act upon bacteria. Specifically, this process likely involves molecular diffusion coupled with oxidative chain reactions. This mechanism could be thoroughly studied using real-time fluorescence microscopy for ROS tracking, isotopic or molecular labelling combined with advanced spectroscopy methods, or computational modelling to quantitatively describe ROS transport and reaction kinetics if experimental resources and conditions permit. Investigating attachment and cell death mechanisms for various bacterium types would further enrich the understanding of antibiofouling behaviour.
3. Experimental results confirming the non-cytotoxic nature of ZnO-based water-repellent surfaces toward mammalian cells open avenues for broader

biocompatibility research. Future studies could evaluate antibacterial properties in realistic scenarios, including applications on medical devices, building materials, and patient implants.

REFERENCES

1. Hall-Stoodley, L., J.W. Costerton, and P. Stoodley, *Bacterial biofilms: from the Natural environment to infectious diseases.* Nature Reviews Microbiology, 2004. **2**(2): p. 95-108.
2. van Kleef, E., et al., *Modelling the transmission of healthcare associated infections: a systematic review.* BMC Infect Dis, 2013. **13**: p. 294.
3. Percival, S.L., et al., *Healthcare-associated infections, medical devices and biofilms: risk, tolerance and control.* J Med Microbiol, 2015. **64**(Pt 4): p. 323-334.
4. Dadi, N.C.T., et al., *Impact of Healthcare-Associated Infections Connected to Medical Devices-An Update.* Microorganisms, 2021. **9**(11).
5. Kollef, M.H., et al., *Nosocomial Infection.* Crit Care Med, 2021. **49**(2): p. 169-187.
6. Monegro, A.F., V. Muppidi, and H. Regunath, *Hospital Acquired Infections*. 2022: StatPearls Publishing, Treasure Island (FL).
7. Camara, M., et al., *Economic significance of biofilms: a multidisciplinary and cross-sectoral challenge.* NPJ Biofilms Microbiomes, 2022. **8**(1): p. 42.
8. Ciofu, O., et al., *Antibiotic treatment of biofilm infections.* APMIS, 2017. **125**(4): p. 304-319.
9. Singh, A., et al., *Bacterial biofilm infections, their resistance to antibiotics therapy and current treatment strategies.* Biomedical Materials, 2022. **17**(2): p. 022003.

10. Gold, K., et al., *Antimicrobial Activity of Metal and Metal-Oxide Based Nanoparticles.* Advanced Therapeutics, 2018. **1**(3): p. 1700033.

11. Wooh, S. and H.J. Butt, *A Photocatalytically Active Lubricant-Impregnated Surface.* Angew Chem Int Ed Engl, 2017. **56**(18): p. 4965-4969.

12. Adams, L.K., D.Y. Lyon, and P.J. Alvarez, *Comparative eco-toxicity of nanoscale TiO2, SiO2, and ZnO water suspensions.* Water Res, 2006. **40**(19): p. 3527-32.

13. Jones, N., et al., *Antibacterial activity of ZnO nanoparticle suspensions on a broad spectrum of microorganisms.* FEMS Microbiol Lett, 2008. **279**(1): p. 71-6.

14. Leung, Y.H., et al., *Antibacterial activity of ZnO nanoparticles with a modified surface under ambient illumination.* Nanotechnology, 2012. **23**(47): p. 475703.

15. Wooh, S., et al., *Stable Hydrophobic Metal-Oxide Photocatalysts via Grafting Polydimethylsiloxane Brush.* Adv Mater, 2017. **29**(16).

16. van den Broek, P.J., T.J. Daha, and R.P. Mouton, *Bladder irrigation with povidone-iodine in prevention of urinary-tract infections associated with intermittent urethral catheterisation.* Lancet, 1985. **1**(8428): p. 563-5.

17. Heal, J.S., et al., *Bacterial contamination of surgical gloves by water droplets spilt after scrubbing.* J Hosp Infect, 2003. **53**(2): p. 136-9.

18. Ranjbaran, M. and A.K. Datta, *Retention and infiltration of bacteria on a plant leaf driven by surface water evaporation.* Physics of Fluids, 2019. **31**(11).

19. Pishbin, E., et al., *Frequency dependent multiphase flows on centrifugal microfluidics.* Lab Chip, 2020. **20**(3): p. 514-524.

20. Wang, C. and Z. Guo, *A comparison between superhydrophobic surfaces (SHS) and slippery liquid-infused porous surfaces (SLIPS) in application.* Nanoscale, 2020. **12**(44): p. 22398-22424.

21. Neinhuis, C., *Characterization and Distribution of Water-repellent, Self-cleaning Plant Surfaces.* Annals of Botany, 1997. **79**(6): p. 667-677.

22. Barthlott, W. and C. Neinhuis, *Purity of the sacred lotus, or escape from contamination in biological surfaces.* Planta, 1997. **202**(1): p. 1-8.

23. Solga, A., et al., *The dream of staying clean: Lotus and biomimetic surfaces.* Bioinspiration & Biomimetics, 2007. **2**(4): p. S126-S134.

24. Yan, Y.Y., N. Gao, and W. Barthlott, *Mimicking natural superhydrophobic surfaces and grasping the wetting process: a review on recent progress in preparing superhydrophobic surfaces.* Adv Colloid Interface Sci, 2011. **169**(2): p. 80-105.

25. Cassie, A.B.D. and S. Baxter, *Wettability of porous surfaces.* Transactions of the Faraday Society, 1944. **40**.

26. Roach, P., N.J. Shirtcliffe, and M.I. Newton, *Progess in superhydrophobic surface development.* Soft Matter, 2008. **4**(2): p. 224-240.

27. Bonn, D., et al., *Wetting and spreading.* Reviews of Modern Physics, 2009. **81**(2): p. 739-805.

28. Singh, N.S., et al., *Implementing Superhydrophobic Surfaces within Various Condensation Environments: A Review.* Advanced Materials Interfaces, 2020.

8(2).

29. Vasudevan, R., et al., *Microscale patterned surfaces reduce bacterial fouling-microscopic and theoretical analysis.* Colloids Surf B Biointerfaces, 2014. **117**: p. 225-32.

30. Ayazi, M., N. Golshan Ebrahimi, and E. Jafari Nodoushan, *Bacterial adhesion reduction on the surface with a simulated pattern: An insight into extrand model.* International Journal of Adhesion and Adhesives, 2019. **88**: p. 66-73.

31. Manoj, T.P., et al., *A simple, rapid and single step method for fabricating superhydrophobic titanium surfaces with improved water bouncing and self cleaning properties.* Applied Surface Science, 2020. **512**.

32. Ivanova, E.P., et al., *Antifungal versus antibacterial defence of insect wings.* J Colloid Interface Sci, 2021. **603**: p. 886-897.

33. Oh, J., et al., *Exploring the Role of Habitat on the Wettability of Cicada Wings.* ACS Appl Mater Interfaces, 2017. **9**(32): p. 27173-27184.

34. Román-Kustas, J., et al., *Molecular and Topographical Organization: Influence on Cicada Wing Wettability and Bactericidal Properties.* Advanced Materials Interfaces, 2020. **7**(10).

35. Hizal, F., et al., *Nanoengineered Superhydrophobic Surfaces of Aluminum with Extremely Low Bacterial Adhesivity.* ACS Appl Mater Interfaces, 2017. **9**(13): p. 12118-12129.

36. Pan, Q., et al., *Picosecond Laser-Textured Stainless Steel Superhydrophobic*

Surface with an Antibacterial Adhesion Property. Langmuir, 2019. **35**(35): p. 11414-11421.

37. Jitniyom, T., et al., *Biofouling resistant materials based on micro-structured surfaces with liquid-repellent properties.* Nano Select, 2023. **5**(3).

38. Papadopoulos, P., et al., *How superhydrophobicity breaks down.* Proc Natl Acad Sci U S A, 2013. **110**(9): p. 3254-8.

39. Milionis, A., E. Loth, and I.S. Bayer, *Recent advances in the mechanical durability of superhydrophobic materials.* Adv Colloid Interface Sci, 2016. **229**: p. 57-79.

40. Tian, X., T. Verho, and R.H. Ras, *SURFACE WEAR. Moving superhydrophobic surfaces toward real-world applications.* Science, 2016. **352**(6282): p. 142-3.

41. Hwang, G.B., et al., *The Anti-Biofouling Properties of Superhydrophobic Surfaces are Short-Lived.* ACS Nano, 2018. **12**(6): p. 6050-6058.

42. Villegas, M., et al., *Liquid-Infused Surfaces: A Review of Theory, Design, and Applications.* ACS Nano, 2019. **13**(8): p. 8517-8536.

43. Wong, T.-S., et al., *Bioinspired self-repairing slippery surfaces with pressure-stable omniphobicity.* Nature, 2011. **477**(7365): p. 443-447.

44. He, W., et al., *Emerging Applications of Bioinspired Slippery Surfaces in Biomedical Fields.* Chemistry, 2018. **24**(56): p. 14864-14877.

45. Li, H., M. Yan, and W. Zhao, *Designing a MOF-based slippery lubricant-infused porous surface with dual functional anti-fouling strategy.* J Colloid Interface Sci,

2022. **607**(Pt 2): p. 1424-1435.

46. Jing, Y., et al., *Design of an anticorrosion/bactericidal dual functional organic coating based on the slippery liquid-infused porous surface.* Appl. Surf. Sci., 2023. **639**.

47. Smith, J.D., et al., *Droplet mobility on lubricant-impregnated surfaces.* Soft Matter, 2013. **9**(6): p. 1772-1780.

48. Schellenberger, F., et al., *Direct observation of drops on slippery lubricant-infused surfaces.* Soft Matter, 2015. **11**(38): p. 7617-26.

49. Lee, J., et al., *Development of Multimodal Antibacterial Surfaces Using Porous Amine-Reactive Films Incorporating Lubricant and Silver Nanoparticles.* ACS Appl Mater Interfaces, 2019. **11**(6): p. 6550-6560.

50. Israelachvili, J.N., *Chapter 13 - Van der Waals Forces between Particles and Surfaces*, in *Intermolecular and Surface Forces (Third Edition)*, J.N. Israelachvili, Editor. 2011, Academic Press: San Diego. p. 253-289.

51. Young, T., *III. An essay on the cohesion of fluids.* Philosophical Transactions of the Royal Society of London, 1805. **95**(0): p. 65-87.

52. Liu, L., et al., *Dropwise Condensation by Nanoengineered Surfaces: Design, Mechanism, and Enhancing Strategies.* Advanced Materials Interfaces, 2021. **8**(24): p. 2101603.

53. Pierce, E., F.J. Carmona, and A. Amirfazli, *Understanding of sliding and contact angle results in tilted plate experiments.* Colloids and Surfaces A:

Physicochemical and Engineering Aspects, 2008. **323**(1): p. 73-82.

54. Butt, H.-J., et al., *Contact angle hysteresis.* Current Opinion in Colloid & Interface Science, 2022. **59**: p. 101574.

55. Wong, W.S.Y., et al., *Adaptive Wetting of Polydimethylsiloxane.* Langmuir, 2020. **36**(26): p. 7236-7245.

56. Wenzel, R.N., *Resistance of solid surfaces to wetting by water.* Industrial & engineering chemistry, 1936. **28**(8): p. 988-994.

57. Wenzel, R.N., *Surface roughness and contact angle.* The Journal of Physical Chemistry, 1949. **53**(9): p. 1466-1467.

58. Cassie, A.B.D. and S. Baxter, *Wettability of porous surfaces.* Transactions of the Faraday Society, 1944. **40**: p. 546.

59. Cassie, A., *Contact angles.* Discussions of the Faraday society, 1948. **3**: p. 11-16.

60. Gao, N., et al., *How drops start sliding over solid surfaces.* Nature Physics, 2018. **14**(2): p. 191-196.

61. Schnell, G., et al., *How droplets move on laser-structured surfaces: Determination of droplet adhesion forces on nano- and microstructured surfaces.* J Colloid Interface Sci, 2023. **630**(Pt A): p. 951-964.

62. Wang, J., et al., *Influence of surface roughness on contact angle hysteresis and spreading work.* Colloid and Polymer Science, 2020. **298**(8): p. 1107-1112.

63. Jothi Prakash, C.G. and R. Prasanth, *Approaches to design a surface with*

tunable wettability: a review on surface properties. Journal of Materials Science, 2021. **56**(1): p. 108-135.

64. Šikalo, Š. and E.N. Ganić, *Phenomena of droplet–surface interactions.* Experimental Thermal and Fluid Science, 2006. **31**(2): p. 97-110.

65. Rapp, B.E., *Chapter 9 - Fluids*, in *Microfluidics: Modelling, Mechanics and Mathematics*, B.E. Rapp, Editor. 2017, Elsevier: Oxford. p. 243-263.

66. Starinskiy, S., et al., *Spreading of Impacting Water Droplet on Surface with Fixed Microstructure and Different Wetting from Superhydrophilicity to Superhydrophobicity.* Water, 2023. **15**(4): p. 719.

67. Hu, Z., et al., *Understanding and Utilizing Droplet Impact on Superhydrophobic Surfaces: Phenomena, Mechanisms, Regulations, Applications, and Beyond.* Advanced Materials, 2024. **36**(11): p. 2310177.

68. Rioboo, R., M. Marengo, and C. Tropea, *Time evolution of liquid drop impact onto solid, dry surfaces.* Experiments in Fluids, 2002. **33**(1): p. 112-124.

69. Thenarianto, C., et al., *Energy Loss for Droplets Bouncing Off Superhydrophobic Surfaces.* Langmuir, 2023. **39**(8): p. 3162-3167.

70. Khojasteh, D., et al., *Droplet impact on superhydrophobic surfaces: A review of recent developments.* Journal of Industrial and Engineering Chemistry, 2016. **42**: p. 1-14.

71. Hu, H., et al., *Rebound behaviors of droplets impacting on a superhydrophobic surface.* Science China Physics, Mechanics and Astronomy, 2013. **56**(5): p.

960-965.

72. Antonini, C., A. Amirfazli, and M. Marengo, *Drop impact and wettability: From hydrophilic to superhydrophobic surfaces.* Physics of Fluids, 2012. **24**(10): p. 102104.

73. Tang, C., et al., *Dynamics of droplet impact on solid surface with different roughness.* International Journal of Multiphase Flow, 2017. **96**: p. 56-69.

74. Burzynski, D.A. and S.E. Bansmer, *Droplet splashing on thin moving films at high Weber numbers.* International Journal of Multiphase Flow, 2018. **101**: p. 202-211.

75. Zhou, J., et al., *Regulation of droplet dynamic behavior after droplet impact on superhydrophobic surfaces.* Colloids and Surfaces A: Physicochemical and Engineering Aspects, 2024. **685**: p. 133211.

76. Neinhuis, C. and W. Barthlott, *Characterization and Distribution of Water-repellent, Self-cleaning Plant Surfaces.* Annals of Botany, 1997. **79**(6): p. 667-677.

77. Nosonovsky, M. and B. Bhushan, *Multiscale effects and capillary interactions in functional biomimetic surfaces for energy conversion and green engineering.* Philos Trans A Math Phys Eng Sci, 2009. **367**(1893): p. 1511-39.

78. Jiang, R., et al., *Lotus-leaf-inspired hierarchical structured surface with non-fouling and mechanical bactericidal performances.* Chemical Engineering Journal, 2020. **398**: p. 125609.

79. Koch, K., et al., *Fabrication of artificial Lotus leaves and significance of hierarchical structure for superhydrophobicity and low adhesion.* Soft Matter, 2009. **5**(7): p. 1386.

80. Liu, Y., X. Chen, and J.H. Xin, *Can superhydrophobic surfaces repel hot water?* Journal of Materials Chemistry, 2009. **19**(31): p. 5602.

81. Wu, D., et al., *Three-Level Biomimetic Rice-Leaf Surfaces with Controllable Anisotropic Sliding.* Advanced Functional Materials, 2011. **21**(15): p. 2927-2932.

82. Han, Z., et al., *Anti-adhesive property of maize leaf surface related with temperature and humidity.* Journal of Bionic Engineering, 2017. **14**(3): p. 540-548.

83. Barthlott, W., et al., *The Salvinia Paradox: Superhydrophobic Surfaces with Hydrophilic Pins for Air Retention Under Water.* Advanced Materials, 2010. **22**(21): p. 2325-2328.

84. Feng, L., et al., *Petal Effect: A Superhydrophobic State with High Adhesive Force.* Langmuir, 2008. **24**(8): p. 4114-4119.

85. Chen, H., et al., *Continuous directional water transport on the peristome surface of Nepenthes alata.* Nature, 2016. **532**(7597): p. 85-89.

86. Zhang, P., et al., *Surfaces Inspired by the Nepenthes Peristome for Unidirectional Liquid Transport.* Advanced Materials, 2017. **29**(45): p. 1702995.

87. Gao, X. and L. Jiang, *Water-repellent legs of water striders.* Nature, 2004. **432**(7013): p. 36-36.

88. Zheng, Y., X. Gao, and L. Jiang, *Directional adhesion of superhydrophobic butterfly wings.* Soft Matter, 2007. **3**(2): p. 178-182.

89. Oh, J., et al., *Exploring the role of habitat on the wettability of cicada wings.* ACS Applied Materials & Interfaces, 2017. **9**(32): p. 27173-27184.

90. Aideo, S.N. and D. Mohanta, *Limiting hydrophobic behavior and reflectance response of dragonfly and damselfly wings.* Applied Surface Science, 2016. **387**: p. 609-616.

91. Ivanova, E.P., et al., *Natural bactericidal surfaces: mechanical rupture of Pseudomonas aeruginosa cells by cicada wings.* Small, 2012. **8**(16): p. 2489.

92. Hasan, J., et al., *Selective bactericidal activity of nanopatterned superhydrophobic cicada Psaltoda claripennis wing surfaces.* Applied Microbiology and Biotechnology, 2013. **97**(20): p. 9257-9262.

93. Pogodin, S., et al., *Biophysical model of bacterial cell interactions with nanopatterned cicada wing surfaces.* Biophysical journal, 2013. **104**(4): p. 835-840.

94. Bandara, C.D., et al., *Bactericidal effects of natural nanotopography of dragonfly wing on Escherichia coli.* ACS applied materials & interfaces, 2017. **9**(8): p. 6746-6760.

95. Tripathy, A., et al., *Natural and bioinspired nanostructured bactericidal surfaces.* Advances in Colloid and Interface Science, 2017. **248**: p. 85-104.

96. Rao, T.S., *Chapter 26 - Biofouling (macro-fouling) in seawater intake systems*,

in *Water-Formed Deposits*, Z. Amjad and K.D. Demadis, Editors. 2022, Elsevier. p. 565-587.

97. Sauer, K., et al., *Pseudomonas aeruginosa Displays Multiple Phenotypes during Development as a Biofilm.* Journal of Bacteriology, 2002. **184**(4): p. 1140-1154.

98. Sauer, K., et al., *The biofilm life cycle: expanding the conceptual model of biofilm formation.* Nature Reviews Microbiology, 2022. **20**(10): p. 608-620.

99. Wang, T., et al., *Robust Biomimetic Hierarchical Diamond Architecture with a Self-Cleaning, Antibacterial, and Antibiofouling Surface.* ACS Appl Mater Interfaces, 2020. **12**(21): p. 24432-24441.

100. Liu, S., et al., *Dual-Functional, Superhydrophobic Coatings with Bacterial Anticontact and Antimicrobial Characteristics.* ACS Appl Mater Interfaces, 2020. **12**(19): p. 21311-21321.

101. Ozkan, E., et al., *Bioinspired superhydrophobic surfaces with silver and nitric oxide-releasing capabilities to prevent device-associated infections and thrombosis.* J Colloid Interface Sci, 2024. **664**: p. 928-937.

102. Zhong Lin, W., *Zinc oxide nanostructures: growth, properties and applications.* Journal of Physics: Condensed Matter, 2004. **16**(25): p. R829.

103. Sirelkhatim, A., et al., *Review on Zinc Oxide Nanoparticles: Antibacterial Activity and Toxicity Mechanism.* Nano-Micro Letters, 2015. **7**(3): p. 219-242.

104. Gerbreders, V., et al., *Hydrothermal synthesis of ZnO nanostructures with*

controllable morphology change. CrystEngComm, 2020. **22**(8): p. 1346-1358.

105. Liu, Q., et al., *Ammonia-Induced Seed Layer Transformations in a Hydrothermal Growth Process of Zinc Oxide Nanowires.* The Journal of Physical Chemistry C, 2020. **124**(37): p. 20563-20568.

106. Mohan, S., et al., *Hydrothermal synthesis and characterization of Zinc Oxide nanoparticles of various shapes under different reaction conditions.* Nano Express, 2020. **1**(3): p. 030028.

107. Akpomie, K.G., et al., *One-pot synthesis of zinc oxide nanoparticles via chemical precipitation for bromophenol blue adsorption and the antifungal activity against filamentous fungi.* Sci Rep, 2021. **11**(1): p. 8305.

108. Yang, J., et al., *Synthesis of ZnO nanosheets via electrodeposition method and their optical properties, growth mechanism.* Optical Materials, 2015. **46**: p. 179-185.

109. Xu, L., et al., *Morphological control of ZnO nanostructures by electrodeposition.* J Phys Chem B, 2005. **109**(28): p. 13519-22.

110. Ponja, S.D., et al., *Highly conductive and transparent gallium doped zinc oxide thin films via chemical vapor deposition.* Sci Rep, 2020. **10**(1): p. 638.

111. Lipovsky, A., et al., *Antifungal activity of ZnO nanoparticles—the role of ROS mediated cell injury.* Nanotechnology, 2011. **22**(10): p. 105101.

112. Zhang, L., et al., *ZnO nanofluids – A potential antibacterial agent.* Progress in Natural Science, 2008. **18**(8): p. 939-944.

113. Brunner, T.J., et al., *In Vitro Cytotoxicity of Oxide Nanoparticles: Comparison to Asbestos, Silica, and the Effect of Particle Solubility.* Environmental Science & Technology, 2006. **40**(14): p. 4374-4381.

114. Li, M., L. Zhu, and D. Lin, *Toxicity of ZnO Nanoparticles to Escherichia coli: Mechanism and the Influence of Medium Components.* Environmental Science & Technology, 2011. **45**(5): p. 1977-1983.

115. Brayner, R., et al., *Toxicological Impact Studies Based on Escherichia coli Bacteria in Ultrafine ZnO Nanoparticles Colloidal Medium.* Nano Letters, 2006. **6**(4): p. 866-870.

116. Zhang, L., et al., *Investigation into the antibacterial behaviour of suspensions of ZnO nanoparticles (ZnO nanofluids).* Journal of Nanoparticle Research, 2007. **9**(3): p. 479-489.

117. Ramos, A.A., et al., *Polyphenolic Compounds from Salvia Species Protect Cellular DNA from Oxidation and Stimulate DNA Repair in Cultured Human Cells.* Journal of Agricultural and Food Chemistry, 2010. **58**(12): p. 7465-7471.

118. Guo, H.-L., et al., *Oxygen deficient ZnO1−x nanosheets with high visible light photocatalytic activity.* Nanoscale, 2015. **7**(16): p. 7216-7223.

119. Wang, J., et al., *Oxygen Vacancy Induced Band-Gap Narrowing and Enhanced Visible Light Photocatalytic Activity of ZnO.* ACS Applied Materials & Interfaces, 2012. **4**(8): p. 4024-4030.

120. Qi, K., et al., *Review on the improvement of the photocatalytic and antibacterial*

activities of ZnO. Journal of Alloys and Compounds, 2017. **727**: p. 792-820.

121. Lakshmi Prasanna, V. and R. Vijayaraghavan, *Insight into the Mechanism of Antibacterial Activity of ZnO: Surface Defects Mediated Reactive Oxygen Species Even in the Dark.* Langmuir, 2015. **31**(33): p. 9155-9162.

122. Xu, X., et al., *Antimicrobial Mechanism Based on H2O2 Generation at Oxygen Vacancies in ZnO Crystals.* Langmuir, 2013. **29**(18): p. 5573-5580.

123. Biswas, A., U. Kar, and N.R. Jana, *Cytotoxicity of ZnO nanoparticles under dark conditions via oxygen vacancy dependent reactive oxygen species generation.* Physical Chemistry Chemical Physics, 2022. **24**(22): p. 13965-13975.

124. Padmavathy, N. and R. Vijayaraghavan, *Enhanced bioactivity of ZnO nanoparticles—an antimicrobial study.* Science and Technology of Advanced Materials, 2008. **9**(3): p. 035004.

125. Awad, A., et al., *Polymer nanocomposites part 1: Structural characterization of zinc oxide nanoparticles synthesized via novel calcination method.* Journal of Thermoplastic Composite Materials, 2014. **28**(9): p. 1343-1358.

126. Ahmed, B., et al., *Mitochondrial and Chromosomal Damage Induced by Oxidative Stress in Zn(2+) Ions, ZnO-Bulk and ZnO-NPs treated Allium cepa roots.* Sci Rep, 2017. **7**: p. 40685.

127. Huang, Y., et al., *Facile Synthesis of Zn2+-Based Hybrid Nanoparticles as a New Paradigm for the Treatment of Internal Bacterial Infections.* Advanced Functional Materials, 2021. **32**(15).

128. Wen, Z., et al., *Mesoporous TiO(2) Coatings Regulate ZnO Nanoparticle Loading and Zn(2+) Release on Titanium Dental Implants for Sustained Osteogenic and Antibacterial Activity.* ACS Appl Mater Interfaces, 2023. **15**(12): p. 15235-15249.

129. Brayner, R., et al., *Toxicological impact studies based on Escherichia coli bacteria in ultrafine ZnO nanoparticles colloidal medium.* Nano Lett, 2006. **6**(4): p. 866-70.

130. Huang, Z., et al., *Toxicological effect of ZnO nanoparticles based on bacteria.* Langmuir, 2008. **24**(8): p. 4140-4.

131. Zhang, L., et al., *Investigation into the antibacterial behaviour of suspensions of ZnO nanoparticles (ZnO nanofluids).* Journal of Nanoparticle Research, 2006. **9**(3): p. 479-489.

132. Matula, K., et al., *Influence of nanomechanical stress induced by ZnO nanoparticles of different shapes on the viability of cells.* Soft Matter, 2016. **12**(18): p. 4162-9.

133. Milionis, A., et al., *Water-Based Scalable Methods for Self-Cleaning Antibacterial ZnO-Nanostructured Surfaces.* Industrial & Engineering Chemistry Research, 2020. **59**(32): p. 14323-14333.

134. Seth, A., et al., *Nanostructured antimicrobial ZnO surfaces coated with an imidazolium-based ionic liquid.* Materials Advances, 2024. **5**(8): p. 3186-3197.

135. Rahmah, M.I., R.S. Sabry, and W.J. Aziz, *Preparation and Antibacterial Activity*

of Superhydrophobic Modified ZnO/PVC Nanocomposite. Journal of Bionic Engineering, 2022. **19**(1): p. 139-154.

136. Gao, D., et al., *Multifunctional cotton fabric loaded with Ce doped ZnO nanorods.* Materials Research Bulletin, 2017. **89**: p. 102-107.

137. Gao, D., et al., *Construct the Multifunction of Cotton Fabric by Synergism between Nano ZnO and Ag.* Fibers and Polymers, 2020. **21**(3): p. 505-512.

138. Tang, Y., et al., *Bioinspired photocatalytic ZnO/Au nanopillar-modified surface for enhanced antibacterial and antiadhesive property.* Chemical Engineering Journal, 2020. **398**: p. 125575.

139. Wang, T., et al., *A compound of ZnO/PDMS with photocatalytic, self-cleaning and antibacterial properties prepared via two-step method.* Applied Surface Science, 2021. **550**: p. 149286.

140. Ozkan, E., et al., *Bioinspired ultra-low fouling coatings on medical devices to prevent device-associated infections and thrombosis.* Journal of Colloid and Interface Science, 2022. **608**: p. 1015-1024.

141. Xia, T., et al., *Comparison of the Mechanism of Toxicity of Zinc Oxide and Cerium Oxide Nanoparticles Based on Dissolution and Oxidative Stress Properties.* ACS Nano, 2008. **2**(10): p. 2121-2134.

142. Landsiedel, R., et al., *Testing Metal-Oxide Nanomaterials for Human Safety.* Advanced Materials, 2010. **22**(24): p. 2601-2627.

143. Watson, R., et al., *Development of biocide coated polymers and their*

antimicrobial efficacy. Nano Select, 2023. **4**(7): p. 442-453.

144. Chan, S., et al., *Bacterial release from pipe biofilm in a full-scale drinking water distribution system.* npj Biofilms and Microbiomes, 2019. **5**(1): p. 9.

145. Maes, S., et al., *Occurrence and characterisation of biofilms in drinking water systems of broiler houses.* BMC Microbiol, 2019. **19**(1): p. 77.

146. Mahapatra, A., et al., *Study of biofilm in bacteria from water pipelines.* J Clin Diagn Res, 2015. **9**(3): p. Dc09-11.

147. Uneputty, A., et al., *Strategies applied to modify structured and smooth surfaces: A step closer to reduce bacterial adhesion and biofilm formation.* Colloid and Interface Science Communications, 2022. **46**: p. 100560.

148. Wang, M., G. Buist, and J.M. van Dijl, *Staphylococcus aureus cell wall maintenance - the multifaceted roles of peptidoglycan hydrolases in bacterial growth, fitness, and virulence.* FEMS Microbiol Rev, 2022. **46**(5).

149. Shiomi, D., M. Sakai, and H. Niki, *Determination of bacterial rod shape by a novel cytoskeletal membrane protein.* The EMBO Journal, 2008. **27**(23): p. 3081-3091-3091.

150. Monteiro, J.M., et al., *Cell shape dynamics during the staphylococcal cell cycle.* Nat Commun, 2015. **6**: p. 8055.

151. Luan, Y., et al., *Bacterial interactions with nanostructured surfaces.* Current Opinion in Colloid & Interface Science, 2018. **38**: p. 170-189.

152. Román-Kustas, J., et al., *Molecular and Topographical Organization: Influence*

on Cicada Wing Wettability and Bactericidal Properties. Advanced Materials Interfaces, 2020. **7**(10): p. 2000112.

153. Jitniyom, T., et al., *Biofouling resistant materials based on micro-structured surfaces with liquid-repellent properties.* Nano Select, 2024. **5**(3): p. 2300158.

154. Yi, G., et al., *ZnO Nanopillar Coated Surfaces with Substrate-Dependent Superbactericidal Property.* Small, 2018. **14**(14): p. e1703159.

155. Alves, M.M., et al., *New Insights into Antibiofilm Effect of a Nanosized ZnO Coating against the Pathogenic Methicillin Resistant Staphylococcus aureus.* ACS Appl Mater Interfaces, 2017. **9**(34): p. 28157-28167.

156. Liu, J., et al., *Optimizing Hydrophobicity and Photocatalytic Activity of PDMS-Coated Titanium Dioxide.* ACS Appl Mater Interfaces, 2019. **11**(30): p. 27422-27425.

157. Peppou-Chapman, S. and C. Neto, *Mapping Depletion of Lubricant Films on Antibiofouling Wrinkled Slippery Surfaces.* ACS Applied Materials & Interfaces, 2018. **10**(39): p. 33669-33677.

158. Pan, W., et al., *A facile and high-efficient method to fabricate slippery liquid-infused porous surface with enhanced functionality.* Surface and Coatings Technology, 2023. **472**: p. 129897.

159. Jh, M., *Experiments in Molecular Genetics*. 1972.

160. King, E.O., M.K. Ward, and D.E. Raney, *Two simple media for the demonstration of pyocyanin and fluorescin.* J Lab Clin Med, 1954. **44**(2): p. 301-7.

161. Ghasemi, N., J. Seyfi, and M.J. Asadollahzadeh, *Imparting superhydrophobic and antibacterial properties onto the cotton fabrics: synergistic effect of zinc oxide nanoparticles and octadecanethiol.* Cellulose, 2018. **25**(7): p. 4211-4222.

162. Cai, Y., et al., *Fabricating superhydrophobic and oleophobic surface with silica nanoparticles modified by silanes and environment-friendly fluorinated chemicals.* Applied Surface Science, 2018. **450**: p. 102-111.

163. Liu, S., et al., *Self-cleaning transparent superhydrophobic coatings through simple sol–gel processing of fluoroalkylsilane.* Applied Surface Science, 2015. **351**: p. 897-903.

164. Joanny, J.F. and P.G. de Gennes, *A model for contact angle hysteresis.* The Journal of Chemical Physics, 1984. **81**(1): p. 552-562.

165. Tran, H.H., et al., *Lubricant Depletion‐Resistant Slippery Liquid‐Infused Porous Surfaces via Capillary Rise Lubrication of Nanowire Array.* Advanced Materials Interfaces, 2021. **8**(7).

166. Wong, T.S., et al., *Bioinspired self-repairing slippery surfaces with pressure-stable omniphobicity.* Nature, 2011. **477**(7365): p. 443-7.

167. Wang, J., et al., *Defect-rich ZnO nanosheets of high surface area as an efficient visible-light photocatalyst.* Applied Catalysis B: Environmental, 2016. **192**: p. 8-16.

168. Ahmad, M., et al., *Synthesis of hierarchical flower-like ZnO nanostructures and their functionalization by Au nanoparticles for improved photocatalytic and high*

performance Li-ion battery anodes. Journal of Materials Chemistry, 2011. **21**(21).

169. Guo, M.Y., et al., *Effect of Native Defects on Photocatalytic Properties of ZnO.* The Journal of Physical Chemistry C, 2011. **115**(22): p. 11095-11101.

170. Singh, J., et al., *Evidence of oxygen defects mediated enhanced photocatalytic and antibacterial performance of ZnO nanorods.* Colloids and Surfaces B: Biointerfaces, 2019. **184**: p. 110541.

171. Hirota, K., et al., *Preparation of zinc oxide ceramics with a sustainable antibacterial activity under dark conditions.* Ceramics International, 2010. **36**(2): p. 497-506.

172. Thongsuriwong, K., P. Amornpitoksuk, and S. Suwanboon, *Photocatalytic and antibacterial activities of Ag-doped ZnO thin films prepared by a sol–gel dip-coating method.* Journal of Sol-Gel Science and Technology, 2012. **62**(3): p. 304-312.

173. Robertson, J., et al., *Optimisation of the Protocol for the LIVE/DEAD((R)) BacLight(TM) Bacterial Viability Kit for Rapid Determination of Bacterial Load.* Front Microbiol, 2019. **10**: p. 801.

174. Berney, M., et al., *Assessment and interpretation of bacterial viability by using the LIVE/DEAD BacLight Kit in combination with flow cytometry.* Appl Environ Microbiol, 2007. **73**(10): p. 3283-90.

175. Pigeot-Rémy, S., et al., *Photocatalysis and disinfection of water: Identification of potential bacterial targets.* Applied Catalysis B: Environmental, 2011. **104**(3-

4): p. 390-398.

176. Ma, H., et al., *Impact of solar UV radiation on toxicity of ZnO nanoparticles through photocatalytic reactive oxygen species (ROS) generation and photo-induced dissolution.* Environmental Pollution, 2014. **193**: p. 165-172.

177. Dağlıoğlu, Y. and B. Yılmaz Öztürk, *Effect of concentration and exposure time of ZnO-TiO2 nanocomposite on photosynthetic pigment contents, ROS production ability, and bioaccumulation of freshwater algae (Desmodesmus multivariabilis).* Caryologia, 2018. **71**(1): p. 13-23.

178. Hung, C., et al., *Escherichia coli biofilms have an organized and complex extracellular matrix structure.* mBio, 2013. **4**(5): p. e00645-13.

179. Burdman, S., et al., *Involvement of Type IV Pili in Pathogenicity of Plant Pathogenic Bacteria.* Genes (Basel), 2011. **2**(4): p. 706-35.

180. Watson, G.S., et al., *A Simple Model for Binding and Rupture of Bacterial Cells on Nanopillar Surfaces.* Adv. Mater. Interfaces, 2019. **6**(10): p. 1801646.

181. Jenkins, J., et al., *Antibacterial effects of nanopillar surfaces are mediated by cell impedance, penetration and induction of oxidative stress.* Nat Commun, 2020. **11**(1): p. 1626.

182. Elbourne, A., R.J. Crawford, and E.P. Ivanova, *Nano-structured antimicrobial surfaces: From nature to synthetic analogues.* J Colloid Interface Sci, 2017. **508**: p. 603-616.